7-13-2024

Investigations and Characterization of Loud Transient Noise in Advanced LIGO Detectors

Shania Nichols
Louisiana State University at Baton Rouge

INVESTIGATIONS AND CHARACTERIZATION OF LOUD TRANSIENT NOISE IN ADVANCED LIGO DETECTORS

A Dissertation

Submitted to the Graduate Faculty of the
Louisiana State University and
Agricultural and Mechanical College
in partial fulfillment of the
requirements for the degree of
Doctor of Philosophy

in

The Department of Physics and Astronomy

by
Shania A. Nichols
B.S., State University of New York at Oswego, 2018
August 2024

This thesis is dedicated to my mother, Nadine. You sparked my curiosity about the universe at an early age by teaching me the constellations. Thanks mom, for showing me the stars.

One day when the physics community,
like jazz, includes contributions from
all groups of people, regardless of
creed, it will reach new heights,
allowing us to solve problems once
thought to be impossible.

—Stephon Alexander
The Jazz of Physics

Acknowledgments

I would like to express my deepest gratitude to all those who have supported and guided me throughout the course of my research and studies. This thesis would not have been possible without the encouragement, mentorship, and unwavering support from my advisors, colleagues, friends, and family.

To Gaby, there are no words that can express how grateful I am to have you as an advisor. The support and knowledge you have provided me throughout my years in graduate school have been immeasurable. Thank you for always encouraging me to present talks and posters at various conferences. Your dedication to your students and LIGO is amazing and I am forever thankful for this experience.

To Catherine Deibel, Joseph Giaime, Matthew Penny and Lawrence Smolinsky, thank you for agreeing to be on my thesis committee.

To the LSU LIGO Group, thank you for shaping my graduate school experience. You all are like family to me. Thank you for all the productive research discussions and suggestions that helped move my research forward. I am thankful for all of the memories we've made along the way.

To the Detector Characterization Working Group, thank you for teaching me so much about LIGO and getting me involved with group early on. The DetChar Group has fostered an environment that allowed me to grow as a researcher. I am thankful for the opportunities I've received from being a part of the Noise Mitigation Review Team to being the DetChar Representative for the GW230529 Editorial Team.

To Anamaria, thank you for teaching me about the LIGO instrument and being a guiding figure on my hunt for the source of loud glitches. I am thankful for the insightful

talks we've had and your knowledge of the detectors never ceases to amaze me.

To the researchers and staff at LIGO Livingston, thank you for making my visits enjoyable. I've learned so much by spending time at site and talking with you all.

To Tyler, Brett, Malaysia, Amanda, Jailene, Cheyanne, Kierah, Ben, Khris, Sage, Katie, Michelle, Alex, Chalese, Brionna, Kiara, Mélissa, Randa, Riva and all of my dearest friends, thank you for always showing me love and support throughout my journey. I couldn't have done this without all of your words of encouragement, phone calls and video chats.

To my Mom, Nkosi, Tanty, Uncle Fitzy, and Grandma, thank you for all of the love and support you've shown me my entire life and especially though my years in graduate school. I wouldn't be the person I am today without you all.

To Amiri, I got you the week before my general exam and you've been my best friend and light of my world since. Thank you for always putting a smile on my face and coming with my to campus for all of my meetings. Thank you for napping next to me whenever I had zoom meetings. You've kept me grounded throughout this process, always giving me something to look forward to.

Table of Contents

List of Tables

List of Figures

Abstract

In the era of gravitational wave (GW) astronomy, the detection of cosmic events such as black hole and neutron star mergers has become routine due to the Advanced LIGO (aLIGO) detectors. However, the sensitivity of these detectors also makes them susceptible to loud transient noise, which can obscure GW signals. This thesis investigates loud transient noise with a Signal-to-Noise Ratio (SNR) greater than 100, focusing particularly on the most extreme transients with SNR exceeding 1000.

We begin by analyzing the impact of loud transient noise on the binary neutron star (BNS) range of aLIGO detectors across observation runs O2, O3, and O4a. Despite improvements in interferometer sensitivity, the SNR and amplitude of loud glitches have remained constant. My statistical analysis reveals that the daily rate of these glitches follows a Poisson distribution, indicating their independent occurrence.

A comprehensive study of auxiliary data channels identifies those significantly affected by loud transient noise. An analysis of auxiliary data highlights interferometer sensing and control channels that witness these glitches, particularly noting that certain transient noise classifications, such as Blip, Koi Fish, and Extremely Loud, may share common origins.

Machine learning techniques, specifically t-SNE, are employed to cluster different Gravity Spy glitch classes and the time series of loud transient noise. This clustering supports the hypothesis of an energy scale continuum between Blip, Koi Fish, and Extremely Loud glitches. Additionally, I identify distinct morphologies of loud transient noise, laying the groundwork for determining their characteristic durations.

Potential sources of loud transient noise are examined, including residual gases,

dust particles, and the differential arm length (DARM) control loop. Although these sources are ruled out based on observed behaviors and experimental noise injections, the research provides a deeper understanding of loud transient noise characteristics. This thesis establishes a foundation for future research, emphasizing the importance of detector characterization research to study transient noise in GW strain data. We aim to uncover the sources of loud transient noise, thereby improving the data quality for GW detection and enhancing our understanding of the universe.

Chapter 1. Gravitational Waves: Theory and Sources

Published in 1915, Albert Einstein's General Theory of Relativity revolutionized our understanding of gravity [1]. General relativity describes the gravitational force as a property of a curved four-dimensional spacetime, where the curvature of the spacetime manifold is influenced by the amount of mass and energy present. Massive objects, such as stars, distort their surrounding spacetime and smaller objects, such as planets and asteroids, orbit them along geodesic paths. This drastically differed from our understanding of gravity from Newton's law of universal gravitation [2], which is still used as an approximation of gravity's effects.

General relativity has predicted several phenomena, which could not be accounted for by Newtonian gravity alone, including the perihelion precession of Mercury's orbit, the bending of light due to gravity, the gravitational redshift of light, black holes, and gravitational waves. Many of these predictions were proven in the 20^{th} century, including the indirect observation of gravitational waves from the orbital decay of the Hulse–Taylor Binary Pulsar [3]. Nearly one hundred years after general relativity was published, the direct obsrvation of gravitational waves would finally occur. On September 14, 2015 at 09:50:45 UTC the aLIGO detectors, located in Hanford, Washington, LHO, and Livingston, Louisiana, LLO, observed a transient gravitational wave signal from the inspiral of stellar sized binary black holes (GW150914) with a source distance of 410 Mpc [4]. This chapter details the mathematical theory, astrophysical sources and observations of gravitational waves.

1.1. Gravitational Waves in General Relativity

To understand the mathematical basis for gravitational waves, we begin with flat 3-dimensional space with coordinates (x, y, z). The spatial distance between two points in this space is

$$ds^2 = dx^2 + dy^2 + dz^2. \tag{1.1}$$

In Special Relativity Einstein introduces the concept of 4-dimensional flat spacetime with coordinates (t, x, y, z). The spacetime interval between two points is now

$$ds^2 = -c^2dt^2 + dx^2 + dy^2 + dz^2, \tag{1.2}$$

which is known as Minkowski space, where c is the speed of light. In General Relativity, $g_{\mu\nu}$ is a metric that encapsulates the geometric and gravitational properties of spacetime, defining how distances and intervals are measured. In Minkowski space, $g_{\mu\nu} = \eta_{\mu\nu}$. To write equation 1.2 using Einstein notation, we introduce the Minkowski metric with coordinates (ct, x, y, z),

$$\eta_{\mu\nu} = \begin{pmatrix} -1 & 0 & 0 & 0 \\ 0 & 1 & 0 & 0 \\ 0 & 0 & 1 & 0 \\ 0 & 0 & 0 & 1 \end{pmatrix}. \tag{1.3}$$

Equation 1.2 can now be written as:

$$ds^2 = \eta_{\mu\nu}dx^\mu dx^\nu. \tag{1.4}$$

Einstein's equations in the theory of general relativity relate the geometry, or curvature, of spacetime to the distribution of matter and energy within it,

$$G_{\mu\nu} = \frac{8\pi G}{c^4}T_{\mu\nu} \tag{1.5}$$

$G_{\mu\nu}$ known as the Einstein Tensor and it describes the curvature of spacetime in a way that is consistent with conservation of energy and momentum. It is constructed from the products of the first and second derivatives of the metric $g_{\mu\nu}$. G is the Newtonian gravitational constant. The stress-energy tensor, $T_{\mu\nu}$, describes the density and flux of energy and momentum in spacetime.

Now we consider a spacetime interval which is no longer flat, but instead has a weak gravitational field. We know from General Relativity the presence of gravity causes spacetime to curve. The metric is now given by the Minkowski form plus a small perturbation,

$$g_{\mu\nu} = \eta_{\mu\nu} + h_{\mu\nu} \qquad |h_{\mu\nu}| \ll 1. \tag{1.6}$$

The assumption of $|h_{\mu\nu}| \ll 1$ allows us to only keep the linear terms in the calculation as we are assuming the scale of the perturbation is much smaller than that of curvature scale of the spacetime background. A small perturbation to the spacetime interval is now

$$ds^2 = (\eta_{\mu\nu} + h_{\mu\nu} + O({h_{\mu\nu}}^2))dx^\mu dx^\nu = g_{\mu\nu}dx^\mu dx^\nu. \tag{1.7}$$

Einstein's equations in vacuum, where $T_{\mu\nu} = 0$, simplify to a wave equation given by,

$$\left(\nabla^2 - \frac{1}{c^2}\frac{\partial^2}{\partial t^2}\right) h_{\mu\nu} = 0. \tag{1.8}$$

The perturbation, $h_{\mu\nu}$, then describes a gravitational wave traveling through flat space in the $\hat{z}$ direction. We then select a gauge transformation known as the transverse traceless gauge (TT gauge). "Transverse" component of the gauge indicates that the effects of the GW are perpendicular to the direction of wave propagation. This means in the TT gauge, GWs compress and stretch spacetime in the perpendicular direction to their propagation.

The "traceless" component signifies that the trace of the perturbation tensor is zero, implying that the wave does not alter the local spacetime volume as it travels. Choosing this coordinate system simplifies the mathematics of GWs propagating through a vacuum.

The perturbation, to first order, is

$$h_{\mu\nu} = \begin{pmatrix} 0 & 0 & 0 & 0 \\ 0 & a & b & 0 \\ 0 & b & -a & 0 \\ 0 & 0 & 0 & 0 \end{pmatrix}, \tag{1.9}$$

or as the sum of two components, $h = a\hat{h}_+ + b\hat{h}_\times$. These components form an orthogonal basis which describe the polarizations of the wave traveling in the $\hat{z}$ direction, shown in Figure 1.1. h_+, pronounced plus, describes the oscillation (stretching and compression) of

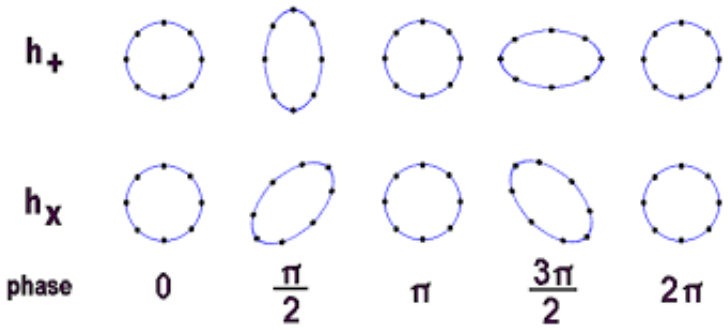

Figure 1.1. The effect of the two GW polarizations on a ring of test masses. The GW stretches and compresses spacetime [5].

spacetime in $\hat{x}$ and $\hat{y}$ directions and is given by

$$h_+ = \begin{pmatrix} 0 & 0 & 0 & 0 \\ 0 & 1 & 0 & 0 \\ 0 & 0 & -1 & 0 \\ 0 & 0 & 0 & 0 \end{pmatrix}. \tag{1.10}$$

$h_\times$, pronounced cross, describes the oscillation of spacetime in the direction rotated 45° from that of h_+ and is expressed as,

$$h_\times = \begin{pmatrix} 0 & 0 & 0 & 0 \\ 0 & 0 & 1 & 0 \\ 0 & 1 & 0 & 0 \\ 0 & 0 & 0 & 0 \end{pmatrix}. \tag{1.11}$$

Thus, $h_{\mu\nu}$ is a transverse wave and represents a GW propagating at the speed of light in a vacuum. The two polarizations can be expressed as a plane wave:

$$h_{\mu\nu} = \begin{pmatrix} 0 & 0 & 0 & 0 \\ 0 & -h_+ & h_\times & 0 \\ 0 & h_\times & h_+ & 0 \\ 0 & 0 & 0 & 0 \end{pmatrix} \cos(\omega t - kz). \tag{1.12}$$

The Advanced LIGO instruments measure GW strain, $h = \frac{\Delta L}{L}$, where L is the arm length of the detector. The longer the arm length of the interferometer, the more sensitive it is to the small perturbations of spacetime.

1.2. Gravitational Wave Sources

In general relativity, gravitational radiation is produced by a time varying quadrupole moment, $I_{\mu\nu}$. The second time derivative of the quadrupole moment is non-zero and gravitational radiation is given by

$$h_{\mu\nu} = \frac{2G}{Rc^4}\ddot{I}_{\mu\nu}, \tag{1.13}$$

where R is the distance between the source and the interferometer. Only sources that are not spherically symmetric emit gravitational radiation.

Although everyday objects such as humans and cars can emit gravitational radiation according to classical theory, it takes it takes cataclysmic astrophysical events to produce GWs that are detectable by aLIGO and other ground-based detectors. We search for GWs from four types of sources: compact binary coalescences, continuous sources, burst sources, and cosmological and astrophysical stochastic backgrounds.

1.2.1. Compact Binary Coalescence

Compact binary systems produce GWs as the objects in the system orbit each other. The GW carry away orbital energy from the system causing the objects to inspiral and the orbital period of the binary decreases. The amplitude and frequency of the GWs increase and eventually the objects coalesce. Numerical general relativity provides models of the GW waveform from binary systems. There are three types of binary systems in this category: binary black hole (BBH), BNS and neutron star–black hole (NSBH). Thus far all GW signals detected by aLIGO have come from binary systems and GWs from each type have been detected.

We can derive the amplitude of the GW strain by considering a BNS system of masses m_1 and m_2 orbiting the xy-plane. The components of the quadrupole moments are:

$$I_{xx} = \mu r^2 \cos^2(\omega t), \tag{1.14}$$

$$I_{yy} = \mu r^2 \sin^2(\omega t), \tag{1.15}$$

$$I_{xy} = I_{yx} = \mu r^2 \cos(\omega t) \sin(\omega t). \tag{1.16}$$

The I_{zz} component is constant for this case, the reduced mass of the system $\mu = \frac{m_1 m_2}{m_1+m_2}$, the angular frequency is $\omega = 2\pi f_{orbital}$, and r is the radius of the orbit. Taking the second time derivatives of the quadrupole moment components yields:

$$\ddot{I}_{xx} = -A\cos(2\omega t), \tag{1.17}$$

$$\ddot{I}_{yy} = A\cos(2\omega t), \tag{1.18}$$

$$\ddot{I}_{xy} = \ddot{I}_{yx} = -A\sin(\omega t)\sin(2\omega t), \tag{1.19}$$

where $A = \mu r^2 \omega^2$. Plugging the second time derivatives into equation 1.13 with $m_1 = m_2 = 1.4M_\odot$, $r = 20$ km, $f_{orbital} = 400$ Hz, and $R = 15$ Mpc which is the distance to the Virgo Cluster, then the strain is

$$h \approx 10^{-21}. \tag{1.20}$$

1.2.2. Continuous Wave Sources

Continuous GW sources are astrophysical objects or systems that emit gravitational radiation steadily over extended periods of time. These sources generate a persistent, periodic signal. The most promising candidates for continuous GW emission are rapidly rotating neutron stars, or Pulsars, with slight asymmetries [6, 7]. Pulsars have uneven mass distributions due to crustal deformations that create a time varying quadrupole moment. Continuous GWs offer a unique opportunity for prolonged observation, enabling the study of the properties and behaviors of neutron stars in great detail. Detecting these requires operating GW detectors over long periods to accumulate enough data to identify

the weak signals amid noise. The detection and analysis of continuous GW can provide valuable insights into the internal structure of neutron stars, the state of matter at extremely high densities, and the dynamics of strong gravitational fields.

1.2.3. Bursts

Burst GWs are from unmodeled sources, like an asymmetric core collapse supernova, gamma ray bursts, cosmic strings and other unknown sources. These signals have durations of milliseconds to a few seconds in GW instruments [8]. It is difficult to predict how GWs from bursts would appear in the detector data because all the physics about the system may not be known. These systems also require complex numerical models that account the physics processes such as relativistic effects and neutrino transport. For a confident detection of a GW signal from a burst source, coincident observations of the signal in several detectors would be necessary.

1.2.4. Stochastic Background

The GW stochastic background is a pervasive, diffuse background of GWs arising from the superposition of numerous weak, unresolved sources. Unlike individual signals that are localized in space and time, the stochastic background is akin to a cosmic GW noise, continuously present and stemming from a variety of astrophysical and cosmological sources [9]. These sources include the combined effect of countless binary mergers of black holes and neutron stars, rotating neutron stars, and possibly even remnants from the early universe, such as cosmic inflation or phase transitions. Collapsing binary systems are numerous and can originate from a multitude of different directions forming an astrophysical stochastic background. The early universe, being dynamic and inhomogeneous, would

generate a cosmological stochastic background that is detectable by ground-based instruments. We search for any stochastic background, but it is expected that the astrophysical background is larger than the cosmological background. Studying the stochastic GW background can provide profound insights into the population and evolution of compact objects, as well as fundamental clues about the early universe. Its detection and analysis hold the promise of unlocking new aspects of the history of the universe and the underlying physics governing its evolution.

1.3. Observations of Gravitational Waves

The Laser Interferometer Gravitational-Wave Observatory (LIGO) and Virgo Collaboration (located in Cascina, Italy) have completed three observation runs and the O4 run is currently in progress. The first observing run (O1), spanned from September 12, 2015 to January 19, 2016, and was marked by the detection of three BBHs GW [10]. The O2, from November 30, 2016 to August 25, 2017, expanded these findings by identifying seven more BBH mergers [11] and most notably, the first detection of GWs from merger of two neutron stars [12]. The O3, operational from April 1st, 2019, to March 27th, 2020, observed a total of 74 GWsignals [13, 14]. O4 began on May 24, 2023 with the aLIGO and KAGRA (located underground in the Kamioka mine near Toyama, Japan) instruments observing. The first half of the fourth observation run (O4a) ended on January 16, 2024, with 81 GW detections with a false alarm rate (FAR) of 1 per 5 months. This included GW230529, the first confident detection of a GW signal from a binary system with the primary component residing in the lower mass gap ($\sim 2-5\ M_{\odot}$) [15]. O4a was followed by a commissioning break with the second half of the fourth observing run (O4b) resum-

ing on April 10, 2024. Figure 1.2 shows the component and remnant masses from aLIGO, Virgo and KAGRA GW detections.

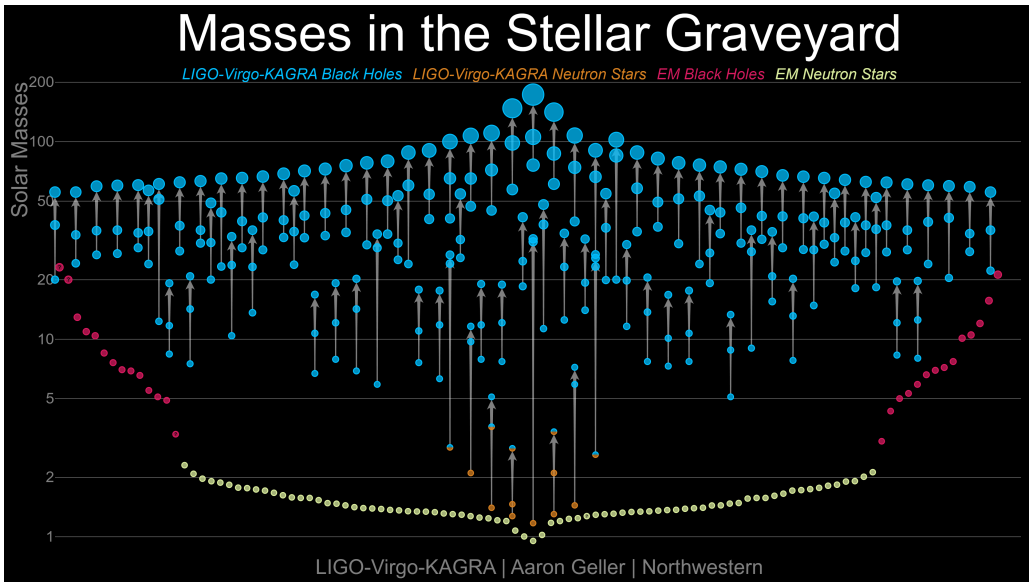

Figure 1.2. The masses of neutron stars and black holes measured from GW signals from the first three observation runs and GW230529. A gray line connects the component masses and the gray arrow points to the remnant mass. Masses from electromagnetic observations of neutron stars and black holes are also depicted [16].

1.4. Thesis Outline

Chapter 1 has provided a brief introduction to general relativity, an overview of gravitational wave sources, and a discussion of the detections of gravitational waves thus far. Chapter 2 gives an overview of the Advanced LIGO detector designs, discusses major noise sources. Chapter 3 describes transient noise in the instrument, detector characterization tasks and tools used for noise investigations and mitigation. In Chapter 4, I discuss loud transient noise, focusing on their characteristics and impact on the detectors. Chapter 5, I present my analysis of loud transient noise in auxiliary detector data channels. In chapter 6, I discuss analyses of transient noise that apply a machine learning algorithm to cluster data. Chapter 7, I present results from an experiment done to reproduce loud

transient noise and discuss potential sources of this noise. In chapter 8, I summarize the results of this thesis and discuss future loud transient noise research.

Chapter 2. Advanced LIGO Instrumental Design

The aLIGO instruments are a pair of specialized long-baseline interferometers used to measure small perturbations in spacetime. Upgrades to the LHO and LLO detectors enhance their sensitivity, thereby expanding the observable volume of space where detections can be made. Enhancements such as new optics, increased laser input power, and advanced quantum optic techniques were key factors in improving detector sensitivity from O3 to O4. This chapter delves into the hardware of the interferometers, as well as the fundamental and technical noise sources that limit their sensitivity.

2.1. Interferometer Design

LIGO employs a technique based on the Michelson interferometer, Figure 2.1, to measure the interference of laser beams at the detector output. Since the speed of light is constant in all inertial frames, the deformation of spacetime due to GWs can be measured by the light travel time of the interferometer lasers beams. A laser beam is injected into the interferometer via the symmetric port. The Michelson interferometer uses a 50/50 beam splitter to split the input laser light down orthogonal arms. The light travels down each arm and resonates within the cavity. At the end of each arm cavity is a highly reflective mirror that reflects the beam back to the beam splitter, where the light is recombined. At the anti-symmetric port of the interferometer, a photodiode is used to measure the recombined light. The aLIGO instruments are configured to allow for destructive interference at the photodiode when no GW is present. When a gravitational wave is present, it introduces a phase shift due to the stretching and compressing of spacetime, thus changing lengths of the detector arms. This phase overlap of the recombined beams is sensed by the

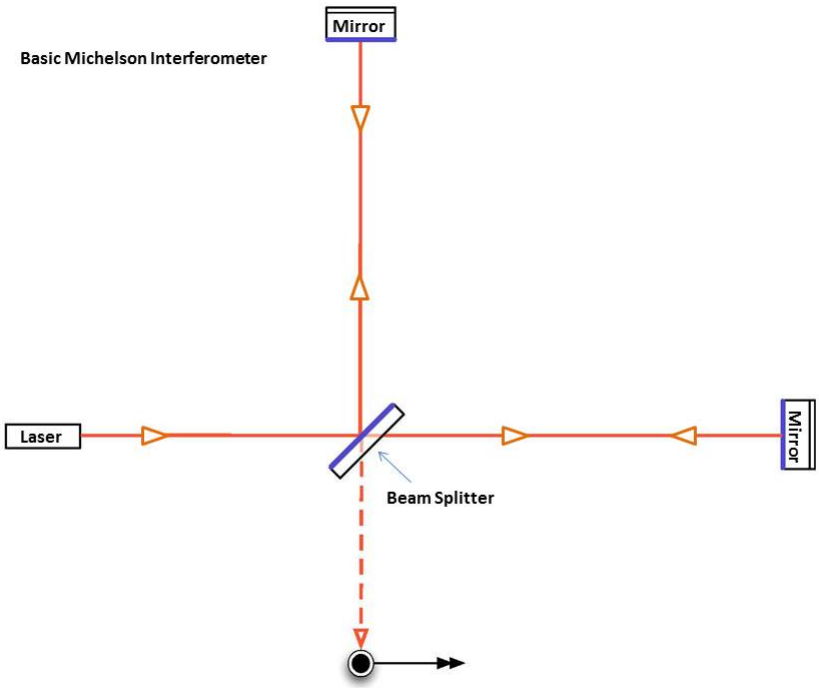

Figure 2.1. Schematic of a simple Michelson interferometer [17]. The aLIGO arms are 4 km in length.

photodiode, allowing the detection of GWs.

A Michelson interferometer with 4 km arms does not provide the sensitivity necessary to measure the tiny strain perturbation derived in section 1.2.1. To provide the necessary sensitivity, the aLIGO detectors incorporate several advanced technologies beyond a simple Michelson interferometer. This includes, but is not limited to, Fabry-Perot cavities, recycling cavities, and squeezed light. A schematic of the detectors is shown in Figure 2.2. The goal of the additonal technology is to substantially improve the sensitivity to GW signals and increase the astrophysical range of the aLIGO instruments. The remainder of this section will discuss aspects of the detector hardware.

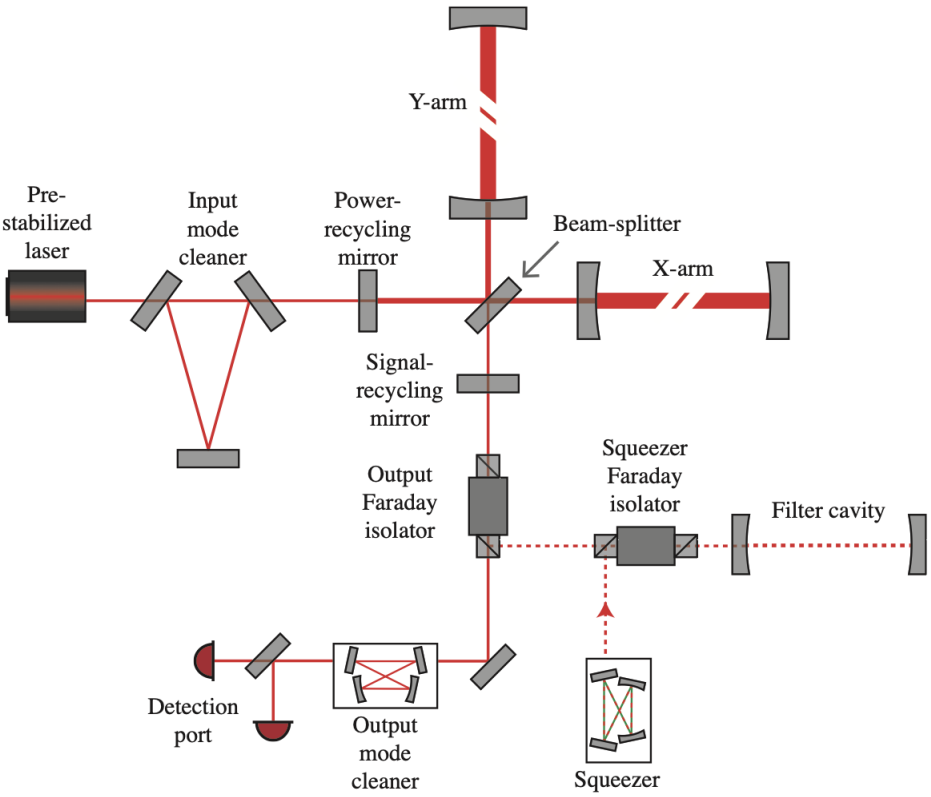

Figure 2.2. Schematic of the aLIGO detectors optical layout [18]. Note the solid red line represents the path of the main interferometer carrier light and the dashed red line is the path of squeezed light.

2.1.1. Pre-stabilized Laser and Input Optics

The aLIGO detectors use a 2 W NPRO 1064 nm laser source that is stabilized in frequency and intensity to reduce noise from the laser injected into the interferometer [18, 19]. The pre-stabilized laser is also amplified to increase the input laser power of the interferometer. For reference, during O4a LHO and LLO operated with an input power ranging between $60 - 75$ W [20]. The laser then passes through electro-optic modulators (EOM), which generates radio frequency sidebands used for sensing the length of the detector cavities. This will be further discussed in section 2.1.6. The laser light, and sidebands, enter a triangular mirror cavity known as the Input Mode Cleaner (IMC). The

IMC is responsible for eliminating higher order modes from entering the main interferometer and only allowing the fundamental Gaussian mode, TEM-00, to pass through.

2.1.2. Fabry-Perot Cavities

Each of 4 km arms of the aLIGO interferometer have an input test mass (ITM) just after the beam splitter. These mirrors are highly reflective ($\sim$ 97% in power), letting only a small amount of light transmission, forming a Fabry-Perot cavity with the end test mass (ETM) The light that is transmitted goes back towards the laser, or the symmetric port, and has constructive interference. The Fabry-Perot cavities effectively lengthen the cavity arms by allowing the light to reflect between the ITM and ETM several times before recombining at the beam splitter. This also increases the circulating power in the arm cavities and allows each arm to build up the phase shift produced when there is a change in arm length due to the resonance condition. For a plane-wave in a Fabry-Perot cavity, the electric field equations for the circulating (E_{circ}), reflected (E_{refl}) and transmitted (E_{trans}) beam can be written as [18],

$$E_{circ} = t_i E_{in} + r_i r_e e^{i2kL} E_{circ}, \tag{2.1}$$

$$E_{refl} = -r_i E_{in} + t_i r_e e^{i2kL} E_{circ}, \tag{2.2}$$

$$E_{trans} = t_e E_{circ}, \tag{2.3}$$

where t_i, r_i and t_e, r_e are the amplitude transmission and reflection coefficients of the ITMs and ETMs, respectively and k is the laser wave number. Using equation 2.1 we solve

for E_{circ} in terms of E_{in} and E_{circ}, E_{refl}, and E_{trans} can be rewritten as

$$E_{circ} = \frac{t_i}{1 - r_i r_e e^{i2kL}} E_{in}, \tag{2.4}$$

$$E_{refl} = \frac{-r_i + (r_i^2 + t_i^2) r_e e^{i2kL}}{1 - r_i r_e e^{i2kL}} E_{in}, \tag{2.5}$$

$$E_{trans} = \frac{t_i t_e e^{ikL}}{1 - r_i r_e e^{i2kL}} E_{in}. \tag{2.6}$$

We can analyze the resonant condition of the Fabry-Perot cavity with equation 2.4, in the case where $r_i r_e$ is chosen to be close to one. The cavity achieves maximum circulating power when e^{i2kL} is equal to one, which is the case when $2kL = 2n\pi$, with n being any positive integer value. The resonance condition of cavity length L is now,

$$L = \frac{\lambda}{2} n, \tag{2.7}$$

and λ is the wavelength of the laser.

Another important parameter of the the Fabry-Perot cavity is the cavity pole, f_p. By setting the denominator of equations 2.4, 2.5, and 2.6 equal to zero, we get:

$$if_p = -\frac{1}{2\pi} \frac{c}{2L} log(r_i r_e), \tag{2.8}$$

where c is the speed of light. The cavity pole signifies the frequency where the the cavity response to changes in lengths falls off by half.

2.1.3. Dual Recycled Michelson Interferometer

Mirrors are placed at the symmetric and antisymmetric port of the main interferometer forming what is known as dual recycling cavities. The aLIGO detectors are operated near a dark fringe, where the beams returning from the two arms almost perfectly

interfere, directing most of the returning light back towards the symmetric port. To further enhance sensitivity, a partially transmitting mirror is placed between the input of the interferometer and the beamsplitter, forming a Power Recycling Cavity (PRC). The PRC allows the detector to have a higher circulating power in the Michelson Interferometer and even more in the Fabry-Perot cavities. At the anti-symmetric output, after the beam splitter, of the Michelson we introduce another mirror, thus forming the Signal Recycling Cavity (SRC). The SRC broadens the frequency response of the detector by changing the cavity finesse. The finesse is a measure of the sharpness of the resonance peaks and is defined in terms of the free spectral range (FSR) and full width at half maximum (FWHM) of the optical cavity,

$$\mathcal{F} = \frac{FSR}{FWHM}. \tag{2.9}$$

Both the PRC and SRC are designed to be stable cavities. The stability condition for a two-mirror cavity is expressed as, $0 \leq g_1 g_2 \leq 1$, where the parameter g_i is related to the mirror radii of curvature R_i and the cavity length L [21],

$$g_i = 1 - \frac{L}{R_i}. \tag{2.10}$$

2.1.4. Output Mode Cleaner

The Output Mode Cleaner (OMC) is comprised of four mirrors arranged in a bowtie, which allows the GW signal to be transmitted to the readout photodiode. The radio frequency sidebands generated at the input of the interferometer are rejected by the OMC, as they would contribute noise at the detector output. The photodiode at the output detects the light from the interferometer due to changes in length. The GW readout method is discussed in section 2.2.

2.1.5. Squeezed Light

A major upgrade to the aLIGO instruments is the addition of squeezed light to increase sensitivity. The instrument is limited by quantum noise sources due to the Heisenberg uncertainty principle, further discussed in 2.3.1. During O3, frequency-independent squeezed light was introduced, which reduced the uncertainty in the phase quadrature of the laser beam, thus reducing quantum noise at high-frequency [22], but worsening noise at low-frequency. During O4, frequency-dependent squeezing was implemented using a 300 m filter cavity to rotate the squeezed vacuum quadrature depending on the frequency [23–25]. This allows for a reduction in phase and amplitude uncertainty, reducing noise across the detector bandwidth.

2.1.6. Interferometer Sensing and Control

Feedback control loops maintain the stability of the optical cavities in the aLIGO detectors, ensuring proper instrument operation. Without a feedback control system, the mirrors move freely, causing movements too large to maintain resonance in the various cavities. To measure the length and angular alignment of the optics, the main carrier is modulated at 9 MHz, and sidebands at 9 MHz, 36 MHz, 45 MHz, and 72 MHz are used. Photodiodes are placed at several locations around the detector, depicted in Figure 2.3, and linear combinations of their signals are used to sense the interferometer degrees of freedom and actuate the appropriate mirrors and maintain resonance in the cavities. There are five length degrees of freedom that are controlled by the LSC system, Figure 2.3: DARM, Common Arm Readout Measurement (CARM), Michelson Length (MICH), Power Recycling Cavity Length (PRCL) and Signal Recycling Cavity Length (SRCL).

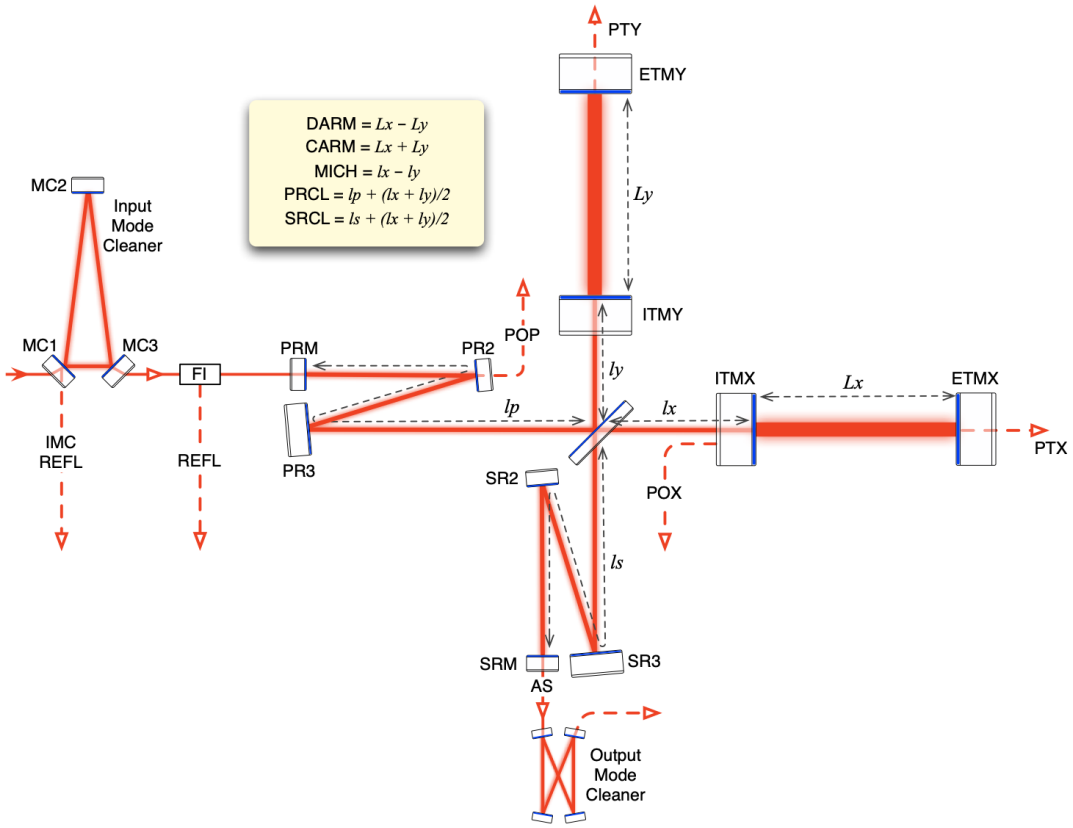

Figure 2.3. Interferometer layout showing LSC and ASC system detection ports. Photodiode port acronyms: REFL, reflection port; POP, PRC pick-off; POX, X arm pick-off; AS, anti-symmetric port; PTX/Y, transmitted power X/Y arm. The LSC degrees of freedom are also defined.

The detector optics are controlled angularly in pitch and yaw by the ASC system. Pitch refers to the up-and-down tilting of an optic around its horizontal axis, while yaw describes the left-and-right swiveling around its vertical axis. Each arm cavity of the detector can be treated as a unit that has two orthogonal modes, the hard and soft angular modes, Figure 2.4. The hard mode represents the rotational motion of the mirror whereas the soft mode represents the transnational motion. Hard modes increase the stability of the cavity while soft modes decrease the cavity stability. There are four modes of angular motion: Common Hard (CHARD), Differential Hard (DHARD), Common Soft

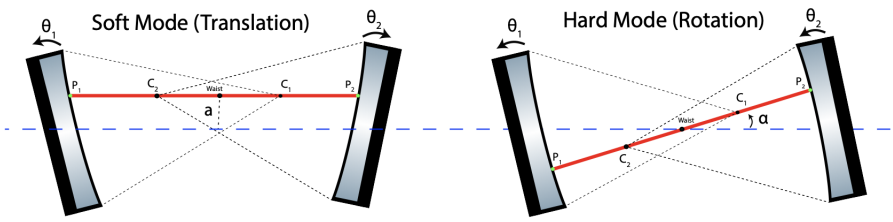

Figure 2.4. The arm cavity hard and soft modes [26].

(CSOFT), and Differential Soft (DSOFT). There are also ASC control loops for the PRC, SRC, MICH, amongst others. Together, the interferometer sensing and control system supports the stability of the aLIGO detectors.

2.2. Gravitational Wave Readout Method

The DARM degree of freedom is used for the detection of GW signals. The motion from $h = 10^{-21}$ is equivalent to a change in length of 4×10^{18} m. To minimize the motion coupling into the DARM signal, the ITMs and ETMs are suspended using quadruple stage suspensions, and active seismic isolation systems are also employed, see section 2.3.3. Low-frequency ground motion and other external forces (ΔL_{ext}) are suppressed to a residual DARM length (ΔL_{res}) by the LSC system, which has an open loop transfer function, G, where

$$\Delta L_{res} = \frac{\Delta L_{ext}}{1+G}. \tag{2.11}$$

The DARM loop, shown in 2.5 is comprised of three transfer functions: sensing function $C(f)$, digital filters $D(f)$, and actuation function $A(f)$ [27, 28].

When a GW passes through the interferometer, it introduces motion in DARM as ΔL_{ext}. The sensing function, $C = \frac{d_{err}}{\Delta L_{res}}$, converts the arm displacement into the GW readout signal, d_{err}. Next, signal is then processed by a digital filter bank, $D = \frac{d_{ctrl}}{d_{err}}$, to

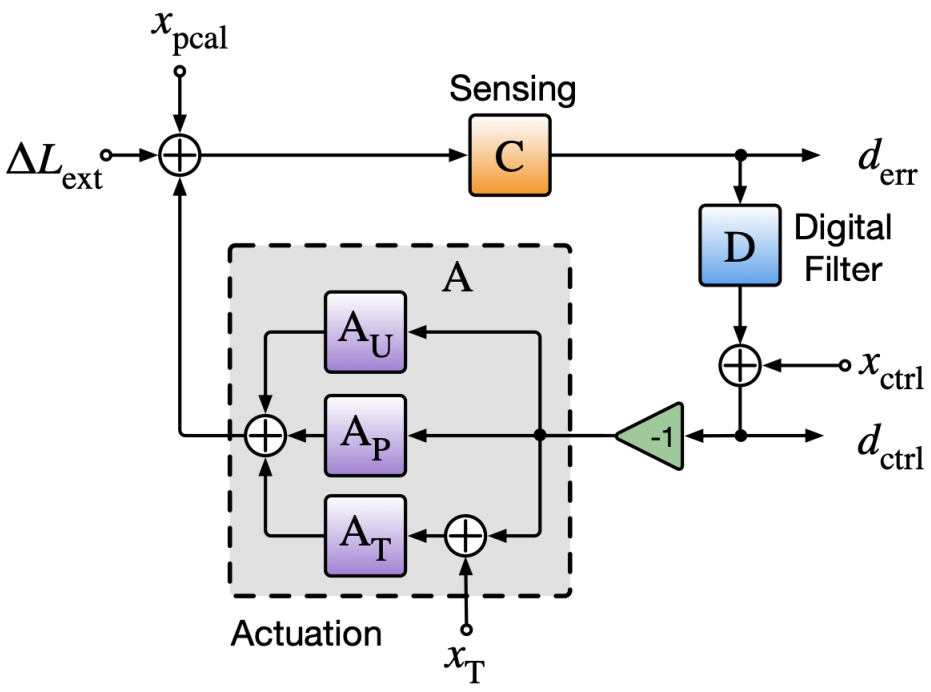

Figure 2.5. Schematic of the DARM control loop [28].

produce the DARM control signal, d_{ctrl}. The actuation function, $A = \frac{\Delta L_{ctrl}}{d_{ctrl}}$, is divided into three actuation functions, A_U, A_P, and A_T, for the upper-intermediate, penultimate and test mass stages of suspension respectively [28]. These actuation functions model the amount of DARM displacement is induced in the interferometer by applying d_{ctrl} to the actuators on the bottom three stages of the quadruple suspension system. Thus, the DARM open loop transfer function is given by

$$G = A(f)D(f)C(f). \tag{2.12}$$

When the laser interacts with the mirrors, the phase of the light is ingrained with the motion of the mirror. By measuring the phase of two interfering beams, information about the GW signal is extracted via DC readout. The aLIGO detectors uses the DC readout technique known as Homodyne detection. There is a picometer-scale DARM off-

set to allow for 20 mW of light to be detected at the asymmetric port photodiode [18], creating a reference field, or local oscillator. Operating slightly away from the dark fringe allows for a linear response to the amount of power detected due to changes in length. In the presence of a GW, the reference field beats against the carrier light, which contains the GW signal and the total amount of light on the photodiode is measured. This method for readout vastly reduces the amount of power that must be detected at the output and is less susceptible to certain technical noise couplings.

2.3. Instrumental Noise Sources

Instrumental noise sources in the aLIGO detectors play a critical role in determining the sensitivity to GW observations. These noise sources, which can be both fundamental and technical (Figure 2.6), arise from a variety of physical processes and environmental factors that affect the performance of the instrument. Fundamental noise sources include quantum noise, thermal noise, and seismic noise, all of which stem from intrinsic properties of the materials and technologies used in the detectors. Technical noise sources, on the other hand, result from imperfections in the detector design and operation, such as electronics noise, scattered light, and control system noise. The aLIGO noise budget is represented as an amplitude spectral density (ASD). For a time-domain signal $x(t)$, the amplitude spectral density $S(f)$ is defined as the square root of the power spectral density (PSD) $P(f)$:

$$S(f) = \sqrt{P(f)}, \tag{2.13}$$

where $P(f)$ is the power spectral density at frequency f and $S(f)$ is the amplitude spectral density at frequency f. The units of amplitude spectral density depend on the units

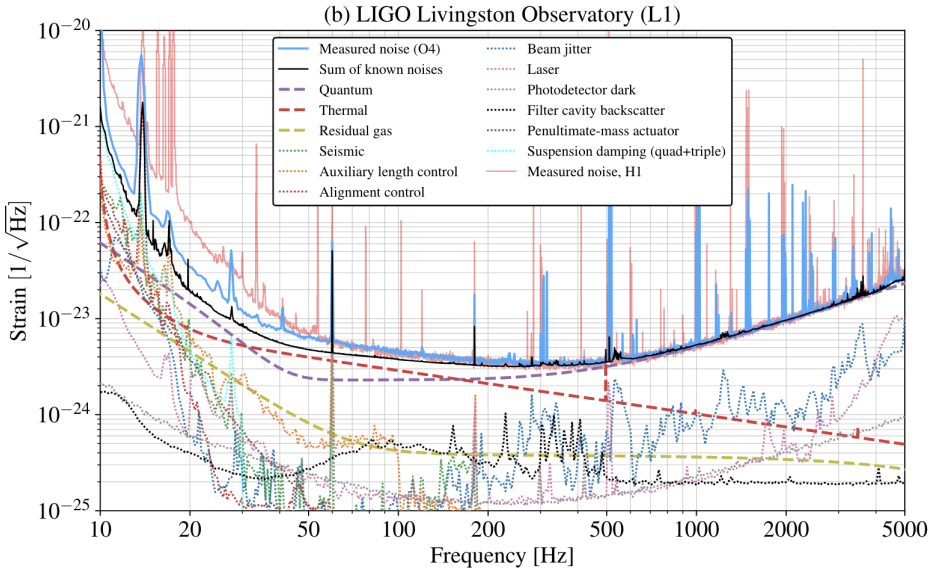

Figure 2.6. LLO noise budget for O4 depicting major sources of fundamental and technical noises [20]. Solid lines represent calculated noises and dots show measured and projected noises. The black line is the sum of budgeted noises from the instrumental design, while the blue line shows the measured detector noise. At 500 Hz and above, the vertical lines are the "violin" modes of the fibers that suspend the test masses.

of the original signal. If the signal is measured in meters, the ASD is in meters per square root of hertz ($\mathrm{m}/\sqrt{\mathrm{Hz}}$), or in Figure 2.6 it is given in units of strain ($1/\sqrt{\mathrm{Hz}}$). The ASD provides information about the magnitude of different frequency components within the signal. A higher value at a particular frequency indicates that the signal has a stronger component at that frequency. Understanding and mitigating these noise sources is essential for enhancing the instrumental sensitivity and increasing the amount of GW singals detected from astrophysical sources.

2.3.1. Quantum Noise

Quantum noise is a fundamental limit to the sensitivity of the aLIGO detectors, arising from the quantum mechanical nature of light. It consists of two main components: shot noise and radiation pressure noise. These noise sources are a consequence of the

Heisenberg Uncertainty Principle, which imposes a limit on the simultaneous measurement precision of the amplitude and phase of the light field within the interferometer. The relationship between amplitude and phase uncertainty is

$$\sigma_{amp}\sigma_{phase} \geq \frac{\hbar}{2}. \tag{2.14}$$

This means that increasing the accuracy in measuring the amplitude of light necessarily leads to greater uncertainty in the measurement of its phase, and vice versa.

Shot Noise

Shot noise, also known as photon shot noise, originates from the discrete nature of photons. In aLIGO, shot noise primarily affects the high-frequency region of the detector's sensitivity band (above a few hundred Hertz). It arises due to the statistical fluctuations in the number of photons arriving at the photodetectors. When a GW passes through the interferometer, it induces a differential phase shift in the light returning from the two arms, which is then detected as a change in the interference pattern. However, the detection process is limited by the inherent noise due to photon statistics. Shot noise can be described in terms of strain with a white noise ASD [29], given by

$$h_{shot}(f) = \frac{1}{L}\sqrt{\frac{\hbar c\lambda}{2\pi P_{in}}}. \tag{2.15}$$

In equation 2.15, the arm cavity length is L and the input power is P_{in}. Increasing the laser power can reduce shot noise by increasing the number of photons, but the increased number of photos impart a force on the optics causing motion, referred to as radiation pressure noise.

Radiation Pressure Noise

Radiation pressure noise, in contrast to shot noise, dominates at low frequencies (below a few tens of Hertz) due to the $\frac{1}{f^2}$ dependency on frequency (equation 2.16) [29]. The strain noise due to radiation pressure noise is,

$$h_{rpn} = \frac{1}{mf^2L}\sqrt{\frac{\hbar P_{in}}{2\pi^3 c\lambda}} \tag{2.16}$$

It is caused by the quantum fluctuations in the momentum of the photons that exert a force on the interferometer's mirrors. The optics, suspended as pendulums to isolate them from seismic noise, experience minute displacements due to the random photon momentum transfers, leading to noise in the measurement of GW. The effect of radiation pressure noise increases with higher laser power, creating a trade-off with shot noise. Balancing this trade-off is crucial for optimizing the overall sensitivity of the detector.

2.3.2. Thermal Noise

Thermal noise is a significant source of noise in the aLIGO instruments, arising from the thermal fluctuations of atoms and molecules within the detector components. The movement of atoms is driven by the thermal energy present at any non-zero temperature, which induces random motion in materials. Thermal noise primarily originates from mechanical losses from the test masses and the suspension systems [30, 31]. The test masses are subject to Brownian motion due to their internal temperature. This motion causes fluctuations in the mirror surfaces, introducing noise into the measurement of the beam position and phase. Additionally, the fused silica fibers used to suspend the optics and optic coatings are affected by thermal noise, that translates to displacement of the mirrors. Ongoing research, including new materials for future optic coatings, and techno-

logical advancements continue to improve the mitigation of thermal noise, enhancing the overall performance of the aLIGO detectors [32].

2.3.3. Seismic Noise

Seismic noise from the motion of the Earth is one of the primary low-frequency noise sources that affect the sensitivity of the aLIGO detectors. It originates from ground vibrations caused by a variety of sources, including natural phenomena such as earthquakes, weather conditions and ocean waves, as well as human activities including traffic and industrial operations. The noise spectrum due to ambient seismic noise is expressed as [29],

$$x(f) = 10^{-7} \frac{cm}{\sqrt{Hz}} \left(\frac{10 \text{ Hz}}{f} \right)^2, \tag{2.17}$$

for $f > 10$ Hz. Without any isolation from seismic noise, the instruments would not be able to maintain resonance. These vibrations couple into the interferometer and cause mirror movements, which introduce noise into the GW signal.

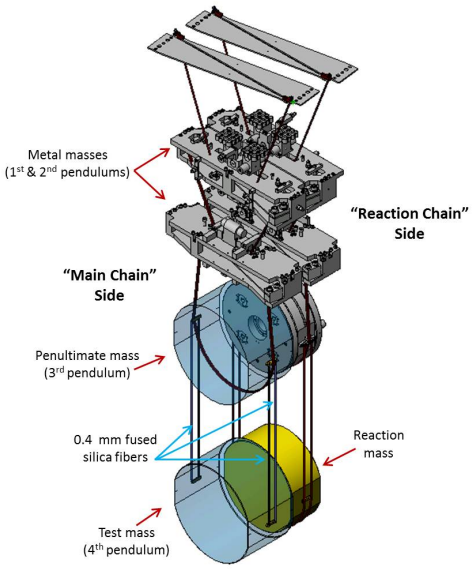

Figure 2.7. aLIGO quadruple pendulum suspension diagram [33].

To mitigate seismic noise, aLIGO employs a sophisticated seismic isolation system. The test mass optics are suspended by a quadruple-stage pendulum for passive isolation from the ground motion [34]. The pendulum chain is also suspended from an active seismic isolation system, which uses hydraulic actuation structures as well as piezoelectric transducers [35]. The active and passive seismic isolation provides enough attenuation from the ground motion for the optical cavities to maintain resonance. Despite the advanced isolation systems, some residual seismic noise still couples into the interferometer.

2.3.4. Technical Noise

Technical noises are those that are not inherit to the design of the aLIGO instruments. There are several sources of technical noise, some of which I will discuss briefly. At low-frequency, feedback control system noise dominates, which arises from imperfect sensing signals and noisy actuation [36, 37]. This can lead to misalignments of the interferometer optics. Residual gas noise, caused by the presence of small amounts of gas in the vacuum chambers, can also introduce noise. During commissioning of the instrument, vacuum chambers may be vented to allow upgrades and maintenance of hardware. After a vent the chambers are pumped down to restore vacuum conditions, but the amount of residual gas and the gas composition may be different from previous levels. A more detailed discussion of residual gas noise will be presented in Chapter 7. Additionally, dark noise from the photodiodes, contributes noise due to the intrinsic electronic and thermal properties of these detectors. Actuator noise, originating from imperfections in the actuators used to position and control the mirrors, and electronic noise from various components, also add to instrumental technical noise. Technical noises should be controlled to

be below the noise floor set by fundamental noise sources, however aLIGO has not reached this limit yet.

2.4. Conclusion

The aLIGO detectors represent a remarkable achievement in engineering and physics, enabling the detection of GW signals with unprecedented sensitivity. The design and operation of these interferometers incorporate cutting-edge technologies such as advanced optics, sophisticated feedback control systems, and innovative seismic isolation techniques. These elements work together to minimize various sources of noise, both fundamental (such as quantum, thermal, and seismic) and technical (including electronic and residual gas noises), which would otherwise limit the sensitivity of the instruments. The integration of squeezed light technology during O3 and O4 marks a significant enhancement, reducing quantum noise and increasing the astrophysical range of the instrument. Ongoing advancements and refinements continue to push the boundaries of GW detection, promising even greater discoveries and insights into the astrophysical universe.

Chapter 3. Transient Noise in Advanced LIGO

The LIGO detectors are riddled with transient non-Gaussian noise, commonly referred to as glitches. Transient noise is different from the fundamental noises discussed in the previous chapter. Glitches vary in time, frequency, and amplitude, with new morphologies arising as instrumental upgrades occur [38]. Glitches arise in LIGO data due to the environmental and instrumental conditions [39]. This noise appears in the GW readout signal, even when the detector is in its nominal state. Glitches contribute to the overall loudness of the instrumental noise background, leading to several problems for GW search methods, such as decreasing the significance of candidate signals, corrupting data, reducing the amount of data used in analyses, and biasing astrophysical parameter estimation [40]. In this chapter, I will discuss transient noise in the LIGO detectors and methods used to characterize and investigate glitches.

3.1. Data Quality Challenges Due to Transient Noise

Transient noise poses a problem for GW detection methods as they can affect the recovery of the signal. They occupy the same frequency bandwidth as genuine astrophysical signals, leading to the potential overlap of glitches with GW signals. When noise occurs during or near a GW signal, time and/or frequency intervals around the noise are removed from the analysis window, or the glitch may be subtracted [41] from the data for parameter estimation analyses. The method used depends if the noise is long in duration, has multiple glitches or is a single short duration glitch. During GW170817, the detection of the first GW signal from binary neutron stars, a short duration glitch was observed at LLO [12]. In this case, the glitch was subtracted from the LLO data and the data with the

glitch removed was used for analysis.

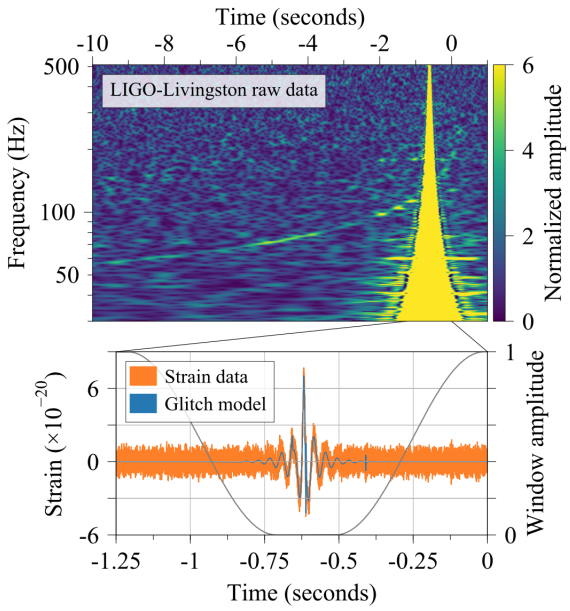

Figure 3.1. *Top*: Time-frequency spectrogram of GW170817 in LLO raw data. A loud, short duration transient is visible before the merger time at t = 0 s. *Bottom*: Time series data of the loud, short transient [12].

Although LIGO scientists have techniques to reduce the impact transient noise has on the recovery of candidate signals, applying these methods leads to delays in reporting sky localization of GW candidates. Rapid reporting of sky localization is essential for multi-messenger observations of BNS and NSBH mergers.

A key signature of a GW candidate is consistent waveforms that occur in each detector, and the time between each signal is within the 10 ms light intersite propagation time [4]. Transient noise occurs independently in each instrument, but frequently enough to cause false GW alerts. When a false GW signal occurs the candidate must be retracted. During O3 there were 24 retractions (74 detections) and during O4a there were 11 retractions (81 detections) due to data quality issues caused by transient noise. To reduce the number of retracted GW signals, it is imperative to mitigate and reduce glitches by char-

acterizing the aLIGO instruments.

During O4, I co-led the Noise Mitigation Review Team, which is responsible for determining if transient noise present in the analysis window of a GW candidate requires follow-up measures [42]. This also includes recommending the time-frequency analysis window for parameter estimation and assessing GW data frames after noise mitigation processing. It is a priority to ensure good data quality, although transient noise may occur during GW candidate signals.

3.2. Detector Characterization Overview

Detector Characterization encompasses various activities aimed at monitoring detector status and ensuring the high quality of LIGO data. This is a working group in the LIGO Scientific Collaboration. These activities include identifying and mitigating transient noise, monitoring data quality during observation runs, validating gravitational wave candidates, vetoing poor data quality segments, analyzing data from the various detector subsystems and maintaining various noise analysis tools. The detector characterization group interfaces with the instrumentation and data analysis groups, communicating findings to improve detector performance and GW search methods.

Noise investigations rely on a large number (tens of thousands) of data-streams, or auxiliary channels, which monitor interferometer and the surrounding environment [40]. Auxiliary channels monitor photodiodes, actuators, electronic devices, feedback control loops and environmental sensors (e.g., thermal, seismic, and magnetic). With the exception of some interferometer sensing and control channels, the vast majority of these channels are not sensitive to GW signals. These auxiliary channels are thus used as witnesses

to noise artifacts in the detector data. We often search for transient noise events in these witness channels and correlate them to the environmental or instrumental sources. Once a coupling source for the noise is identified, hardware or software upgrades are made to reduce the rate of the glitches.

The LIGO Detector Characterization Summary Pages [43] are regularly updated webpages that provide an overview of the performance and environmental conditions of the LIGO instruments. From the summary pages we gain insight on the behavior of interferometer subsystems, transient noise rates, detector sensitivity and seismic noise, among other factors. One way we quantify the sensitivity is by calculating the BNS range. This range signifies the sky-average distance at which a GW signal from the merger of two 1.4 $M_\odot$ neutron stars would be detected with an SNR of 8 [44]. The BNS range is shown for a day during O4a in figure 3.2, along with the rate of transient noise for that day. The summary pages offer a convenient method for monitoring data quality and comparing the primary GW channel with other relevant auxiliary channels.

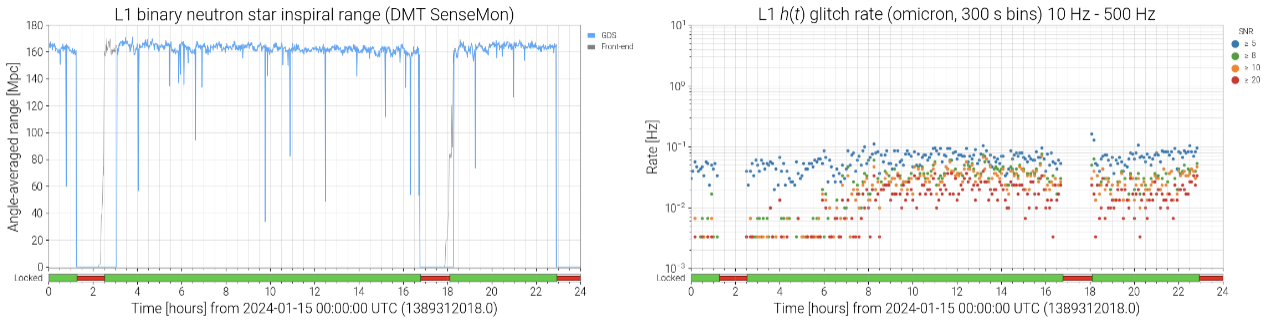

Figure 3.2. *Left*: LLO BNS range plot from the Detector Characterization Summary Pages on January 10, 2024. The BNS range for this day is $\sim$ 160 Mpc. *Right*: The rate of transient noise in the GW strain channel on January 10, 2024. The color of the points represents the SNR of the glitches.

The detector characterization group also creates and maintains software tools to

monitor and assess detector status and data quality. These tools provide key information about transient noise in the GW strain channel and auxiliary channels. In the following section, I will provide descriptions of key detector characterization tools utilized by LIGO researchers.

3.3. Characterization Tools for Data Quality

3.3.1. Omicron

Omicron is an unmodeled or 'burst' transient identification algorithm which generates triggers for excess power events with SNR large than 7.5 in the primary GW and auxiliary data channels [39, 45]. These events are referred to as omicron triggers or triggers. Each trigger identified is given parameters by the algorithm including event time, SNR, frequency, duration, bandwidth and others. These parameters assist in characterizing transient noise in the detectors.

Omicron searches for transient signals by projecting the data onto a basis of complex-valued sinusoidal Gaussian (sine-gaussians) functions that span the time-frequency parameter space. Sine-gaussians also depend on a third parameter called quality factor, Q-factor or Q. The Q-factor is the width of the Gaussian envelope of the sine-gaussian and the frequency of a sine-gaussian is defined by the central frequency of its sinusoidal component. The transform coefficient, X, is a measure of the average amplitude and phase of a time-frequency space [45]. This space is referred to as a tile.

$$X(\tau, \phi, Q) = \int_{-\infty}^{+\infty} x(t) w(t - \tau, \phi, Q) e^{-2i\pi\phi t} dt \tag{3.1}$$

Tiles create a 3-dimensional space with linearly-spaced time tiles, logarithmically-spaced frequency rows and logarithmically-spaced Q planes. Here, the Q of a trigger is defined as

the ratio of its resonance, or central, frequency and its bandwidth.

$$Q = \frac{f}{\Delta f} = 4\pi f \Delta t \tag{3.2}$$

For each plane, the Q value is constant and there are multiple tiles. The time-frequency uncertainty of an event is measured by the duration, Δt, and bandwidth, Δf. As the Q-factor increases, the duration increases as the bandwidth decreases for a fixed frequency. Based on the plane with the greatest signal energy, Omicron assigns a trigger an event time and peak frequency from the central time and central frequency of the tile with the highest SNR [46].

3.3.2. Omega-scans

The `gwdetchar-omega` [47, 48] algorithm is used to visualize noise in the GW strain and auxiliary data in time, frequency and energy.

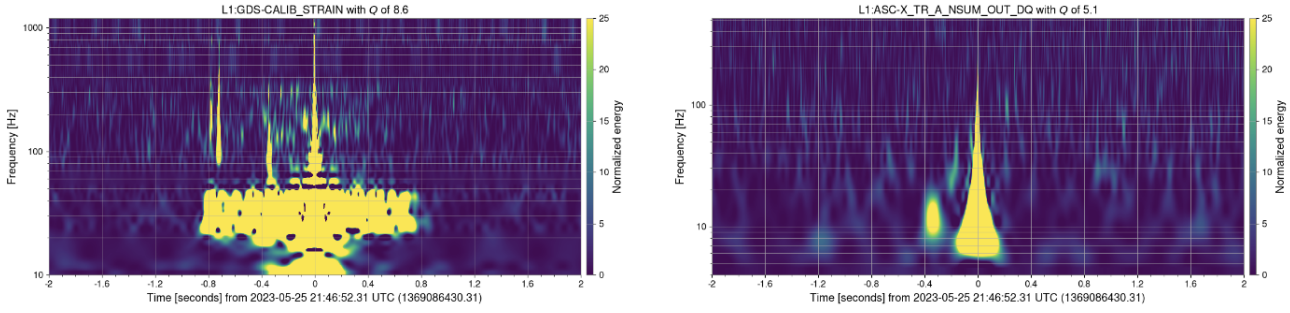

Figure 3.3. *Left*: An omega-scan of a loud noise transient in the GW strain data. *Right*: An omega-scan of a coincident transient in an auxiliary data channel. The morphology of the glitch is different in the auxiliary channel in comparison to the GW channel due to their different sensitivities to noise.

Examining noise triggers in this domain enables the classification of noise triggers based on their distinct morphologies. These various shapes provide insights into trigger

characteristics that may not always be apparent in the raw time series data. The algorithm uses the time series of a trigger to produce a whitened spectrogram, referred to as an omega-scan or Q-scan. To produce the omega-scans, the algorithm uses a configuration file with channel names, frequency range, SNR threshold, duration of the scan amongst other parameters. The omega-scan is created by providing the time of the trigger to the algorithm. Users also have the option to create Q-scans for multiple trigger times using `gwdetchar-omega-batch` and a text file containing a list of times.

3.3.3. Hierarchical-Veto

Hierarchal-Veto, or H-veto, is a tool which uses Omicron triggers to find correlations between the GW strain and auxiliary channel data. The H-veto algorithm identifies and removes noise in the strain data by identifying statistical correlations between noise in the GW and auxiliary data [49]. For "safe" auxiliary channels, or channels that are not sensitive to GW signals, the algorithm searches for coincident triggers with the primary GW channel within the desired time window. The safe channels found to be statistically significance are ranked and triggers from these channels are used to "veto", or remove noise, from the GW data.

The significance of a channel is a measure of how unlikely the observed coincidences came from the overlap of two random Poissonian time distributions, each with identical occurrence rates and time windows. The significance is given by,

$$S = -log_{10}\left(\sum_{k=n}^{\infty} P(\mu, k)\right) \tag{3.3}$$

where n represents the number of observed noise coincidents between the auxiliary and GW channel during a period of time and $P(\mu, k)$ is the Poisson probability density func-

tion (PDF). The Poisson PDF is given by,

$$P(\mu, k) = \frac{\mu^k e^k}{k!},\ \mu = \frac{N_h N_{aux} t_{win}}{T_{total}} \tag{3.4}$$

and μ is the expected number of coincidences that occur by chance between the the primary and auxiliary channel in a time window, T_{win}, N_h and N_{aux} are the number of observed triggers during a period of time, T_{total}, in the GW channel and auxiliary channel, respectively.

The H-veto algorithm works in a hierarchical method, proceeding in rounds. In the first round, the significance is calculated for the safe channels, and the coincident triggers from channel with the greatest significance are used to construct the vetoes to remove these time segments from the primary channel. By removing these periods of poor data quality from the GW channel, when H-veto is run for the second round a new auxiliary channel is found to be significant and the vetoing processes begins again. H-veto continues this method until the significance of the round "winner" auxiliary channel falls below a minimum threshold.

The `gwdetchar-omega` algorithm is also used to produce q-scans for each H-veto round. Omega-scans are generated for five randomly selected instances of vetoed triggers in the primary GW channel, along with the auxiliary channels identified in each round. The results of daily H-veto runs and the omega-scans are published to the LIGO summary pages (Figure 3.4).

3.3.4. Gravity Spy

Gravity Spy harnesses machine learning models and human classification through a citizen science effort to classify transient noise triggers by morphology in the LIGO detec-

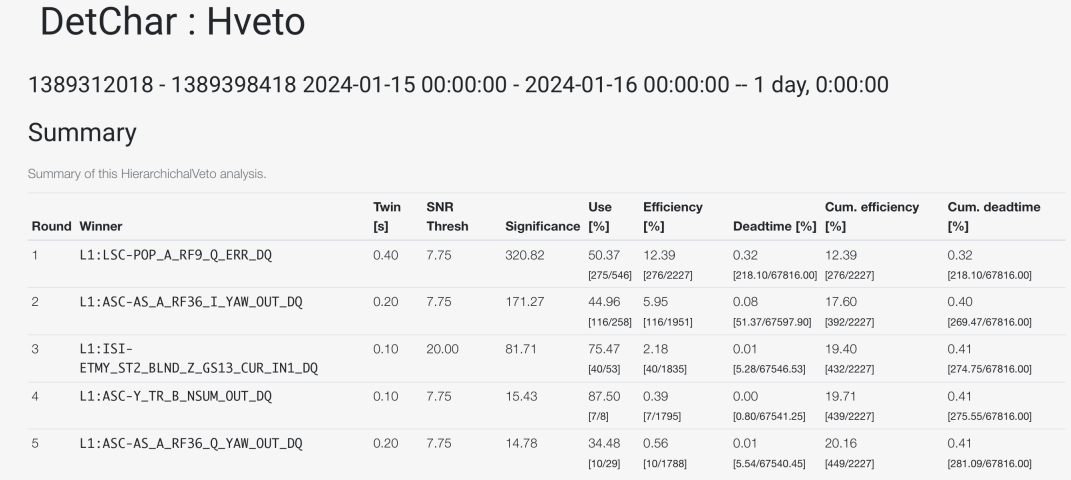

DetChar : Hveto

1389312018 - 1389398418 2024-01-15 00:00:00 - 2024-01-16 00:00:00 -- 1 day, 0:00:00

Summary

Summary of this HierarchichalVeto analysis.

Round	Winner	Twin [s]	SNR Thresh	Significance	Use [%]	Efficiency [%]	Deadtime [%]	Cum. efficiency [%]	Cum. deadtime [%]
1	L1:LSC-POP_A_RF9_Q_ERR_DQ	0.40	7.75	320.82	50.37 [275/546]	12.39 [276/2227]	0.32 [218.10/67816.00]	12.39 [276/2227]	0.32 [218.10/67816.00]
2	L1:ASC-AS_A_RF36_I_YAW_OUT_DQ	0.20	7.75	171.27	44.96 [116/258]	5.95 [116/1951]	0.08 [51.37/67597.90]	17.60 [392/2227]	0.40 [269.47/67816.00]
3	L1:ISI-ETMY_ST2_BLND_Z_GS13_CUR_IN1_DQ	0.10	20.00	81.71	75.47 [40/53]	2.18 [40/1835]	0.01 [5.28/67546.53]	19.40 [432/2227]	0.41 [274.75/67816.00]
4	L1:ASC-Y_TR_B_NSUM_OUT_DQ	0.10	7.75	15.43	87.50 [7/8]	0.39 [7/1795]	0.00 [0.80/67541.25]	19.71 [439/2227]	0.41 [275.55/67816.00]
5	L1:ASC-AS_A_RF36_Q_YAW_OUT_DQ	0.20	7.75	14.78	34.48 [10/29]	0.56 [10/1788]	0.01 [5.54/67540.45]	20.16 [449/2227]	0.41 [281.09/67816.00]

Figure 3.4. LLO Hierarchical Veto results from January 15-16, 2024. H-veto proceeds in rounds, each auxiliary channel listed is the winner channel for that round, based on significance calculated with a time window (Twin) and SNR threshold applied. The Use % is the fraction of auxiliary triggers used to veto triggers in the GW channel. The efficiency % refers to the percentage of triggers vetoed from the GW channel and the deadtime % is the percentage of time removed from analysis due to vetoes.

tors. Volunteers use omega-scans to classify different types of transient noise and the labeled glitches are used to train machine learning algorithms to identify new glitch classes, while also learning to classify noise in large datasets swiftly [38]. Gravity Spy uses Q-scans of omicron triggers from the GW channel to classify glitches by their morphology. Classified glitches are also assigned a confidence level ranging from 0 to 1. The different characteristics of the glitches allow LIGO scientists to analyze and characterize noise with the goal of reducing or mitigating glitches from the instrument.

Types of Transient Noise

There is a substantial variety of transient noise present in the LIGO detectors. Gravity Spy classifies these glitches in to categories based on their time-frequency morphologies and origins. The mechanisms that cause the different classes transient noise vary and the sources of some categories remain poorly understood. Gravity Spy classified 23

glitch types in the O3 LIGO data set [50]. This serves as a brief introduction to some of the many glitch classes that exist.

Depicted in figure 3.5 are six examples of Gravity Spy classifications. Of these examples, slow and fast scattering glitches have known mechanisms. Imperfections in the LIGO test masses cause light to scatter. This stray light reflects from vibrating surfaces in the detector, causing a change in phase. When the stray light recombines with the main laser beam causing noise [40]. These glitches become more common when there is increased seismic motion present. In order to reduce scattered light noise baffles have been installed, along with the dampening of vibrating surfaces and reaction chain tracking [51]. "Low-frequency lines" usually have frequency below 30 Hz and a duration near one second. They occurred during O3, but have become more common during O4a. The reason for this is currently unknown. "Extremely loud", ""koi fish", and "blip glitches" have been present in the LIGO detectors in various observation runs, but their origins remain unidentified. These glitches are broadband in frequency and short duration, note that extremely loud glitches saturate the spectrogram making the duration appear longer. They often cause problems for transient GW search methods, causing false detections. Further discussion of extremely loud glitches, koi fish, and blip glitches will follow in forthcoming chapters.

3.3.5. LIGO-DV-web

LIGO-DV-web (LDV-web) is a web-based data viewer designed to facilitate swift and effortless access to instrumental data for LIGO researchers [52]. The data viewer utilizes data recorded from both LIGO detector sites. Users can rapidly perform several com-

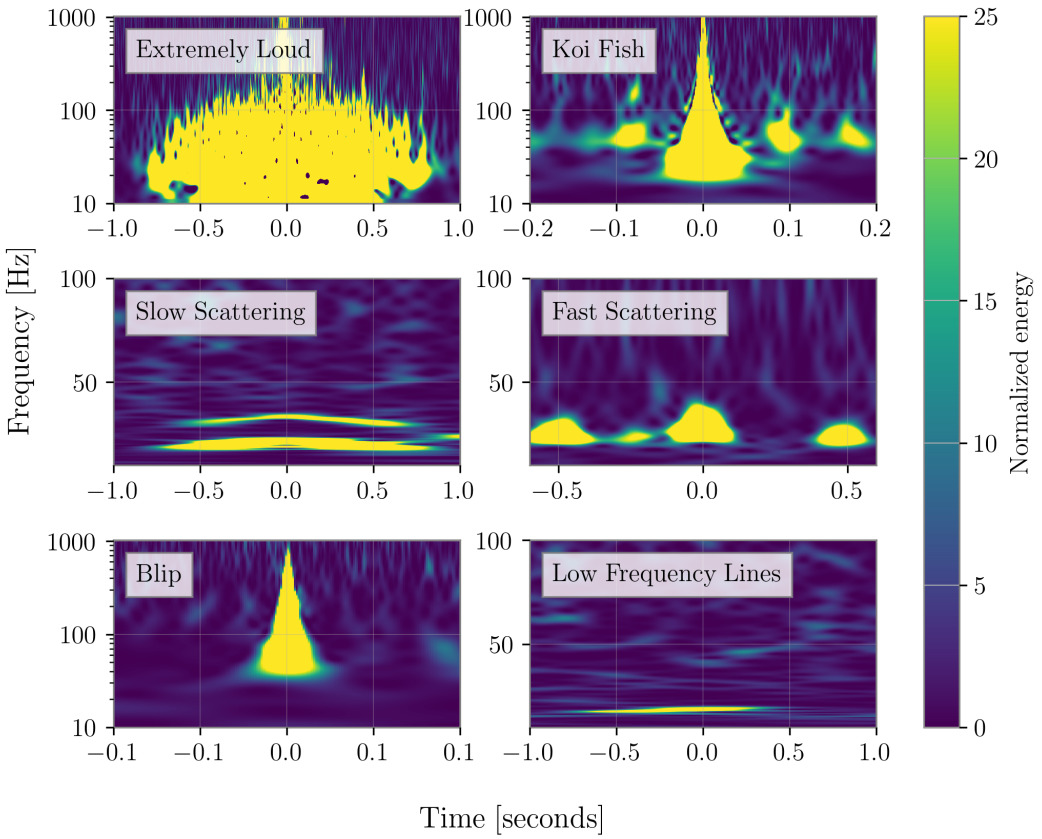

Figure 3.5. Time-frequency spectrograms of common Gravity Spy glitch classes present at both LHO and LLO.

mon analyses for noise investigations, without having to create their own analysis codes. Through the web interface, scientists have the ability to choose data from the instrument channel list and specify times to view and for analysis.

Scientists commonly engage in several essential tasks to analyze the vast amounts of instrument data available. These tasks include, but are not limited to, generating plots of time series, amplitude spectral densities, and Q-transforms, as well as computing the transfer function between channels. Time series plots offer visual representations of LIGO data channel trends over time, aiding in the identification of signal behavior and noise patterns. Amplitude spectral density plots provide insights into the distribution of sig-

nal power across different frequencies, enabling the identification of dominant frequency components within the data that can be used to identify noise sources. Q-transform plots facilitate the analysis of data in the time-frequency domain, while transfer functions represent the frequency response of input and output of a control system. LDV-web incorporates a searchable glitch database, enabling users to find glitches classified by Gravity Spy based on various criteria such as time, SNR, confidence level, and glitch class. By performing these tasks within LDV-web, researchers can quickly gain valuable insights into data characteristics, identify patterns or anomalies, and make informed decisions for further analysis of the detector data.

3.4. Conclusion

In this chapter, I provided an overview of transient noise in the aLIGO instruments. Transient noise adversely impacts the performance of the detectors and the data quality around GW candidate signals. This plays a major role in the tasks the Detector Characterization group are responsible for. These tasks include but are not limited to validating astrophysical candidate signals, ensuring good data quality, and finding noise correlations between the primary GW channel and other detector subsystems. For this reason, the group acts a bridge between LIGO instrument scientists and parameter estimation analysts. From aiding commissioners at LHO and LLO with noise investigations to providing noise mitigation recommendations for parameter estimation groups, detector characterization significantly influences the performance of the detectors and the methods used in GW searches. This chapter also described various software tools maintained and utilized by the group for noise and data analysis. Future chapters will include discussion Detector Char-

acterization projects that employ the tools described in this chapter. As improvements are made to the aLIGO instruments for future observing runs, Detector Characterization will persist in its efforts to understand and mitigate both new and existing sources of transient noise.

Chapter 4. The Statistics of Loud Transient Noise

This chapter focuses on the characterization and analysis of loud transient noise events in the aLIGO detectors, focusing on their SNR, frequency, and amplitude across different observation runs. We generally refer to transient noise with SNR > 100 as loud transients. Some are very loud, with SNR $>$ 1000, and my thesis work focuses around these glitches. The aLIGO instruments undergo continuous commissioning and upgrades to enhance performance and sensitivity, which can influence the occurrence and characteristics of these loud transient noise, often referred to as loud glitches. By examining the variations in loud glitch parameters during the O2, O3, and O4 observation runs at both LHO and LLO, we aim to identify potential sources and understand the impact of loud transients on the detectors.

4.1. Loud Glitch Characteristics

The LIGO instruments constantly undergo commissioning and upgrades during and between observation runs to improve performance and sensitivity. Instrumental changes influence the total number of loud transient noise events observed, see table 4.1 and their characteristics including SNR, frequency and amplitude. Tracking these changes over the course of different observation runs aids in determining potential sources of loud transient noise. In this section, I will discuss various parameters of loud transient noise, commonly referred to as loud glitches, during O2, O3 and O4a in both LHO and LLO.

Table 4.1. Total number omicron triggers with SNR > 1000 in LHO (*top row*) and LLO (*bottom row*) during O2, O3, and O4a.

IFO	O2	O3	O4a
LHO	534	7120	1431
LLO	343	4215	1392

Signal-to-Noise Ratio

An important characteristic of transient noise is the SNR. This is a measure of the loudness of the glitch compared to the overall background noise of the GW channel. The SNR distribution of loud glitches are similar across O2, O3, and O4a in both LHO and LLO as shown in Figure 4.1.

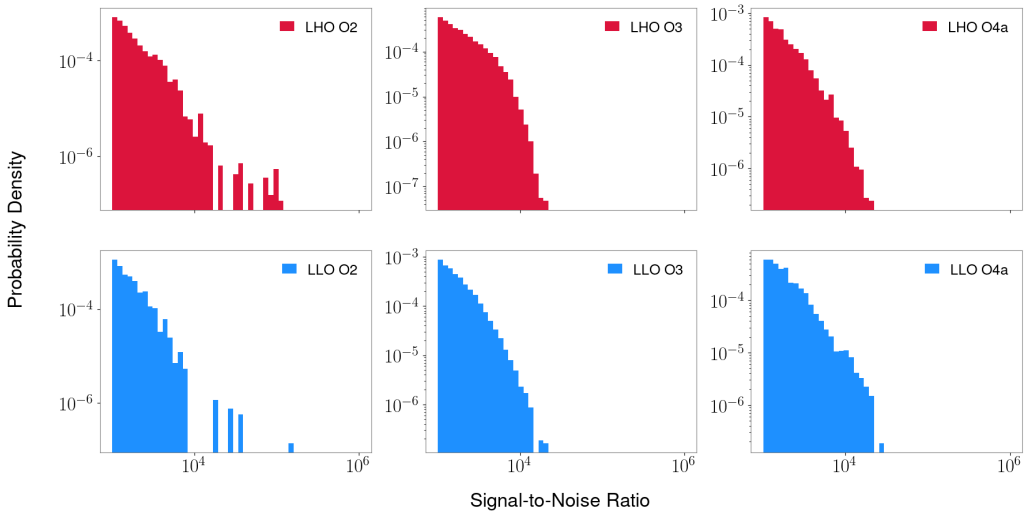

Figure 4.1. The SNR probability density distribution in O2, O3, and O4a. *Top Row*: LHO is shown in red. *Bottom Row:* LLO is shown in blue.

The probability density decreases as the SNR of the glitches increase. In O2, both LHO and LLO have a small secondary population of loud glitches with SNR $> 10^4$. This separate secondary population does not occur in O3 and O4a. Although the aLIGO instruments become more sensitive from observing run to observing run, the overall SNR distribution of the loud glitches does not change drastically. It is also interesting to note that the overall distribution does not shift towards higher SNRs with increased detector sensitivity.

Frequency

The omicron algorithm assigns a peak frequency to triggers. For loud glitches, the assigned peak frequency is between $10 - 1000$ Hz as shown in Figure 4.2.

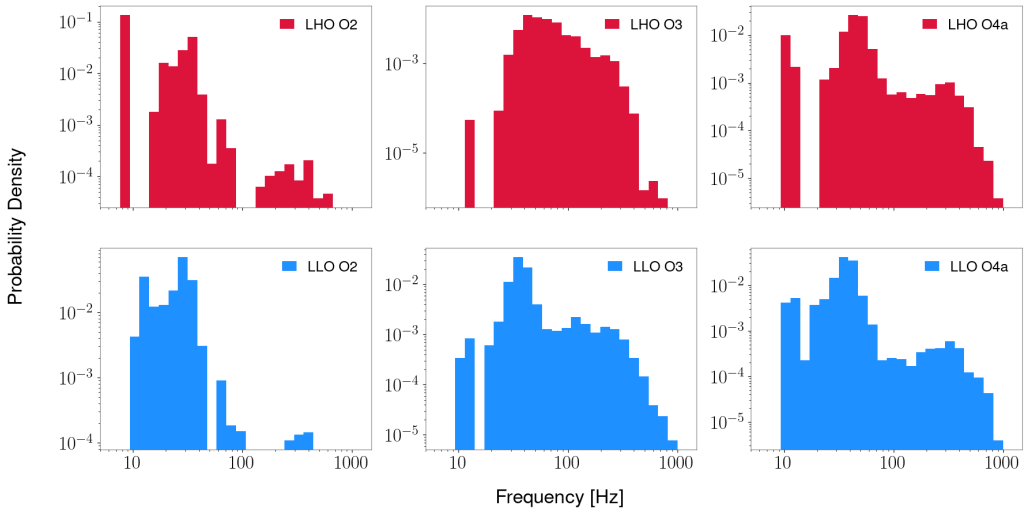

Figure 4.2. The frequency probability density distribution in O2, O3, and O4a. *Top Row*: LHO is shown in red. *Bottom Row:* LLO is shown in blue.

The frequency distribution of loud glitches varies between observation runs. During O2, both detectors have a prominent low-frequency population of loud glitches below 100 Hz. There is also a small population of triggers with frequency above 100 Hz. The probability density of the high-frequency population of glitches increases in both detectors in O3. The LLO frequency distribution exhibits a high-frequency peak ($\sim$ 200 Hz) and low-frequency peak ($\sim$ 30 Hz). However, in LHO the overall distribution is more uniform, peaking at $\sim$ 50 Hz. This changes in O4a, as the low-frequency population of loud triggers becomes more dominant in LHO, thus the distribution is more similar to the LLO O3 distribution. The LLO O4a distribution is comparable to the O3 distribution, although the probability density of the high-frequency population decreases.

We also examine the frequency of loud transients as a function of SNR. The fre-

quency of loud glitches do not exhibit a correlation on the SNR, refer to Figure A.1. Further discussion of the loud glitch SNR-frequency relationship across the various observation runs can be found in Appendix A.

Amplitude

The amplitudes of loud transient noise can be several orders of magnitude larger than that of the GW signals measured by LIGO. For comparison, the largest GW amplitude measured by LIGO was GW150914, with an amplitude of $\sim 10^{-21}$ strain, whereas the loudest glitches have amplitudes $\sim 10^{-16}$ strain, see Figure 4.3. With such large amplitudes, loud glitches briefly dominate the noise background of the primary GW channel.

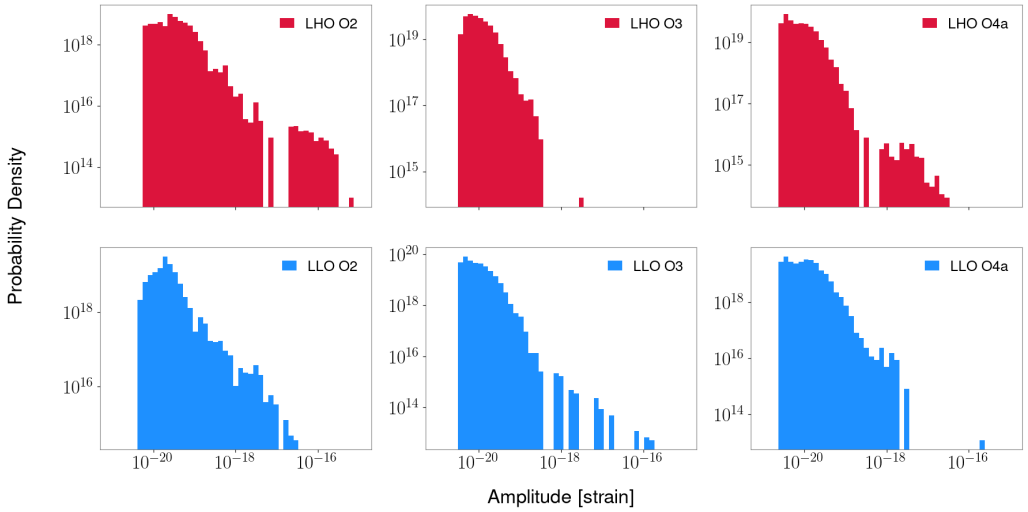

Figure 4.3. The amplitude probability density distribution in O2, O3, and O4a. *Top Row*: LHO is shown in red. *Bottom Row:* LLO is shown in blue.

Across the observation runs, there are some changes in the probability density distribution of loud glitch amplitudes. In O2, the amplitude distribution has two populations in LHO and LLO. The dominant population has amplitudes ranging from $\sim 10^{-20} - 10^{-17}$ strain, while the smaller secondary population has amplitudes greater than $\sim 10^{-17}$. The secondary amplitude population completely vanishes in LHO in O3,

with no loud glitches having amplitude greater than $\sim 10^{-17}$. For LLO the secondary population remains, though it is not as pronounced as it was in O2. During O4a, the secondary amplitude population reappears in LHO, but the amplitudes are greater than $\sim 10^{-18}$ strain and do not exceed 10^{-16}. In LLO, the higher amplitude distribution of loud glitches merges with the lower amplitude glitches, with all but one loud glitch having an amplitude less than $\sim 10^{-17}$. Similarly to the SNR of loud glitches, the amplitudes do not trend toward larger values with increased detector sensitivity.

We also analyze the amplitude of loud transients in relation to SNR. There is a clear linear relationship between the amplitude and SNR as expected, with amplitude increasing as the glitch SNR increases, shown in Figure A.2. Additional details on the amplitude-SNR relationship of loud glitches between observation runs are provided in Appendix A.

4.2. Impact of Loud Transient Noise on LIGO Detectors

Loud glitches create significant challenges for both LIGO instrument scientists. These transients are very loud (SNR > 100) and very short (fractions of seconds) in nature, leading overflows in digital-to-analog and analog-to-digital converters. Specifically, loud glitches saturate the coils responsible for mirror actuation, sometimes resulting in detector lock losses. Losing lock due to loud glitches reduces the detector duty cycle, or uptime, and multi-detector observing time which is crucial for accurate sky localization of GW candidate signals. Furthermore, loud glitches have a substantially impact the BNS range, causing "range drops". An example of a range drop is shown in Figure 4.4.

At the time of loud glitches, the BNS range distribution peaks at ~ 30 Mpc in both

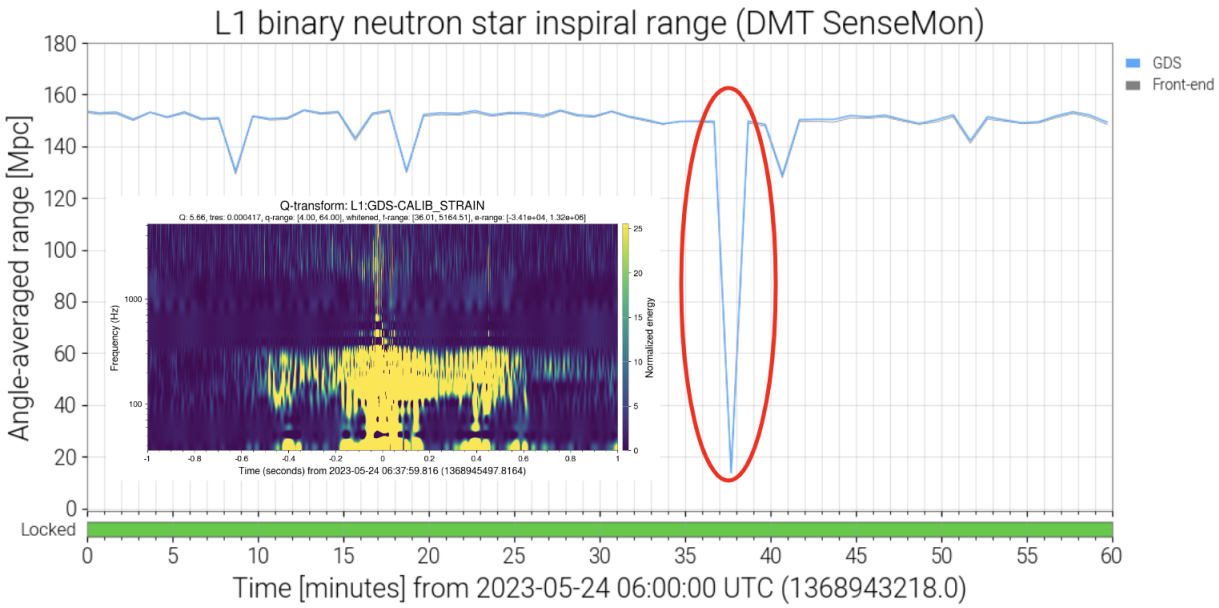

Figure 4.4. Detector Characterization Summary Page plot of a BNS range drop (red circle) caused by a loud transient with an SNR of 2860 in LLO on May 24, 2023. The omega scan of the glitch from LIGO-DV-web is overlaid on the BNS range plot.

LHO and LLO for triggers with SNR > 500, see Figure 4.5. Glitches that cause the range to drop to 0 Mpc are associated with instrumental lock losses. Following the occurrence of a loud glitch, the BNS range distribution aligns more closely with the average BNS range observed during O3 in both detectors [36]. There is no significant correlation between the SNR, frequency, and amplitude of the glitch and the decrease in BNS range at the time of the glitch occurrence, refer to Appendix A. Loud glitches have a substantial impact on the performance of the LIGO detectors and it is imperative to characterize them and investigate potential sources.

4.3. Loud Transient Noise Rates

Transient noise rates may reveal patterns and periods of time that may be of interest to investigate. Glitch rates are important in discerning whether loud transients are instrumental or environmental in nature by correlating them to seasonality. O3 monthly

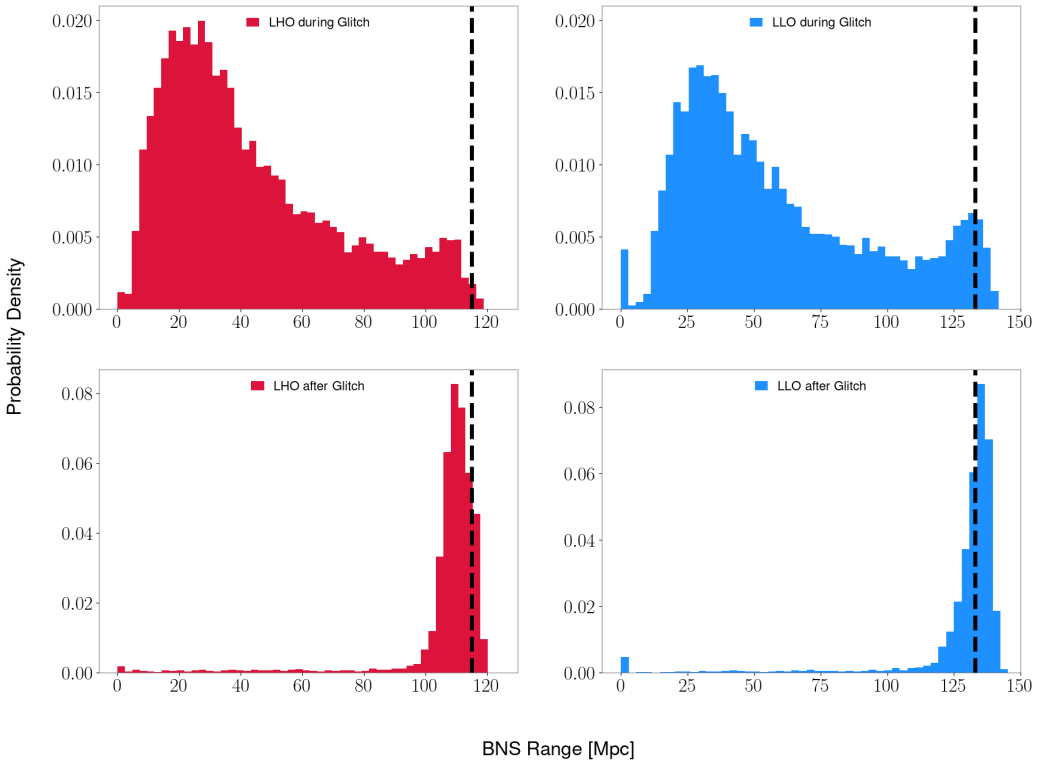

Figure 4.5. BNS range distribution in the O3 during (*top panels*) and after (*bottom panels*) loud glitches at LHO (red) and LLO (blue). *Left Panels*: The black dashed line represents the median range at LHO of 111 Mpc during O3. *Right Panels*: The black dashed line represents the median range at LLO of 134 Mpc during O3.

hourly glitch rates for loud transients identified by Gravity Spy with confidence > 0.9 and SNR > 8 do not indicate a pattern or correlation to the time of year [53]. Examining the hourly rate per day for each observation run, refer to Figure 4.6, reveals in more detail periods with higher rates of loud glitches.

Comparing the average hourly glitch rate between observation runs highlights the need to investigate the different subsystems of the LIGO instruments that have changed, with the aim of finding correlations to loud glitches. There are notable variations in the average rate per hour of loud triggers across observation runs, as shown in tables 4.2 and 4.3 for LHO and LLO respectively.

O3 had the highest rate of loud triggers, followed by O4a, and then O2. The lower

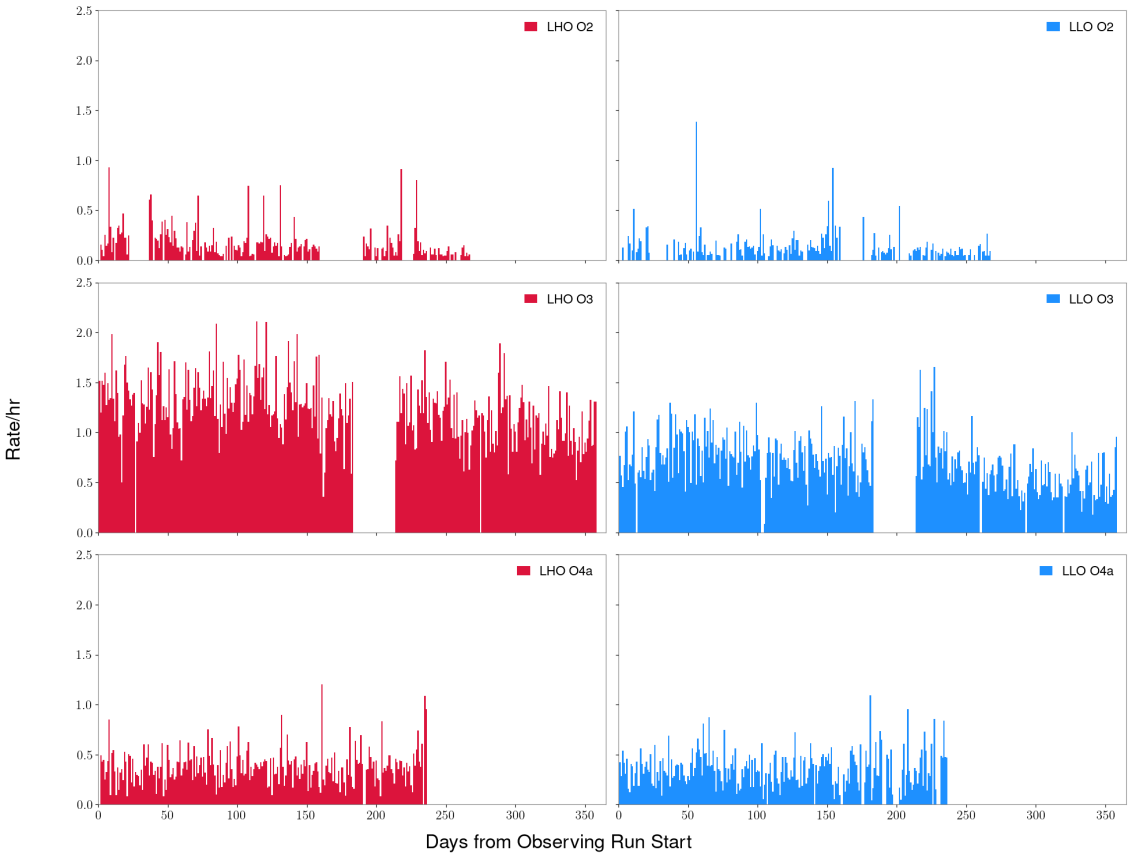

Figure 4.6. LHO (red) and LLO (blue) daily rate per hour of omicron triggers with SNR > 1000 for different observation runs. *Top Panels*: O2 began on November 30, 2016 and ended on August 25, 2017. *Middle Panels*: O3 began on April 1, 2019 and ended March 28, 2020. Note, there was a commissioning break from October 1 to November 1, 2019. *Bottom Panels*: O4a began on May 24, 2023 and ended on January 17, 2024.

Table 4.2. LHO average rate per hour of omicron triggers with SNR $> 10^3$ (*top row*) and $> 10^4$ (*bottom row*) for O2, O3a, O3b and O4a.

LHO	O2	O3a	O3b	O4a
SNR $> 10^3$	0.14	1.31	1.08	0.37
SNR $> 10^4$	0.007	0.01	0.01	0.005

Table 4.3. LLO average rate per hour of omicron triggers with SNR $> 10^3$ (*top row*) and $> 10^4$ (*bottom row*) for O2, O3a, O3b and O4a.

LLO	O2	O3a	O3b	O4a
SNR $> 10^3$	0.09	0.78	0.58	0.35
SNR $> 10^4$	0.001	0.015	0.09	0.018

rate of triggers in O4a compared to first half of the third observing run (O3a), despite occurring around the same time of year, suggests that seasonality does not impact glitch rate. The largest difference in glitch rates between detectors is in O3, with the rate at LHO being nearly twice the rate at LLO. Despite this difference, the similarity in the rate of loud triggers between both detectors from run to run supports that loud glitches are instrumental in origin. Since we hypothesize that loud transient noise is instrumental in nature, examining the time interval between each occurrence of a loud glitch (Figure 4.7) may provide insight into the process that may cause them. The time interval between glitches reveals that there are few loud triggers that occur in clusters ($\delta t < 1$ min). This suggests that the majority of loud glitches occur independently from each other.

To further support this idea, we examine the daily loud glitch rate probability density distribution in LHO and LLO in Figure 4.8. We fit the probability density distribution with a Poisson probability distribution given by,

$$P(k) = \frac{\mu^k e^{-\mu}}{k!}, \tag{4.1}$$

where μ is the mean number of loud triggers for each observation run in the respective detector and k is the number of occurrences. The Poisson distribution represents the probability of a certain number of events occurring within a fixed time period, given a known mean rate, with each event happening independently of the others.

The distribution of the daily rate of loud glitches at LHO and LLO closely approximates a Poisson distribution for O2, O3, and O4a. The fit is more accurate for LHO compared to LLO. This provides additional evidence that loud glitches occur independently of one another.

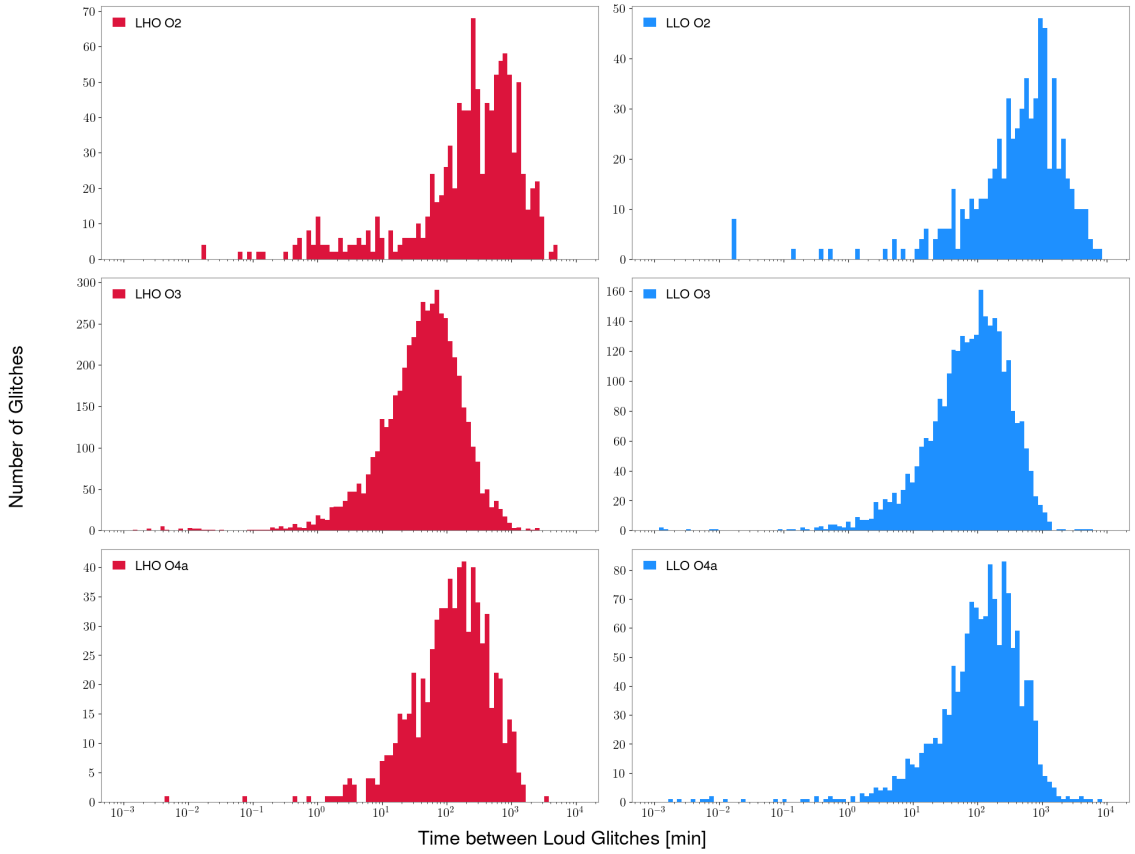

Figure 4.7. The distribution of the number of loud triggers as a function of the time interval between glitches during O2, O3 and O4a. *Left Panels*: LHO shown in red. *Right Panels*: LLO shown in blue.

4.4. Conclusion

In summary, loud transient noise poses significant challenges for the performance and data quality of the LIGO detectors. Characterizing these glitches, including their SNR, frequency, and amplitude, is crucial for investigating their origins. Key takeaways from this analysis include the notable variation in the glitch rate across observation runs, with O3 exhibiting the highest rate of loud transient noise events. These glitches occur independently of one another, as evidenced by their distribution patterns. Additionally, loud transient noise have a significant impact on the instruments, causing considerable range drops. Interestingly, despite the improvements in the sensitivity of the instruments over

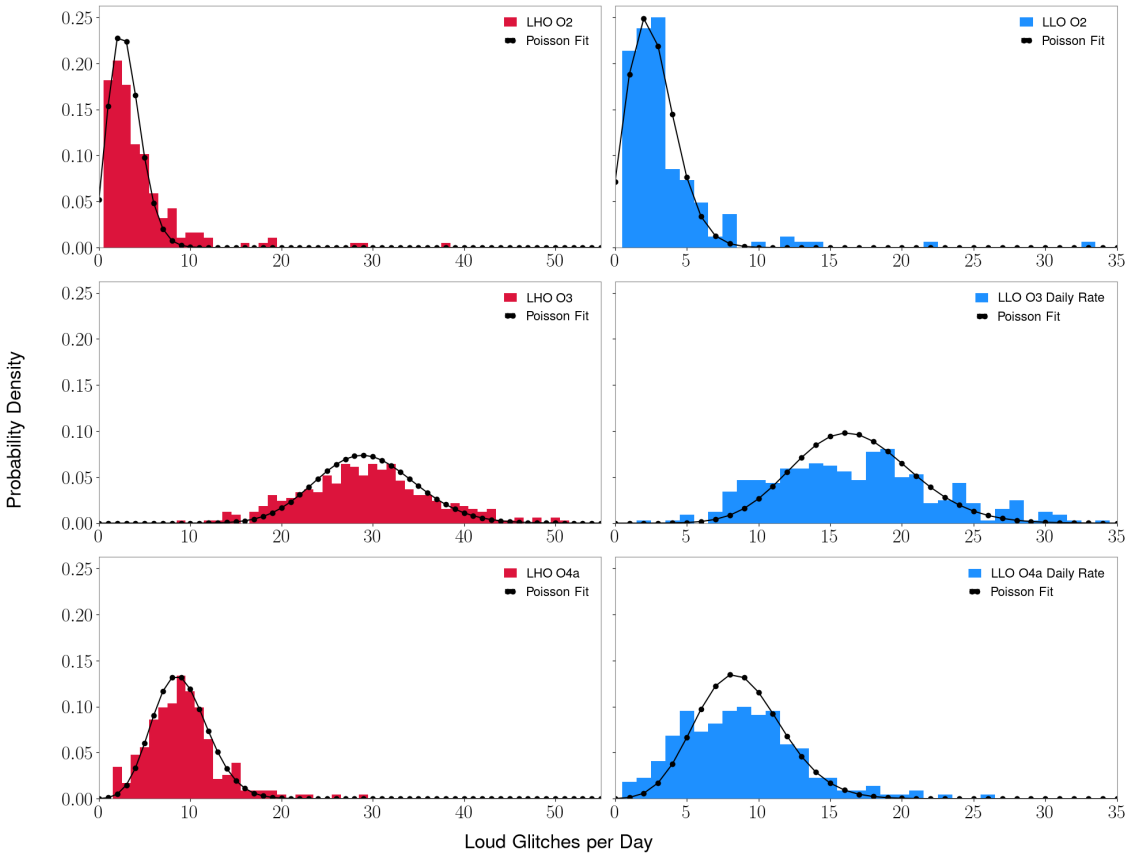

Figure 4.8. Probability density of daily rate of loud glitches in LHO (red) and LLO (blue) during O2, O3, and O4a. The black curve is the Poisson distribution fit for the respective observation run.

time, the SNR and amplitude of loud glitches do not necessarily increase. This indicates that enhanced sensitivity does not always correlate with increased loudness or larger amplitude with these glitches. The characteristics of loud transient noise glitches discussed in this chapter, motivate the investigations in the following chapters.

Chapter 5. Auxiliary Witnesses of Loud Transients

Auxiliary channels in LIGO play a critical role in monitoring environmental and instrumental noise, allowing for the identification noise sources that could interfere with the detection of GWs. [40]. In this chapter, I discuss several analyses of auxiliary channels that witness loud transient noise during O3. The primary goal is to identify and understand the auxiliary channels that are sensitive to loud glitches, which are unsafe to use in GW signal analyses. Some of these investigations make use of H-veto [49] (section 3.3), to determine various auxiliary channels that are associated with loud transient noise in the GW strain data. This also includes an analysis of Koi Fish glitches, which is a Gravity Spy [38] class which also contains loud transient noise. The findings reveal numerous auxiliary channels which witness loud transient noise and the extent in which these glitches are observed in the aLIGO instruments. Unfortunately, this study only identified witnesses of loud transient noise and not their cause.

5.1. Electrostatic Drive Voltage Monitors

The ESD on ETMX and ETMY, have 18 V and 24 V voltage sources which are used when locking the detector (24 V) and in the low noise mode (18 V). There are physical environmental auxiliary channels which monitor these voltage sources, known as voltage monitor channels. Transient noise should not appear in these channels, however many glitches occur in the voltage monitor channels. Many of these glitches are coincident with the primary GW channel.

During O3 in LLO, particularly in February 2020, the 18 V ETMY ESD voltage monitor channel was found to be a round winner by H-veto on several occasions. The

ETMY ESD was used for actuation in the DARM feedback control loop from February 1 - 25, 2020 [54]. The vetoed triggers in the GW channel were primarily loud glitches. If

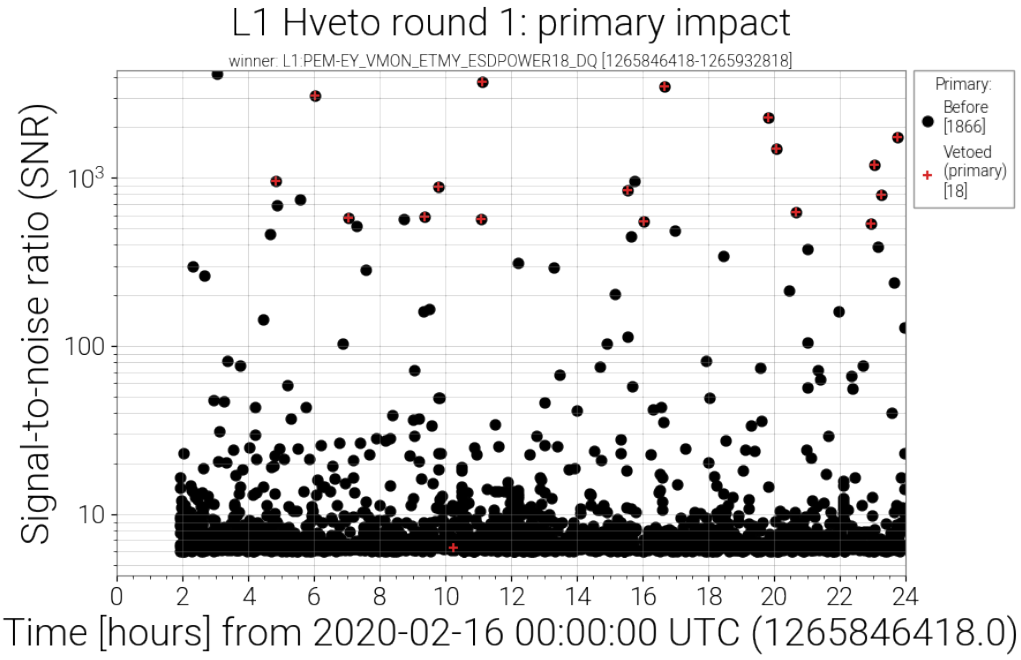

Figure 5.1. H-veto SNR versus Time plot for February 16, 2020. On this day the round one winner channel was `L1:PEM-EY_VMON_ETMY_ESDPOWER18_DQ`, the 18 V ETMY ESD voltage monitor channel. The black points are triggers in the GW channel. Black points with red crosses are triggers that were vetoed using the ETMY ESD voltage monitor triggers. Of the 18 vetoed triggers for this day, 17 are loud glitches with SNR > 400.

the glitches in the monitor are the cause of triggers in the GW readout signal, then vetoing this noise is good. However, if noise in the voltage monitor channel are a consequence of glitches in the GW channel then this monitor channel is unsafe to use when validating GW candidate events.

I investigated the triggers in both the ETMX and ETMY voltage monitor channel that were coincident with the GW omicron triggers. Coincident triggers are defined to occur within ± 0.1s of each other. For the loud glitches in the GW channel, SNR > 200, $\sim 39\%$ of the triggers were coincident with the voltage monitor.

I also compared ETMX and ETMY ESD voltage monitor channel triggers with the GW channel for March 2020. At the beginning of the month the detector was locked using the ETMY ESD to actuate on the mirrors, then after March 10^{th}, the ETMX ESD was used for actuation during locking [54]. Loud transient noise in the GW channel was coincident with triggers in the voltage monitor for the ESD used for locking the instrument [55], shown in figure 5.2. The voltage monitor channels also contained louder glitches, that were not coincident with glitches in the GW strain, thus I suspected these channels were witnesses and not a cause of loud transient noise.

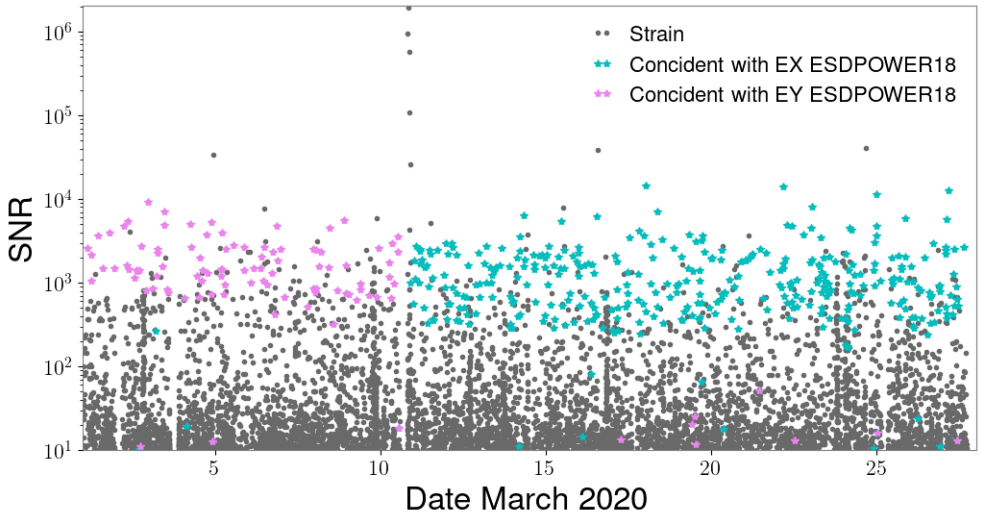

Figure 5.2. GW strain omicron triggers from March 1–28 2020 represented by gray points. Triggers that are coincident with the ETMX voltage monitor represented by cyan points and ETMY voltage monitor by violet points.

Although the coincident glitches are very loud in the GW channel, in the voltage monitor channel these triggers mostly have SNR below 100 (see figure 5.3). The triggers that normally appear in the voltage monitors also have their own structure. In the ETMX ESD monitor, the glitches appear at SNR below 20, SNR near 30 and SNR near 60. At each SNR level, there is a visible oscillation in the SNRs of the triggers. In the ETMY

ESD monitor, the triggers have SNR below 15, a band of triggers SNR near 20 which shifts up to SNR around 50 after March 15, 2020. There are also triggers that appear between these two groups in the monitor. The glitches that typically occur in each voltage monitor are not coincident with each other beyond what would be expected from statistical coincidences. In both cases, the glitches that are coincident with loud glitches in strain do not have a pattern in the either ESD voltage monitor.

Figure 5.3. *Top*: ETMX voltage monitor triggers from March 1–28 2020 represented by cyan points. Triggers that are coincident with GW strain represented in gray. *Bottom*: ETMY voltage monitor triggers from March 1–28 2020 represented by violet points. Triggers that are coincident with GW strain represented in gray.

Locking the detector with the different ESDs did not cause any obvious change in the glitch rates. We concluded from these observations that for some reason (possibly electronic interference) the glitches in the voltage monitor channels are produced by the large

electronic drives due to the loud glitches in the primary GW channel. Thus, the voltage monitors are not a source of loud transient noise the in GW data and they are unsafe to use in GW candidate signal analyses [40].

5.2. Antisymmetric Port Wavefront Sensors

In LLO, the beginning of the second half of the third observing run (O3b) had a higher daily rate of loud transient noise compared to the rest of O3b (section 4.3). In November, the rate of loud glitches with SNR $>$ 1000 was 0.87 per hour where as the rate was 0.58 per hour for all of O3b. For this reason, I did a weekly H-veto analysis for November 2019 to determine auxiliary witness channels and investigate the glitches in those channels.

The November 2019 H-Veto runs were done in seven day segments: Week 1 - Nov 1-8, Week 2 - Nov 8-15, Week 3 - November 15-22, and Week 4 - November 22-29. For statistical purposes the SNR threshold used was reduced to triggers with SNR $>$ 100. Figure 5.4 shows a comparison histogram between the number of triggers before and after three rounds of analysis for the first week of November.

The H-veto round one winner for all four of the weeks analyzed was `L1:ASC-AS_B_RF45_I_YAW_DQ`. This channel is for one of the two ASC wavefront sensors located at the antisymmetric port. It senses the I component of the demodulated radio frequency 45 MHz sideband. H-veto identified five auxiliary channels for week 2, three in week 3, and four in week 4. The vetoed triggers primarily had SNR $>$ 500 and were associated with the round one winner. Week 2 also had two clusters of triggers vetoed with SNR between 100 and 200 and frequency range $10 - 25$ Hz (Figure 5.5). Many of the triggers in

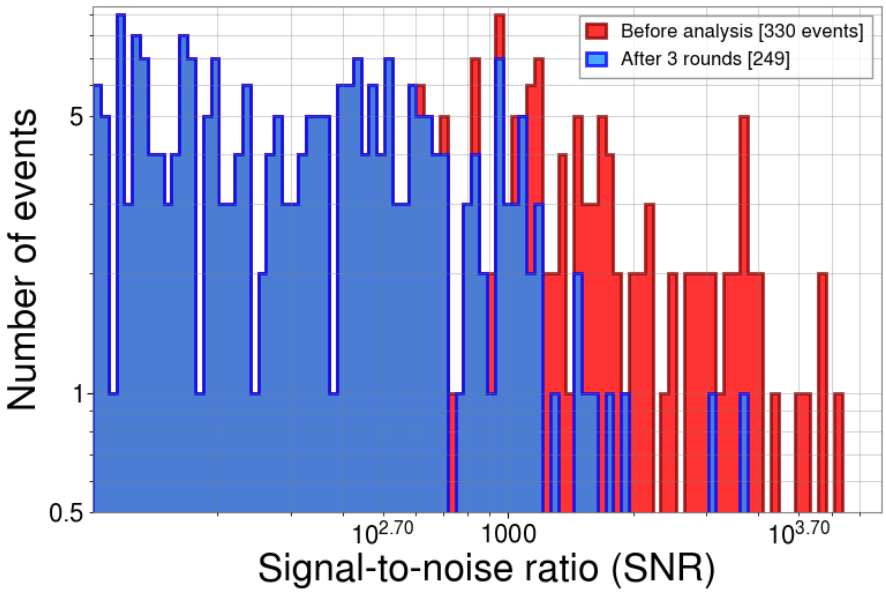

Figure 5.4. Results from Week 1. Histogram of number of triggers in the GW channel before the H-veto analysis (red) compared with the number of triggers after all vetoes from each round is applied (blue) versus the SNR of the triggers.

those clusters were also associated with the round one winner channel

To gain insight on how often this antisymmetric port sensor witnessed loud transient noise, I checked for coincident triggers with strain triggers ($\pm$0.1s) for the entirety of O3, Figure 5.6. For the loud triggers in strain, $\sim$ 65% them are coincident with `L1:ASC-AS_B_RF45_I_YAW_DQ`. A majority of glitches in `L1:ASC-AS_B_RF45_I_YAW_DQ` are lower SNR, below 100. The glitches that are not coincident with strain appear in stratified clusters over the course of O3, while the coincident glitches do not take a particular form (bottom panel Figure 5.6).

Signals from this sensor are not used in any ASC feedback loops, but Q component from the other wavefront sensor at the antisymmetric port (`L1:ASC-AS_A_RF45_Q`) is used to control the DHARD control loop. Although H-veto did not identify this sensor as

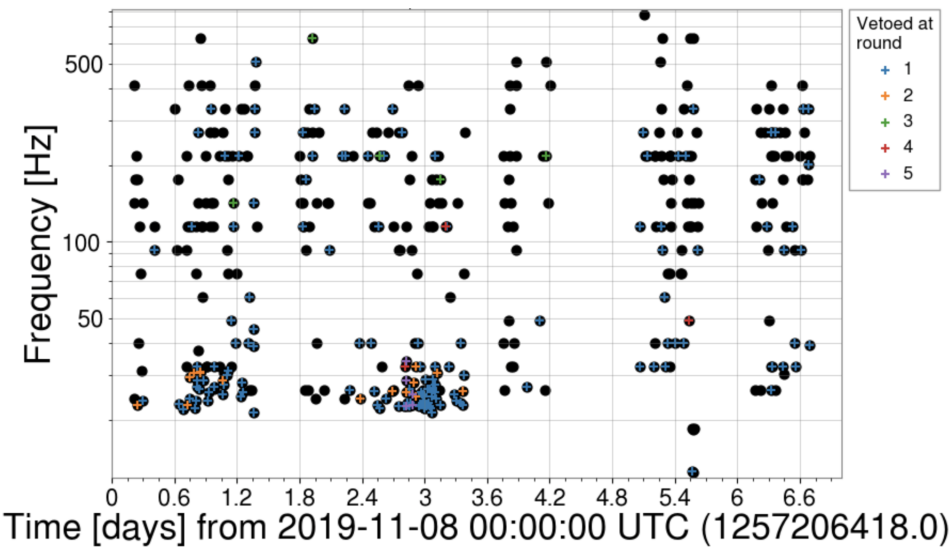

Figure 5.5. Frequency versus Time plot from Week 2 H-veto analysis. The black points are the triggers and the color crosses represent the round in which the trigger was vetoed. Round one represented by blue crosses, two by orange, three by green, four by red and, five by purple. Between 0.6 and 1.2 days and around 3 days after November 8, 2019 clusters of low frequency vetoed triggers in the GW channel appear.

a round winner, loud glitches are visible in the time series with a smaller amplitude compared to `L1:ASC-AS_B_RF45_I`, see Figure 5.7. The amplitude difference between the two antisymmetric port wavefront sensors was due to the `L1:ASC-AS_B` sensor receiving more light than `L1:ASC-AS_A` sensor as the optic responsible for splitting the light between the two was not at 45°. Also visible in the time series of the wavefront sensor channels, is an oscillation after t = 0. This is due to the glitch being suppressed by the interferometer sensing and control feedback loops.

5.3. Other Auxiliary Witness Channels

Due to the nature of loud glitches, numerous auxiliary channels witness them, although they are not the source of the loud transient noise. These channels are not confined to one location of the aLIGO instrument. Auxiliary channels that are used to monitor power and transmitted light are sensitive to loud transient noise. At end of each of the

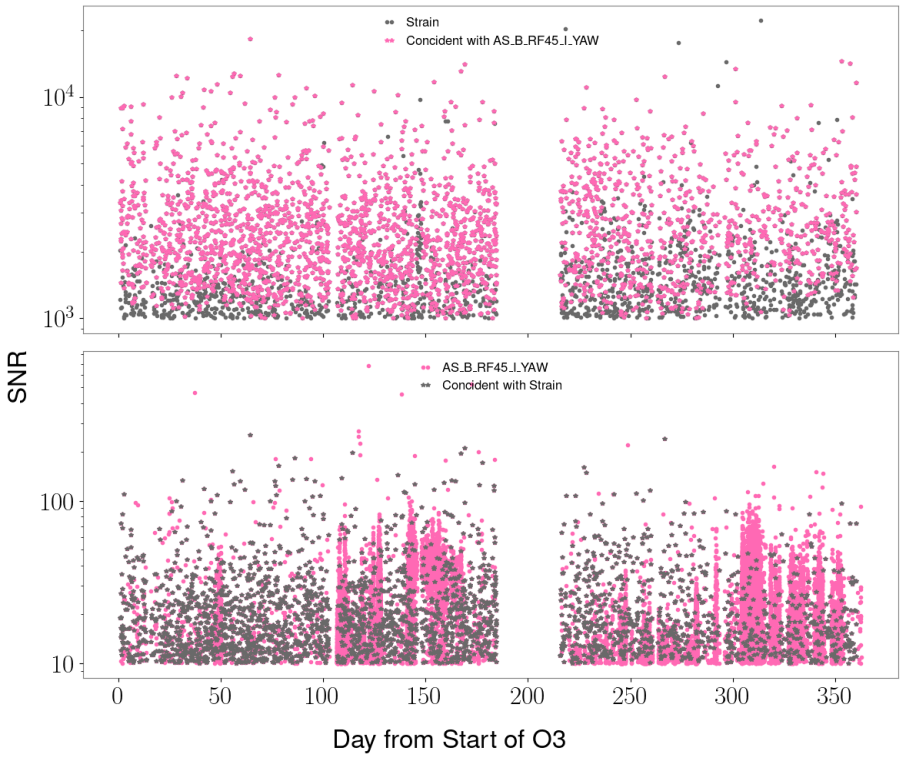

Figure 5.6. *Top*: O3 GW strain omicron triggers are shown in gray and triggers that are coincident with `L1:ASC-AS_B_RF45_I_YAW_DQ` are shown in pink. These coincident triggers are $\sim 65\%$ of the total amount of triggers in the GW strain data. *Bottom*: O3 `L1:ASC-AS_B_RF45_I_YAW_DQ` are shown in pink and triggers that are coincident with strain are in gray.

arm cavities, there are photodiodes used to monitor the transmitted light. These sensors witness loud glitches due to changes in the arm cavities length. The sensor that monitors the power in the Power Recycling Cavity witnesses loud glitches, example shown in Figure 5.8 due to changes in the length of the PRC. Auxiliary channels that monitor the reflected light from cavities are also subject to the effects of loud glitches. In the time series of these channels, small changes appear at the time of loud glitches as they temporarily affect the resonance condition of the cavities. Many of these channels appear in the summary page H-veto runs during observation runs, and in my H-veto analysis for November 2019.

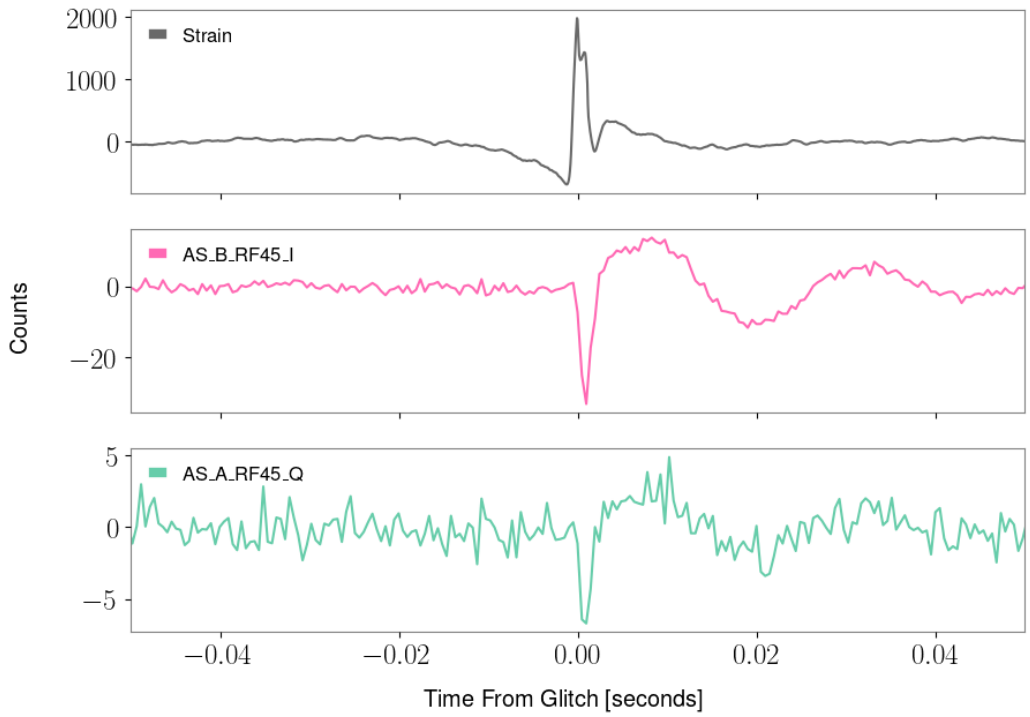

Figure 5.7. *Top*: Time series of a loud transient with in the GW data at t = 0 *s*. *Middle*: The same glitch seen in `L1:ASC-AS_B_RF45_I_YAW_DQ` *Bottom*: The same glitch seen in `L1:ASC-AS_A_RF45_Q_YAW_DQ`.

During each round of H-veto analysis, the significance is recalculated for the channels after the round winner triggers are vetoed. Channels that are correlated with round winner channels will have a decrease in their significance. This is the case with many of the ASC and LSC auxiliary channels used for sensing the various interferometer degrees of freedom. Since the noise appears in the sensing signals, it also affects the signals of the control loops making them witnesses as well. An example of this is shown in the H-veto drop down plot in Figure 5.9, the significance of one of the DHARD control loop channels decreases after the round one sensor channel triggers are vetoed. A full list of the channels found to be statistically significant by H-veto and channels associated with these channels is provided in Appendix B.

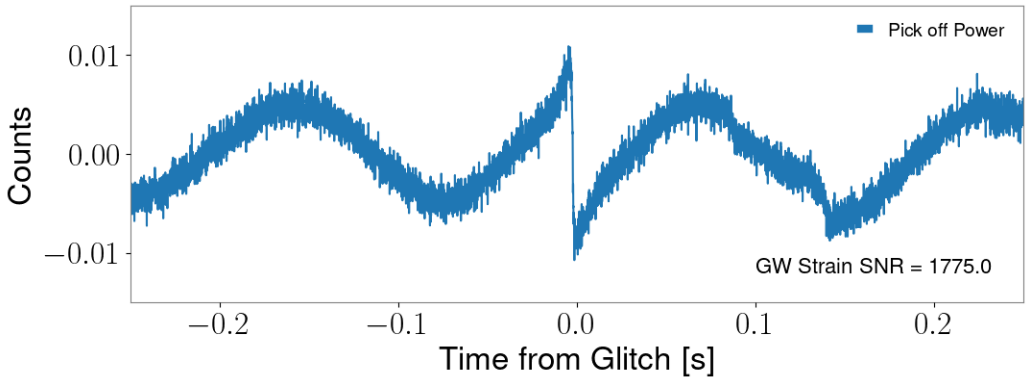

Figure 5.8. An example of the time series of a loud glitch (t = 0) seen by the photodiode that monitors the pick off power from the PRC. The time series is high passed to better show the glitch in this auxiliary channel.

5.4. Hierarchal Veto Applied to Koi Fish Gravity Spy Class

Based on the H-veto analysis in Section 5.2, I mentored and assisted with a summer student project that focused on using H-veto to analyze auxiliary channels associated with transient noise in LLO classified as Koi Fish glitches by Gravity Spy (see Figure 3.5) [56]. The Koi Fish glitches used in the analysis were in O3b and had confidence level greater than 0.9 (2960 glitches in total). Koi Fish glitches are class identified by Gravity Spy that includes triggers with an SNR > 100. Of these Koi Fish glitches, $\sim 61\%$ of them surpassed the threshold to be considered loud transient noise. The SNR distribution of Koi Fish glitches are shown in Figure 5.10.

The initial H-veto run on Koi Fish glitches used the standard configuration file, without excluding any auxiliary channels. This run identified the round winner channel as one of the transmitted light sensors at the end of the X arm cavity, which also detected loud glitches with SNR $>$ 1000. This channel is a known witness to transient noise and was thus removed for the subsequent analysis, along with other transmitted light channels. With these channels excluded, the LSC reflected light auxiliary channel was iden-

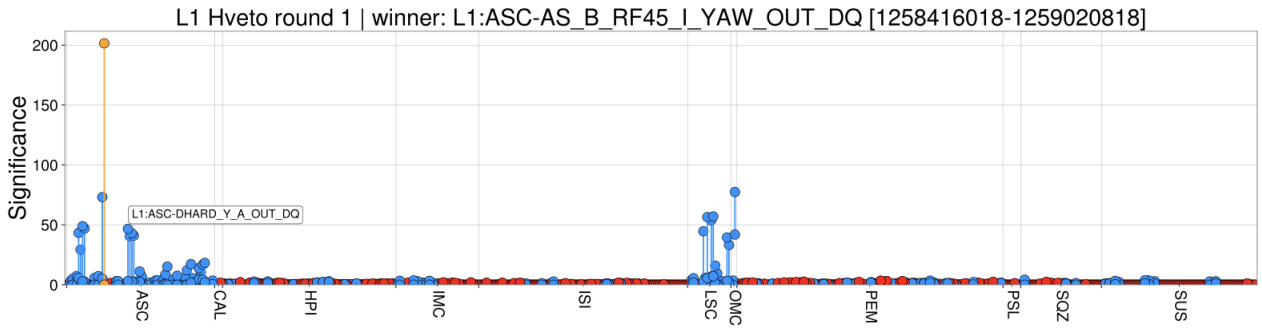

Figure 5.9. H-veto significance drop down plot for Week 1 of November 2019. The round winner, `L1:ASC-AS_B_RF45_I_YAW_DQ`, is shown in yellow. The top of the yellow baton is the significance of the round winner before this round and the bottom of the baton is its significance in the next round, after its triggers have been vetoed. The blue batons are for channels whose significance dropped after this round (indicating that that channel had some trigger times in common with the winner). Red batons are for channels whose significance increased in the next round.

tified by H-veto as the new round winner, which is also a witness to transient noise. For the following analysis, the ASC and LSC transmitted and reflected light channels were removed from the configuration file. After excluding these auxiliary channels, H-veto identified channels associated with the Internal Seismic Isolation (ISI) system as round winners. The triggers vetoed in the GW strain channel from the ISI triggers were of low SNR (Figure 5.11), and the ISI system is not expected to show correlation to the GW strain.

5.5. Conclusion

In summary, I investigated further all the channels that were found to be statistically significant by H-veto during O3. I identified several auxiliary channels that are sensitive to loud glitches that are unsafe for use in GW signal analyses. The ESD voltage monitor channels were identified as significant witnesses to loud transient noise. However, these channels were determined not to be the source of the glitches, making them unsafe for validating GW candidate events. The analysis of the Antisymmetric Port Wavefront

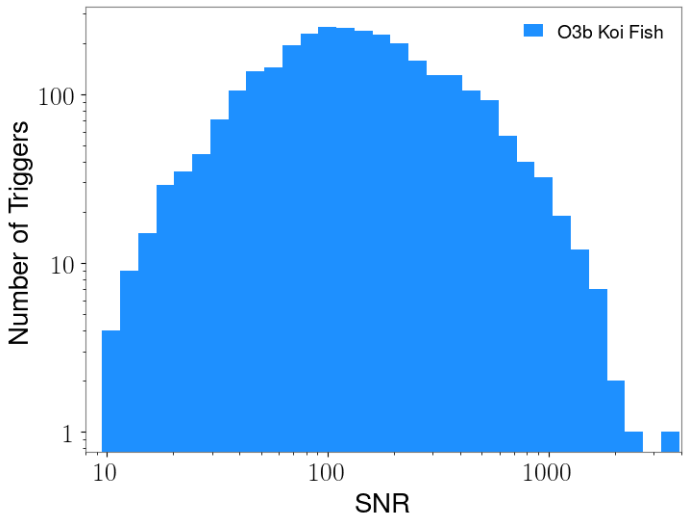

Figure 5.10. SNR distribution of LLO Koi Fish glitches in O3b.

Sensors during November 2019, a period with a higher daily rate of loud glitches, identified the channel `L1:ASC-AS_B_RF45_I_YAW_DQ` as a significant witness to transient noise. Despite the coincidence with loud glitches, these sensors are not part of any active control loops, making them a witness to this noise. Additionally, numerous auxiliary channels monitoring power and transmitted light were found to be sensitive to loud transient noise, often witnessing glitches due to changes in cavity lengths. An H-veto analysis of Koi Fish glitches, a class identified by Gravity Spy, initially highlighted transmitted light sensors and reflected light channels as round winners, which are known witnesses to loud transient noise. The H-veto analysis of Koi Fish glitches revealed that many of the same auxiliary channels witness both Koi Fish and Extremely Loud transient noise, suggesting that these types of noise may share similar origins. Upon excluding these channels, H-veto identified channels associated with the ISI system as round winners. However, the ISI triggers were low in SNR and not expected to correlate with the GW strain or be the source of loud transient noise. Although noise in many auxiliary channels coincides with loud glitches,

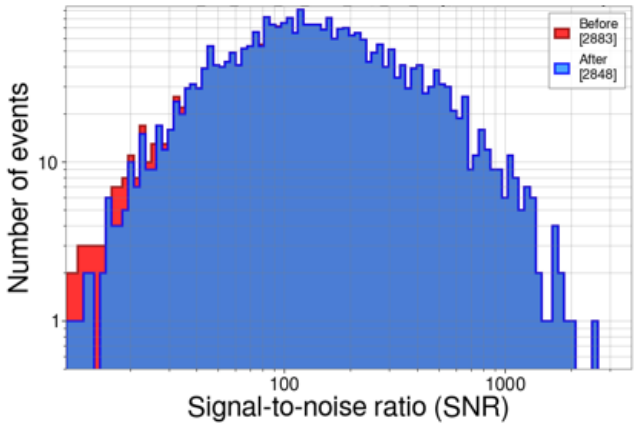

Figure 5.11. Results from H-Veto analysis where an ISI system auxiliary channel is a round winner. The SNR distribution of before the analysis is shown in red. The SNR distribution after the vetoes are applied is shown in blue.

I did not find evidence that these channels are the source of loud transient noise in the

aLIGO detectors.

Chapter 6. Morphology of Loud Transients

Investigating and understanding the morphology of transient noise can provide valuable insights into their sources and guide efforts to mitigate them from LIGO data. By analyzing the structure and patterns of these noise artifacts, researchers can identify their origins and develop strategies to reduce their impact, ultimately enhancing data quality. Omega-scans [47] (section 3.3) are useful for comparing the time-frequency morphology of loud transient noise to other glitch types classified by Gravity Spy, but they do not necessarily provide enough information about potential sources. In the case of loud transient noise, omega-scans are often saturated, making the glitch duration appear longer than it is. Analyzing the time series of loud transient noise provides more accurate information about the duration of the glitch.

t-Distributed Stochastic Neighbor Embedding (t-SNE) is a powerful and widely-used machine learning algorithm for dimensionality reduction, particularly effective for visualizing high-dimensional datasets. It is designed to convert the similarities between data points into probabilities and then find a way to represent these points in a low-dimensional space while keeping these probabilities as close as possible to those in the original high-dimensional space. This results in a mapping of multi-dimensional data to two or three dimensions while preserving the relative distances between points, making it an excellent tool for uncovering patterns and clusters within complex datasets [57]. In this chapter, I will discuss analyses that employ t-SNE to cluster data from Gravity Spy glitch classifications and time series of loud transient noise in aLIGO.

6.1. Gravity Spy Classification Clustering

Gravity Spy classifications are vital in distinguishing the various types of transient noise in the aLIGO instruments. Despite the diversity of glitch classes, some may share similar characteristics in the time-frequency domain. For instance, glitches with similar frequency bandwidths or similar temporal patterns can be easily confused. For this reason, I analyzed Gravity Spy identified triggers with t-SNE to gauge similarities between classes that exhibit similar features to loud transient noise triggers.

This analysis uses LLO glitches identified by Gravity Spy in O4a as Extremely Loud, Koi Fish, Blip, Fast Scatter, Slow Scatter and Low Frequency Lines with confidence level greater than 0.9. Koi Fish and Blip glitches are both broadband in frequency and have short durations similar to Extremely Loud glitches. Slow Scatter, Fast Scatter and Low Frequency Lines do not share similar characteristics with Extremely Loud glitches, see Figure 3.5. The use of these glitch classes in this analysis is to show the ability of t-SNE to distinguish between the Gravity Spy glitch classifications that do not have similar morphologies.

The t-SNE algorithm reduces the data from the Omicron algorithm [45] (section 3.3) used by Gravity Spy to two dimensions, assigning each glitch and X and Y coordinate. The closer the points are to each other, the greater their similarity. Figure 6.3 shows the results from applying t-SNE to the Gravity Spy Glitch classifications. Extremely Loud, Koi Fish and Blip glitches occupy a separate parameter space than Fast Scatter Slow Scatter and Low Frequency Lines. Due to the morphology similarities between Extremely Loud, Koi Fish and Blip glitches, t-SNE does not separate these classifications

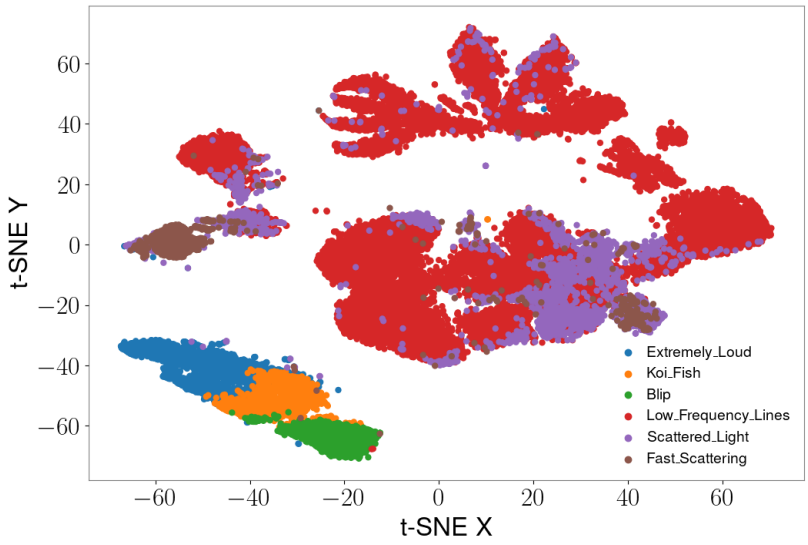

Figure 6.1. t-SNE clustering results for different Gravity Spy glitch classifications of O4a LLO transient noise. Each Gravity Spy classification is represented by a different color.

into their own individual "islands". When analyzing the space these glitch classes occupy, Extremely loud glitches are farthest left, followed by Koi Fish glitches and Blips are farthest to the right. The omega-scans of Blip glitches are the least saturated by noise, followed by Koi Fish glitches, then Extremely Loud (Figure 3.5). The omicron parameters SNR and amplitude, shown in Figure 6.2 of these glitch classes also support the ordering by t-SNE. Blip glitches have the lowest SNR and amplitude probability distribution, followed by Koi Fish, and Extremely Loud. Few Blip glitches pass the SNR > 100 threshold to be considered loud transient noise. There are some Extremely Loud glitches that have SNR < 100, many of these are associated with lock losses that saturate the omega-scans. The ordering of these Gravity Spy glitch classifications suggests there is an energy scale between Blip, Koi Fish and Extremely Loud glitches and these glitches may have the same or similar origins. The clustering of these glitch classes are also present in LHO, this is discussed in Appendix C.

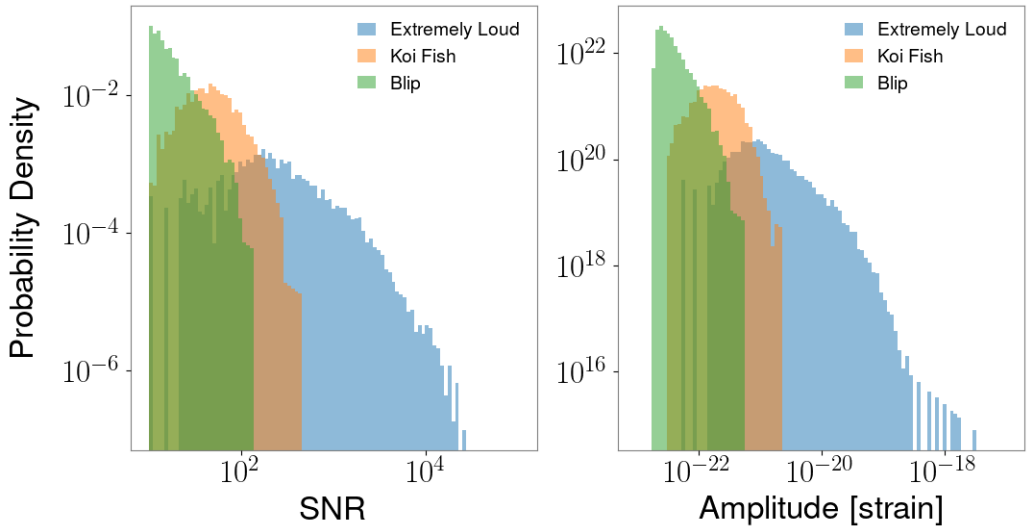

Figure 6.2. *Left*: SNR probability density distribution of Extremely Loud, Koi Fish and Blip glitches in O4a. *Right*: Amplitude probability density distribution of Extremely Loud, Koi Fish and Blip glitches in O4a.

6.2. Time Domain Analysis of Loud Transient Noise

Analyzing loud transient noise in the time domain is essential to understand their true duration in the aLIGO detectors. Characterizing their duration aids in searching and ruling out potential sources of noise. For this analysis, I applied t-SNE to the time series of O3 omicron triggers with SNR $>$ 1000. The time series data was cropped to include ± 0.025 s around the glitch. A short time segment for this analysis is crucial to avoid capturing too much of the low-frequency oscillation present in the GW strain data. Similarly to section 6.1, t-SNE reduces the time series data to two dimensions assigning X and Y coordinates.

The results from the t-SNE analysis on the time series of loud transient noise is shown in Figure 6.3. The primary feature that t-SNE captures of the time series of loud glitches is whether the glitch occurs near the maximum or minimum of the low-frequency oscillation in the GW strain data, as well as whether the glitch lacks the low-frequency

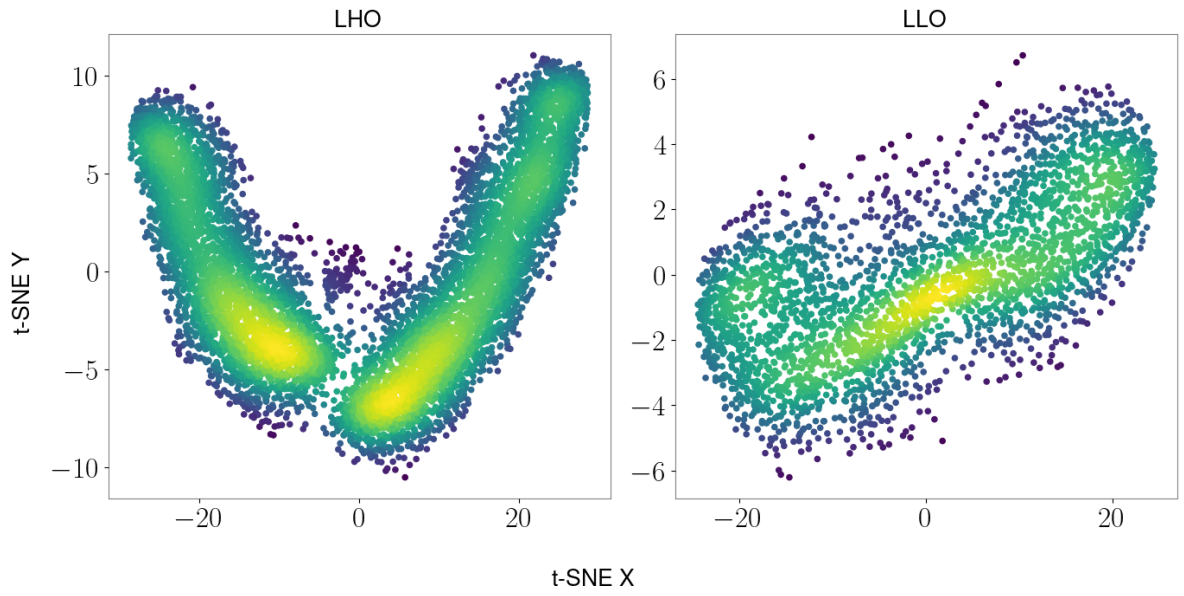

Figure 6.3. Result of t-SNE applied to time series of O3 loud glitches. Areas with the highest density of glitches are in yellow and the least dense regions are dark purple. *Left*: The left panel is the result for LHO. *Right*: The right panel is the result for LLO

oscillation component. This feature determined how t-SNE clustered the time series of loud glitches.

The t-SNE analysis of the time series of loud glitches revealed three distinct groups of glitches in LLO, left ($X < -10$), middle ($X > -10$ and $X < 10$), and right ($X > 10$). The primary difference between the left and right groups is the orientation of the low-frequency oscillation, which occurs at a maximum in the left group and a minimum in the right group. The probability distribution is largest at lower frequency for these glitches, whereas the center region of glitches distribution peaks at higher frequency, as shown in the center panel of Figure 6.5. Additionally, the SNR and amplitude distributions of the left and right groups peak at higher values than those of the center group, as illustrated in the left and right panels of Figure 6.5. Glitches in the center group comprise a mix where the largest amplitude of the glitch can be either positive or negative.

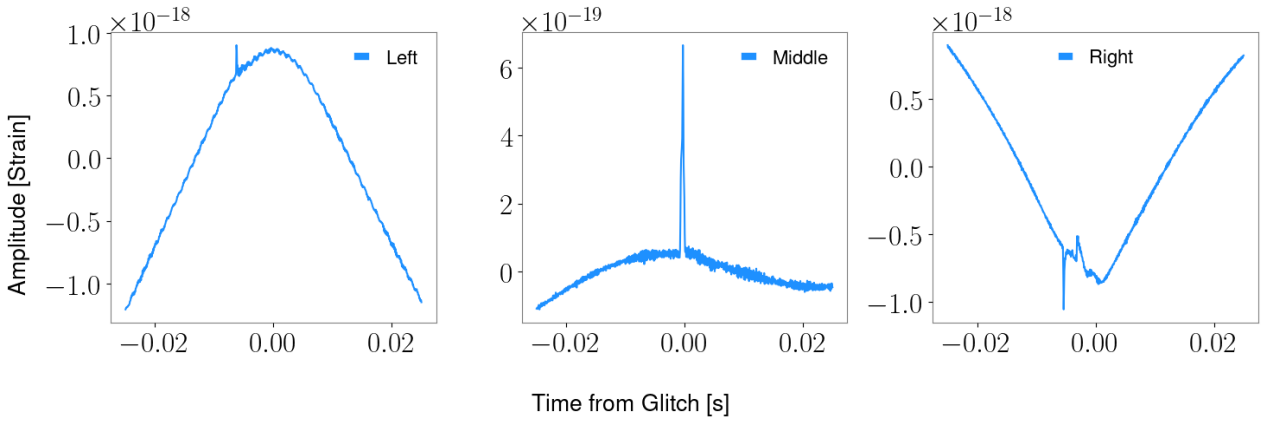

Figure 6.4. Examples of time series of loud transient noise in LLO. The coordinates given for each panel is referring to the LLO panel of Figure 6.3. *Left Panel*: Example of a glitch with X < -10. *Middle Panel*: Example of a glitch with X > -10 and X < 10. *Right Panel*: Example of a glitch with X > 10. The low-frequency component of the GW strain data is visible in the glitches shown in the left and right panels. The glitches in the left and right panels occur just before the glitch time assigned by the omicron algorithm.

In the t-SNE analysis of LHO (left panel of Figure 6.3), there are two distinct islands (left and right), each containing their own dense region of glitches at the bottom of the island, where Y $<$ 0. The glitches in the top left and top right regions at LHO are equivalent to the left and right region glitches at LLO. Again, the low-frequency oscillation of the GW strain reaches a maximum for the left regions and a minimum for the right regions. Unlike the LLO results, t-SNE is able to distinguish between the positive (bottom left) and negative (bottom right) amplitude glitches that do not contain the low-frequency component. This is likely because LHO had more glitches than LLO, providing more examples for the algorithm to identify as similar to each other Although t-SNE identifies four groups of glitches in LHO, the probability density distributions of Omicron parameters such as SNR, frequency, and amplitude do not vary significantly between the groups (Figure 6.6).

An important characteristic of loud transient noise is the duration. The Omicron

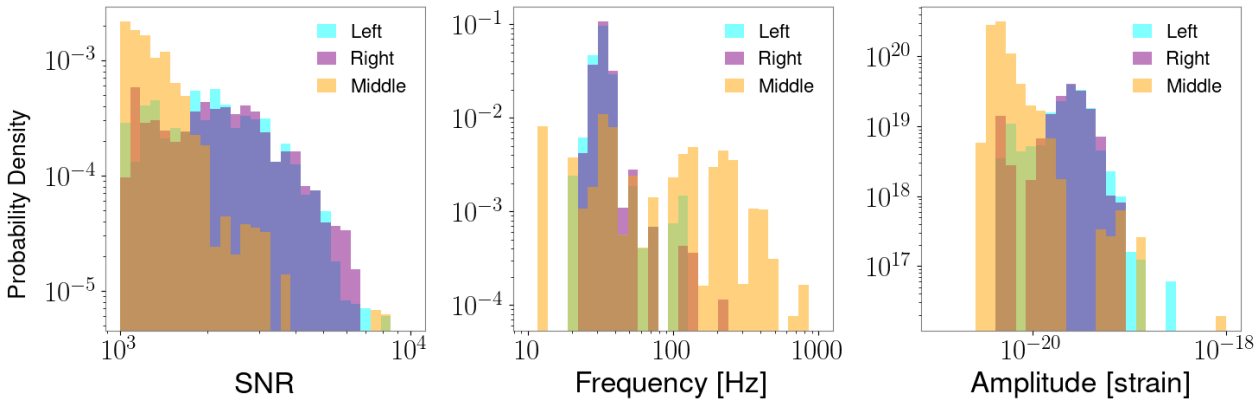

Figure 6.5. The probability density distributions for the Omicron parameters of sample triggers from the left (aqua), middle (orange) and right (purple) sections of the LLO panel of Figure 6.3. *Left Panel*: SNR of triggers. *Middle Panel*: Frequency of triggers. *Right Panel:* Amplitude of triggers.

algorithm provides a duration for all triggers that it observes, however the duration it provides for loud transient noise triggers can often be inaccurate. For this reason, I analyzed the loud transient noise triggers in the dense regions of Figure 6.3 for both LHO and LLO to determine their duration. The glitches in these regions were the most abundant type of loud transient with SNR $>$ 1000 in O3. The duration of a loud transient glitch is given by the width of the glitch in the time series data. I systematically found the widths of the loud transients, the results of this analysis are given in Figure 6.3. The probability density distribution of the duration of loud transients are similar in both instruments. The duration of the glitches range from $\sim 10^{-4} - 10^{-3}$ s. This duration is significantly shorter than those provided by the Omicron algorithm, which can give durations on the order of seconds for loud transient noise triggers. Considering this duration, we can investigate various aspects of the aLIGO instruments as potential sources of loud transient noise.

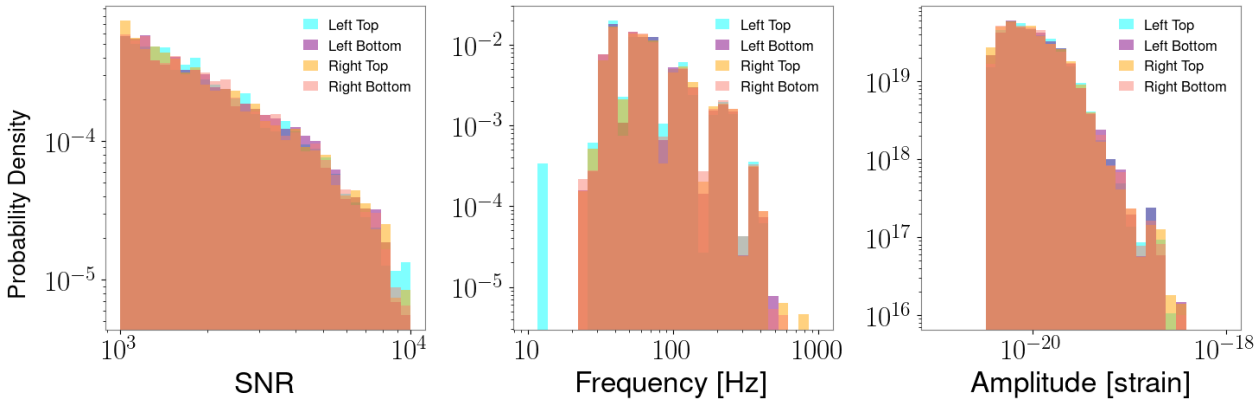

Figure 6.6. The probability density distributions for the Omicron parameters of sample triggers from the left top (aqua), left bottom (orange), right top (purple), and right bottom (pink) sections of the LHO panel of Figure 6.3. *Left Panel*: SNR of triggers. *Middle Panel*: Frequency of triggers. *Right Panel:* Amplitude of triggers.

6.3. Conclusion

In conclusion, the analysis of loud transient noise in aLIGO detectors using t-SNE on omega-scans and time series has revealed crucial insights into their morphology. The clustering results display the effectiveness of t-SNE in distinguishing glitch morphologies and suggested potential shared origins for certain Gravity Spy glitch classes. By leveraging t-SNE to cluster Gravity Spy classifications and time series data, distinct patterns and groups of glitches were identified, highlighting the similarities and differences in their characteristics between detectors. Additionally, the detailed investigation into the true duration of loud transients revealed that these glitches are significantly shorter than the durations assigned by the Omicron algorithm. These findings lay the foundation for the potential sources of loud transient noise I discuss in Chapter 7.

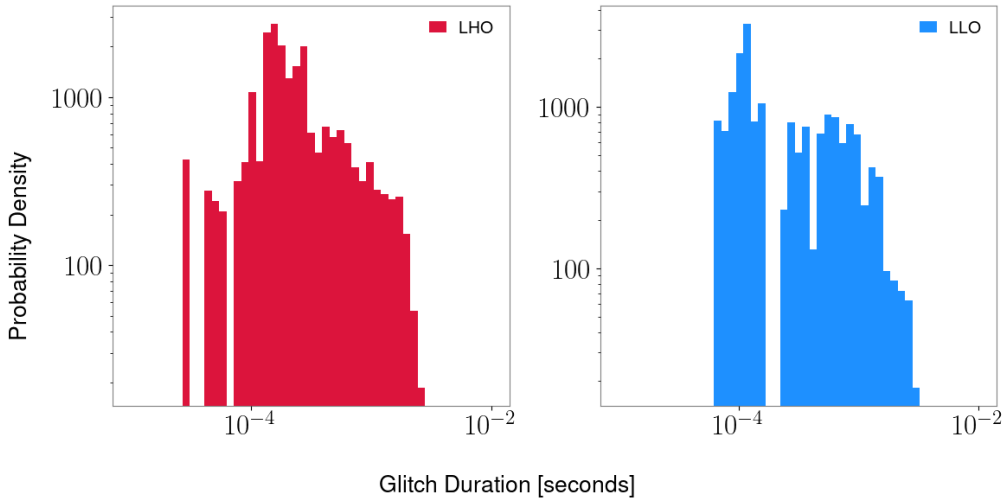

Figure 6.7. Probability density distribution of the glitch duration for a sample of loud glitches from the high-density regions from Figure 6.3. *Left*: LHO is displayed in red. *Right*: LLO is displayed in blue. Both detectors have a peak in the distribution near $\sim 10^{-3}$ s. In LHO there is a peak near $\sim 10^{-4}$ s and in LLO the peak is at $\sim 10^{-4}$ s.

Chapter 7. Potential Sources of Loud Transients

In this chapter, I present investigations into the potential sources of loud transient noise in the aLIGO detectors. These potential sources were chosen based on the previous work in this thesis. First, I estimate the potential impact of residual gases transiting the laser beam and discuss the role of dust particles within the vacuum system. Additionally, I present results from an experiment done at LLO to replicate loud transient noise in the DARM feedback control loop and analyze the behavior of these transient noise events. By investigating these sources, we gain more understanding of the behavior of loud transient noise in the aLIGO instruments.

7.1. Residual Gas

In the aLIGO detectors, achieving ultra-high vacuum conditions (10^{-9} Torr) is crucial for minimizing noise and ensuring the sensitivity required to detect GWs. Residual gas within the vacuum system can cause a variety of noise sources that affect the performance of the interferometer. These gases can introduce noise through several mechanisms, including molecular collisions with the test masses [58] and transversal travel through the laser beam in the arm cavity [59]. Despite extensive vacuum systems designed to reduce the presence of these gases, some residual gas remains and can contribute to the overall noise budget of the detector (refer to dashed olive line in Figure 2.6). In the case of loud transients, we suspect if residual gas molecules are large enough, the aLIGO would be sensitive to them transiting the laser beam. The vacuum chambers are vented during commissioning periods, which can alter vacuum conditions between observation runs and potentially cause the observed changes in glitch rates.

In statistical mechanics, the mean free path of a molecule is a measure of the average distance a particle travels between successive collisions with other particles. Since the aLIGO instruments operate with ultra-high vacuum, we assume that the molecules present in the vacuum chambers do not collide [60, 61]. The root mean square (rms) velocity of particles in a gas is given by the formula:

$$v_{rms} = \sqrt{\frac{3kT}{m}} \tag{7.1}$$

where k is the Boltzmann constant, T is the temperature in Kelvin and m is the mass of a single molecule. This formula represents the average velocity of gas molecules in a system, taking into account their kinetic energy and the distribution of velocities due to thermal motion. We can rearrange this formula to solve for the mass of the molecule, and substitute $v_{rms} = \frac{d}{t}$, where d is the beam diameter and t is the time it takes the molecule to cross the laser beam. For a loud transient glitch to occur from a molecule would need to transit in characteristic time of $\sim 0.1 - 1$ ms (section 6.2). We can consider a section of the arm cavity near the ITM and ETM, here the laser beam radii are 5.3 cm and 6.2 cm respectively. For a molecule to transit the laser beam in that time frame, the mass requirement of the particle near the ITM is $\sim 10^{-25} - 10^{-23}$ kg and near the ETM it is $\sim 10^{-26} - 10^{-24}$ kg. These mass estimates assume the particle travels directly across the diameter of the beam.

The total amount of each gas species present in the system, such as carbon dioxide, carbon dioxide, methane, and other hydrocarbons must be kept below different partial pressures to maintain operation [62]. For a 100 atomic mass unit (AMU) hydrocarbon ($\sim 10^{-25}$ kg), the average pressure required is 7.3×10^{-10} Torr, while for light gases such

as hydrogen the requirement is 10^{-6} Torr. These gas species have masses that are consistent with the masses necessary to transit the beam in the characteristic time of loud transient noise. To assess whether these gas species may cause loud transient noise, the rate of molecules transiting the laser beam must be consistent with the observed loud glitch rates (section 4.3).

We consider a volume, V, that contains molecules with mass, $m = 10^{-23}$ kg. We assume that the particles do not collide and the collisions between the particles and the walls of the volume are elastic collisions. When a molecule collides with the wall its trajectory is redirected, allowing it to cross through a laser beam that is in V, thus the number of wall bounces is equivalent to the number laser beam crossings. The number of molecules near the base of the volume is given by:

$$N_{base} = Adz\frac{N}{V}, \tag{7.2}$$

where A is the area, dz is the differential change in distance z, and $\frac{N}{V}$ is the total number of molecules per unit volume. If we multiply equation 7.2 by $\frac{dt}{dt}$ and the rate of collisions, or the rate of laser beam crossings is expressed as:

$$\frac{N_{base}}{dt} = A\frac{dz}{dt}\frac{N}{V}. \tag{7.3}$$

Here, $\frac{dz}{dt}$ is just the z-component of the velocity, v_z. To approximate the partial pressure necessary, we can rewrite equation 7.3 in terms of pressure (P) from the ideal gas law,

$$\frac{N}{V} = \frac{P}{kT}. \tag{7.4}$$

Now the rate is expressed as,

$$\frac{N_{base}}{dt} = 2\pi RLv_z\frac{P}{kT}. \tag{7.5}$$

We estimate the rate per hour of laser beam crossings from equation 7.5 using v_z for a 10^{-23} kg particle from equation 7.1, the radii for the ITM and ETM and the measured partial pressure of 10^{-13} Torr for heavier molecules in the aLIGO vacuum system (Figure 7.1). The rate per hour of molecules crossing the beam near the ITM and ETM is $\sim 10^{15}\frac{L}{m}$ per hour. This is many orders of magnitudes larger than the rates of loud transient noise observed in O2, O3 and O4a (section 4.3) and would appear as a stochastic noise, not single transients.

Residual gas analysis (RGA) scans are done at various locations around the interferometer to measure the partial pressures of the gas species that are in the vacuum system. From the RGA scan in Figure 7.1, the measured gas species do not exceed 100 AMU and the average partial pressure measured is $\sim 10^{-13}$ Torr.

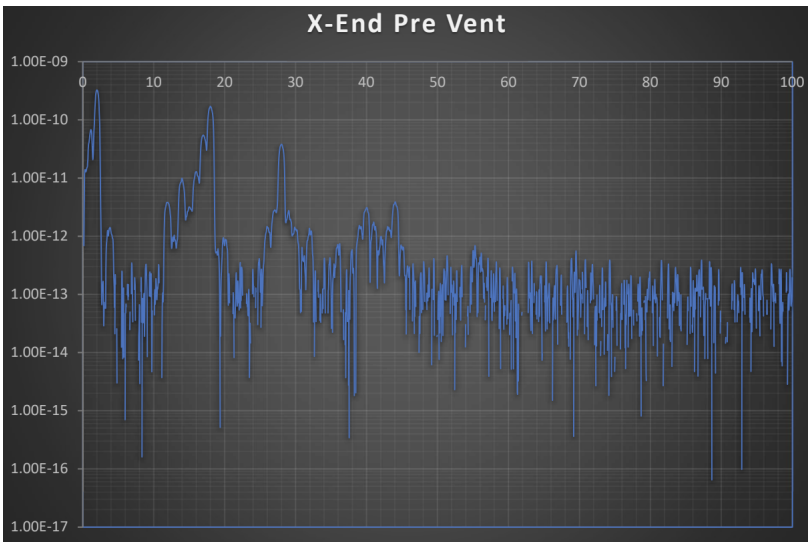

Figure 7.1. An example of an RGA scan performed at the ETMX vacuum chamber at LLO at the end of O4a. The scan has the AMU of various gas species on the x-axis and the partial pressure on the y-axis in $Torr$. [63]

From the approximation of the expected rate of molecules transiting the laser beam, I conclude residual gas molecules are not the source of loud glitches. The rate of

these residual gas crossings would likely create a noise spectrum, rather than individual transient events. Heavier gas molecules, or ensembles of gas molecules that travel in clusters at extremely low pressures (fewer molecules) would be necessary to be consistent with loud transient noise rates in the aLIGO detectors.

7.2. Dust Particles

Dust in the aLIGO instruments refers to particles in the vacuum system that are not residual gas molecules. These particles can come from oxidized metal falling from the chamber walls [64] or from contamination when work is performed inside of vented vacuum chambers. It has been theorized that dust may cause loud transient noise due to particles transiting and interacting with the laser beam. Vacuum chambers were tapped on in an experiment at LHO, which caused dust to fall through the beam and some transients were observed [64].

Dust differs from residual gas molecules as their interactions with the vacuum chambers are inelastic. They are also several orders of magnitude heavier than residual gas molecules, which would make their velocity too slow to transit the laser beam in the duration time found by the t-SNE analysis in section 6.2. Over the course of time, it is expected that dust in the vacuum system should settle. If dust is the cause of loud glitches in the aLIGO instruments then it is expected the glitch rate would also decrease over time. The analyses in section 4.3 show that the glitch rate at both detectors increase from O2 to O3 [65, 66], but decrease from O3 to O4a. This contradicts the idea of glitch rates decreasing over time. In the case that some contamination happened between O2 and O3 that caused the increased glitch rate, one would expect this to be localized to

one instrument. However, the glitch rate change between observation runs is the same for LHO and LLO. Environmental conditions such as wind and seismic noise can potentially influence dust interactions with the laser beam. If dust were responsible for the noise, we would expect an increase in glitch rates during storms or periods of high seismic activity. However, the rate of loud glitches does not correlate with these environmental factors. Given this evidence, it is unlikely that dust is the cause of the loud transient noise in the aLIGO detector.

7.3. DARM Feedback Control Loop

The interferometer sensing and control system has been suspected to be the cause of loud transient noise for several reasons. The aLIGO detectors are designed to be identical between LHO and LLO, but there are subtle differences between the control loops at each detector. The control loops of each detector are commissioned to provide the stability needed due to site-specific factors that may affect the performance of the feedback control system. These differences in commissioning procedures may lead to discrepancies in how each detector handles instrumental noise. Furthermore, changes observed between different observation runs highlight that the response of the control system to noise may evolve over time, possibly due to modifications performed during commissioning periods. This is supported by the variations of loud transient noise rates between instruments and observation runs (see Section 4.3). Collectively, these factors point towards the interferometer sensing and control system as a plausible source of the loud transient noise, warranting an investigation into its behavior. In particular, I focus on the DARM control loop, which is critical for GW detection.

Loud transient noise appears in the GW strain data, which is constructed from the input and output signals of the DARM control loop. The auxiliary channels that monitor input and output of the DARM loop also have loud transient noise that is coincident with the GW strain, as expected (examples shown in Figure 7.2). It has been suspected

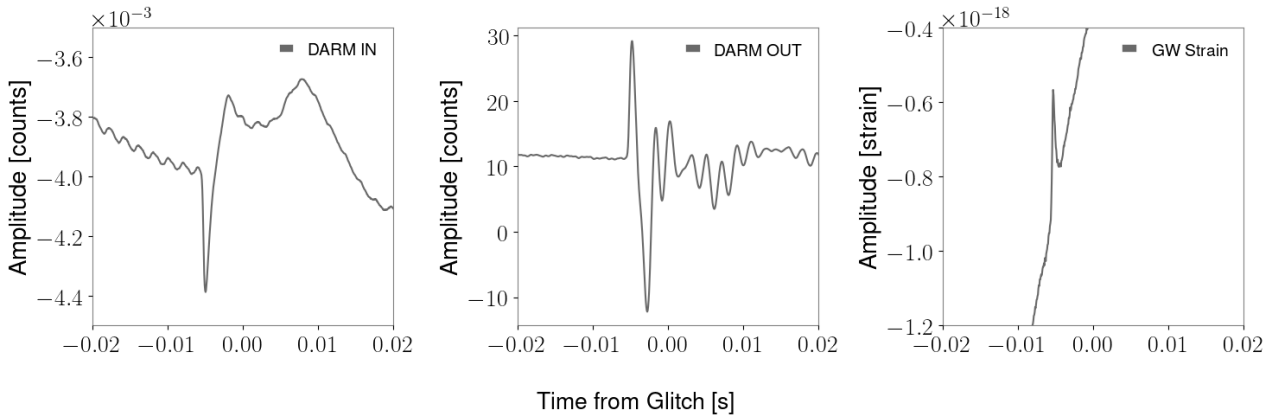

Figure 7.2. Example of a loud transient noise from a glitch in the GW strain data with SNR 1750. *Left Panel*: Time series of the glitch in `L1:LSC-DARM_IN1_DQ`. *Middle Panel*: Time series of the glitch in `L1:LSC-DARM_OUT_DQ`. *Right Panel*: Time series of the glitch in GW Strain.

that loud transient noise may be produced by the DARM loop itself. This was the motivation behind a series of DARM noise injections I performed (Figure 7.3) at LLO, with the goal of reproducing loud transient noise in the GW strain data and gaining a better understanding of the mechanism that causes it.

A series of injections with varying amplitudes were applied to the DARM Input to replicate the noise observed in the DARM control loop and GW strain data [67, 68]. The loud transient noise in this control loop has amplitudes ranging from approximately 10^{-4} to 10^{-3} counts. The amplitudes (in units of DARM counts) used for the injections were 10^{-4}, the second set 5×10^{-4}, and the third set 10^{-3}. Based on the analysis in section 6.2, the injection durations used were 0.1 and 0.5 ms. Each set contained six Gaussians with

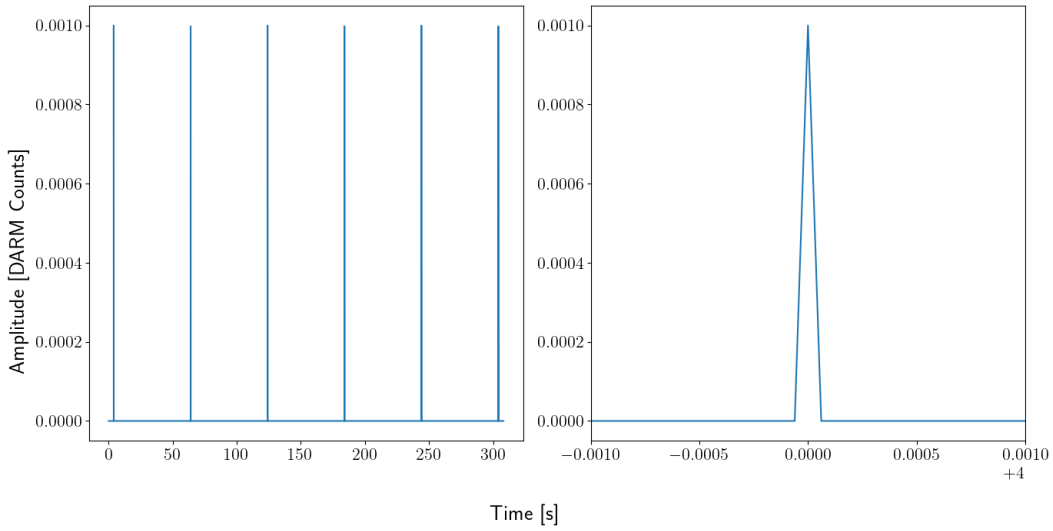

Figure 7.3. *Left Panel*: An example of a waveform used for loud glitch injections. The injections were separated by 60 s to allow for the interferometer to return to its nominal state between injections. The injected glitch durations alternate between 0.1 and 0.5 ms. *Right Panel*: Zoom in of one injection.

the duration (width of the Gaussian) alternating between 0.1 and 0.5 ms. Similarly to real loud transient noise, the injected glitches briefly saturate the coil drivers on the test masses used for actuation (section 4.2), saturation is reached when the amplitude reaches 2^{19} counts or more.

Figure 7.4 shows examples of three DARM glitch injections, as observed in the GW strain data. The omega-scans of the primary GW channel show a Blip glitch (left panel) from an injection with amplitude 5×10^{-4}, a Koi Fish glitch (middle panel) from an injection with amplitude 5×10^{-4} and an Extremely Loud (right panel) glitch from an injection with amplitude 10^{-3}. The same type of injection produced both the Blip and Koi Fish, supporting the overlap between glitch classes. This maybe due to the state of the interferometer at the time of the injection. All three glitches were produced using a duration of 0.5 ms. The SNR of these injected transients in the GW strain data for the Blip, Koi Fish and Extremely Loud were 41, 91, 420, respectively. The results of the injections further

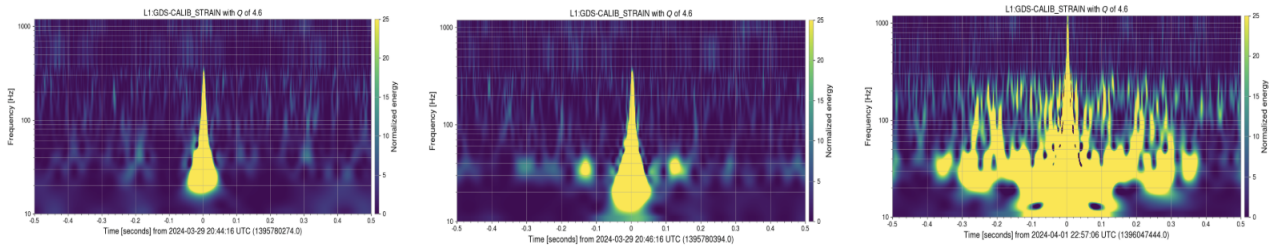

Figure 7.4. Omega-scan examples of loud glitch injections in the GW strain data. *Left Panel*: Injection produced a Blip glitch. *Middle Panel*: Injection produced a Koi Fish glitch. *Right Panel*: Injection produced an Extremely Loud glitch.

supports the theory that Blips, Koi Fish, and Extremely Loud glitches have a common source with an energy scale that separates them into different classifications (discussed in sections 5.4 and 6.1).

The injected glitches are witnessed by similar channels as real loud transient noise such as the ESD voltage monitors (section 5.1) and the ISI channels (section 5.4). To compare the injections to real loud transient noise in LLO, I created omega-scans for a random sample of glitch times and for the injection times. The omega-scans provide the

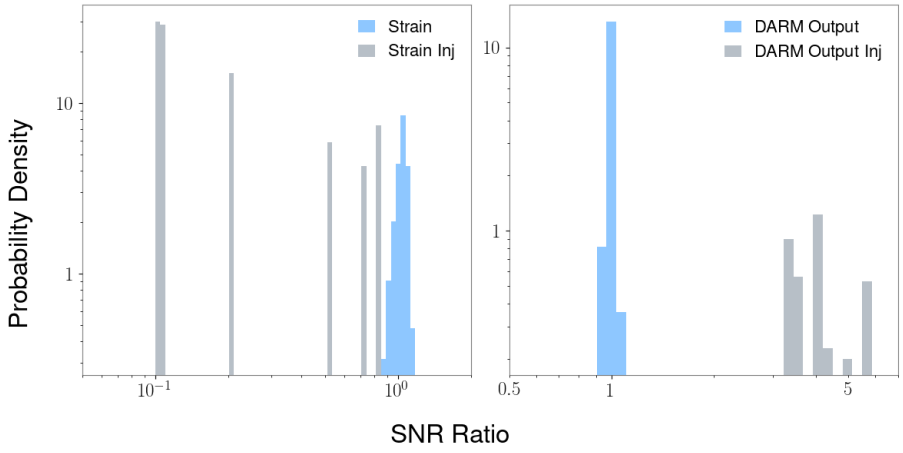

Figure 7.5. Distributions of the SNR ratio of a sample of O4a loud glitches and the injected glitches. *Left*: The ratios shown are of the GW Strain to DARM Input of real glitches (blue) and injected glitches (gray). *Right*: The ratios shown are of DARM Output to DARM Input of real glitches (blue) and injected glitches (gray).

glitch SNR for each channel, Figure 7.5 shows histograms of the SNR ratios for the GW Strain, DARM Input, and DARM Output to DARM Input for both the real and injected glitches. As expected the SNR ratio for DARM Input is one for both the real loud transients and the injected loud transients. In the GW strain and DARM Output, observed loud glitches in O4a have an SNR ratio close to one. For the injected transients the SNR ratio in the GW strain channel is much less than one, and in the DARM output, the SNR ratio is $\sim 3-5\times$ larger than one. The injected glitches appear much louder in the DARM Output due to the transfer function (Figure 7.6) between the Input and Output control loops. The injected glitches are high frequency ($\sim$ 1000 Hz) and there is a gain with mag-

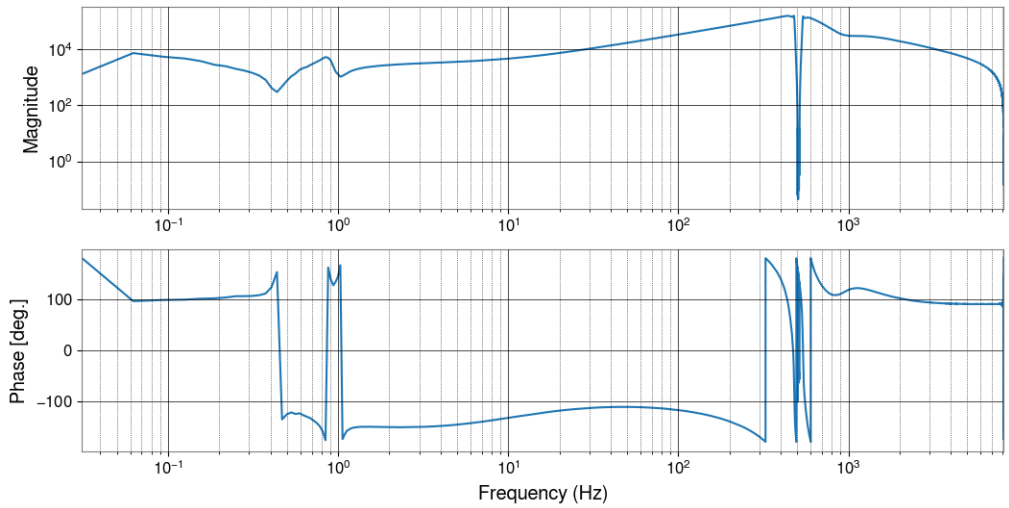

Figure 7.6. The transfer function between the DARM input control signal `L1:LSC-DARM_IN1_DQ` and DARM output control signal `L1:LSC-DARM_OUT_DQ`.

nitude $\sim 10^4$ at this frequency. Due to the location of the injections, the gain applied in the DARM control loop manifests as a higher SNR in the DARM Output glitches. From this experiment, I conclude that the DARM control loop is not responsible for the loud transient noise observed in the GW strain data. Loud transient noise must couple into the

DARM control loop from another point in the interferometer, that evades that gain applied between the Input and Output control loops and produces a similar SNR in the GW strain data and DARM control loops.

7.4. Conclusion

In conclusion, the investigation into these potential sources of loud transient noise has provided valuable insights into the behavior of these glitches. I have shown that molecule and particle interactions with the laser beam do not agree with the observed glitch rates, indicating that other unidentified sources or mechanisms may be causing loud glitches. Through a series of controlled noise injections, I have demonstrated that the DARM control loop itself is not the primary source of these transient noise events. Instead, the analysis suggests that noise is coupling into the DARM control loop from another location in the detector. The findings underscore the importance of continued investigation into the instrumental factors affecting the aLIGO instruments.

Chapter 8. Conclusion

We are at the beginning of the age of gravitational wave and multi-messenger astronomy. These ripples in spacetime, first predicted by Albert Einstein over a century ago, have opened a new window into the universe, allowing us to observe cosmic events that were previously beyond our reach. The performance and sensitivity of aLIGO instruments are improving at a rapid pace, and we are detecting GW from the cataclysmic mergers of black holes and neutron stars weekly when observing. There are more sources of GW still to be detected, such as bursts from supernovae, continuous waves from pulsars, and the cosmological and astrophysical stochastic background. These detectors are at the forefront of GW astronomy; however, the sensitivity of these detectors also makes them susceptible to various sources of transient noise that can obscure or mimic genuine GW signals.

This thesis focused on loud transient noise, SNR > 100, with an emphasis on the loudest transients SNR > 1000. Loud transient noise impacts the BNS range of the aLIGO interferometers (Chapter 4). Chapter 4 also highlighted the Omicron characteristics of loud transient noise across O2, O3, and O4a. Although the sensitivity of the interferometers improves over time, the SNR and amplitude of loud glitches do not increase. I also analyzed the glitch rates across observation runs, showing that the rate changes over time and that the daily rate of loud glitches fits a Poisson distribution, indicating that these glitches occur independently of each other.

The aLIGO interferometers use auxiliary data channels to constantly monitor environmental and instrumental conditions. Through a thorough assessment of various channels, we identified those that are significantly impacted by loud transient noise (Chapter 5). This process involved a detailed examination of the relationships between auxiliary

channels and their correlation with the GW strain data. During O3, the ESD voltage monitor channels were correlated to loud transient noise in the GW strain data at LLO; however, I showed these channels were not the cause of the noise in the strain data. The use of H-veto to analyze the thousands of auxiliary channels identified interferometer sensing and control auxiliary channels that are unsafe due to their propensity to witness loud glitches in the GW strain data. The H-veto analysis also showed that Koi Fish and the loudest transient noise are witnessed by the same auxiliary channels.

Chapter 6 applied a machine learning algorithm, t-SNE, to the cluster omega-scans of Gravity Spy glitch classes and the time series of loud transient noise. The clustering of Blip, Koi Fish, and Extremely Loud glitches together supports the theory that there is an energy scale between these classifications and that they may have the same origins. Applying t-SNE to the time series of loud glitches revealed different morphologies of loud transient noise in the time domain. This analysis also laid the groundwork to determine a characteristic duration of loud glitches in the aLIGO detectors. Identifying the true duration of loud transient noise is imperative for searching for their origin.

Chapter 7 discussed three potential sources of loud transient noise: residual gases, dust, and the DARM control loop. Although these were promising candidates as the source of loud transient noise, I proved that the rate of residual gas molecules interacting with the laser beam is several orders of magnitude too high to explain the observed rates of loud transient noise. The behavior of loud transient noise is inconsistent with dust particles as a source as it would be affected by environmental conditions and seismic noise. Dust particles are also heavier than residual gas molecules; therefore, they would travel slower than the duration of loud transients in the aLIGO instruments. A pivotal aspect of

this research was the investigation of the DARM control loop, which is necessary to detect GW signals. The experiment to reproduce loud transient noise in the detector via noise injections ruled out the DARM control loop as a potential source. Despite null results from these investigations, we have gained a greater understanding of the behavior of loud transient noise in the aLIGO detectors.

The insights gained from this thesis lay a solid groundwork for future research on loud transient noise. Gravity Spy has expanded our understanding of various glitch classifications; however, to accurately identify the sources of loud transient noise, it is crucial to focus more on the similarities among certain classifications. The noise injections conducted in this study reveal that Blip, Koi Fish, and Extremely Loud glitches can manifest in the GW strain data from different noise amplitudes. It is possible that the transient noise is created by other control loops and couples to DARM; however, the coupling mechanism must be different than the location of my noise injections as this noise evades the gain applied between the DARM Input and Output. Due to the high-frequency nature of loud glitches, a potential avenue of research is the common arm readout measurement (CARM) control loop and the frequency stabilization system as they operate with high frequency. It is essential to emphasize performing "Detector Characterization Noise Injections" aimed at reproducing transient noise in the GW strain data. These injections will enable us to compare and contrast real loud transient noise with injected noise, providing deeper insights and potentially leading to the identification of their sources.

In conclusion, this thesis has made significant contributions to understanding the behavior of loud transient noise in the aLIGO instruments. By analyzing various aspects of the aLIGO detector data in relation to loud transient noise, we have laid the ground-

work for future advancements in this exciting area of research. The methodologies and insights developed in this work will serve as a foundation for ongoing research and development, hopefully leading to the mitigation of loud transient noise in the detector data and improved data quality for gravitational wave search methods. As we continue to push the boundaries of our knowledge, the future of gravitational wave astronomy looks promising, with the potential to uncover new and profound insights into the nature of the universe.

Appendix A. Discussion of Loud Glitch Characteristics

It is informative to compare some omicron parameters of loud glitches as a function of one another. Here, I will further discuss the frequency and amplitude of loud glitches as a function of SNR.

A.1. Frequency

The frequency of loud glitches as a function of SNR is shown in A.1. The high-frequency population of O2 loud glitches is confined to SNRs below 5000 in LHO, while in LLO, all but one loud glitch are confined to SNRs below 3000. However, in O3 and O4a, the high and low-frequency populations of glitches exhibit a broad range of SNRs in both instruments. Between $\sim 70 - 200$ Hz, there is a dip in the SNR of loud glitches. This dip is most prominent in LLO during O4a and least prominent in LHO during O3.

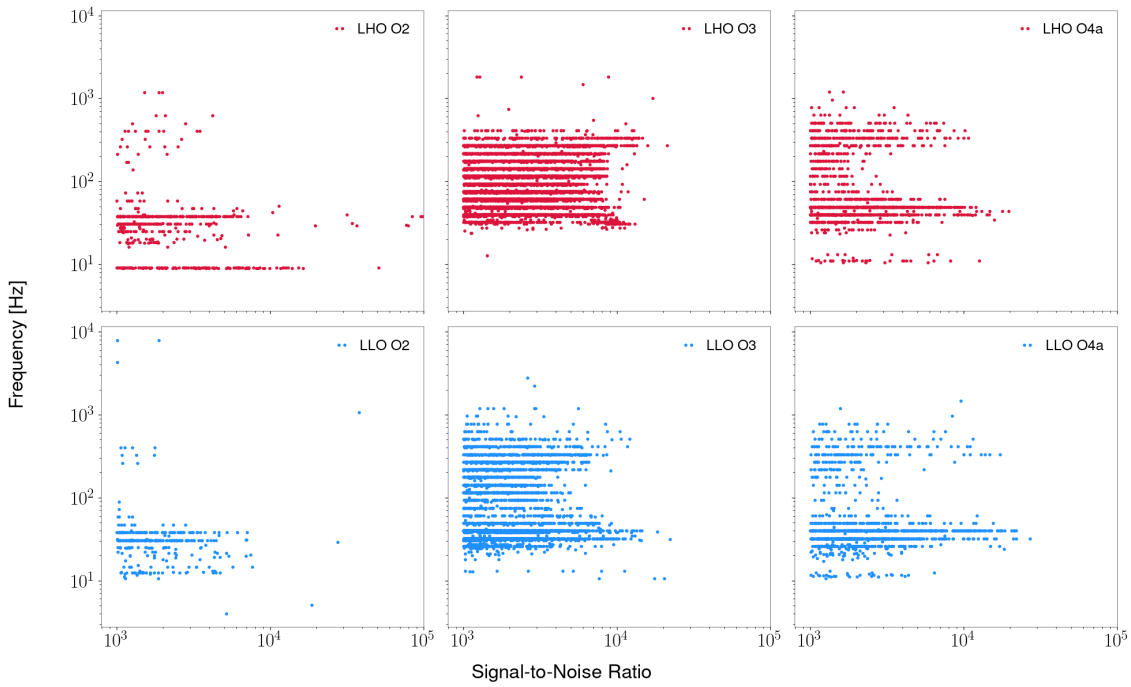

Figure A.1. Frequency of loud glitches as a function of SNR for O2, O3, and O4a in LHO (*top row*) and LLO (*bottom row*). Each point represents a loud glitch omicron trigger.

A.2. Amplitude

The amplitude of loud glitches as a function of SNR is shown in A.1. The linear relationship is present across O2, O3, and O4a in both LIGO instruments. As mentioned in section 4.1 of chapter 4, there is a presence of a population higher amplitude glitches. These glitches have frequency below $\sim$ 15 Hz, seen as a horizontal line of triggers in Figure A.1. It is interesting to note that, although this population has larger amplitudes, their SNRs occupy the same range as the $\sim 10^{-20} - 10^{-17}$ strain glitches.

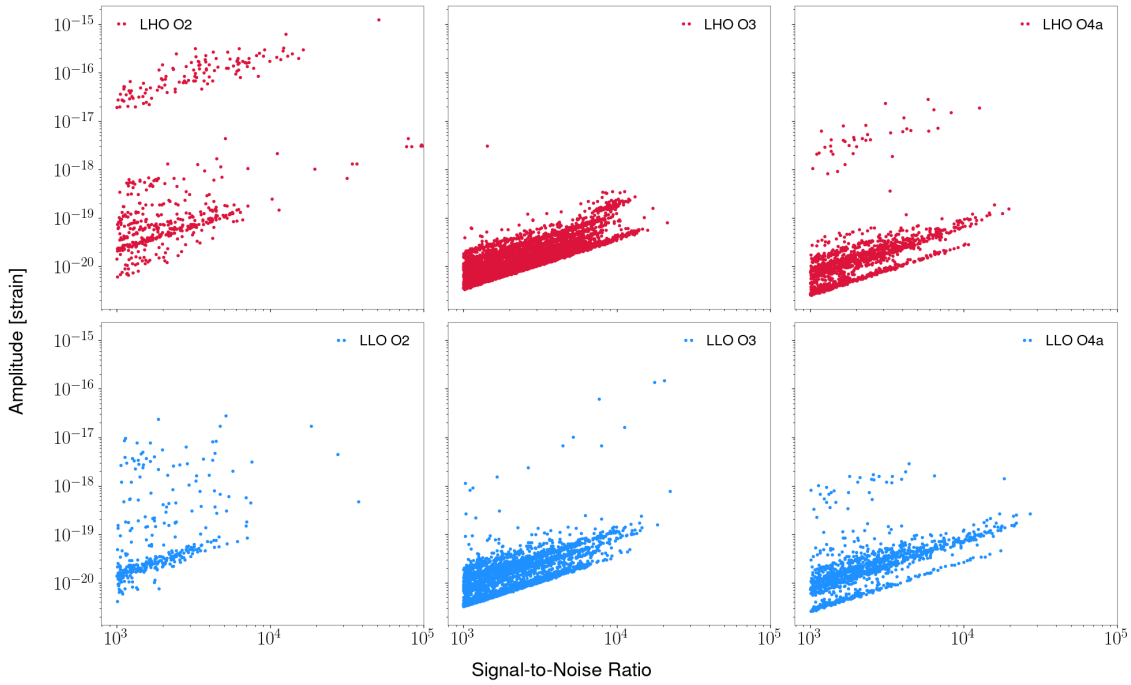

Figure A.2. Amplitude of loud glitches as a function of SNR for O2, O3, and O4a in LHO (*top row*) and LLO (*bottom row*). Each point represents a loud glitch omicron trigger.

A.3. Impact on Binary Neutron Star Range

The BNS range of the aLIGO detectors are significantly impacted by the occurrence of loud transient noise. Figure A.3 displays the omicron parameters SNR, frequency, and amplitude as a function of the BNS range at the time of a loud glitch in both LHO and LLO. There is no significant correlation between these omicron parameters and the

range drops caused by loud glitches.

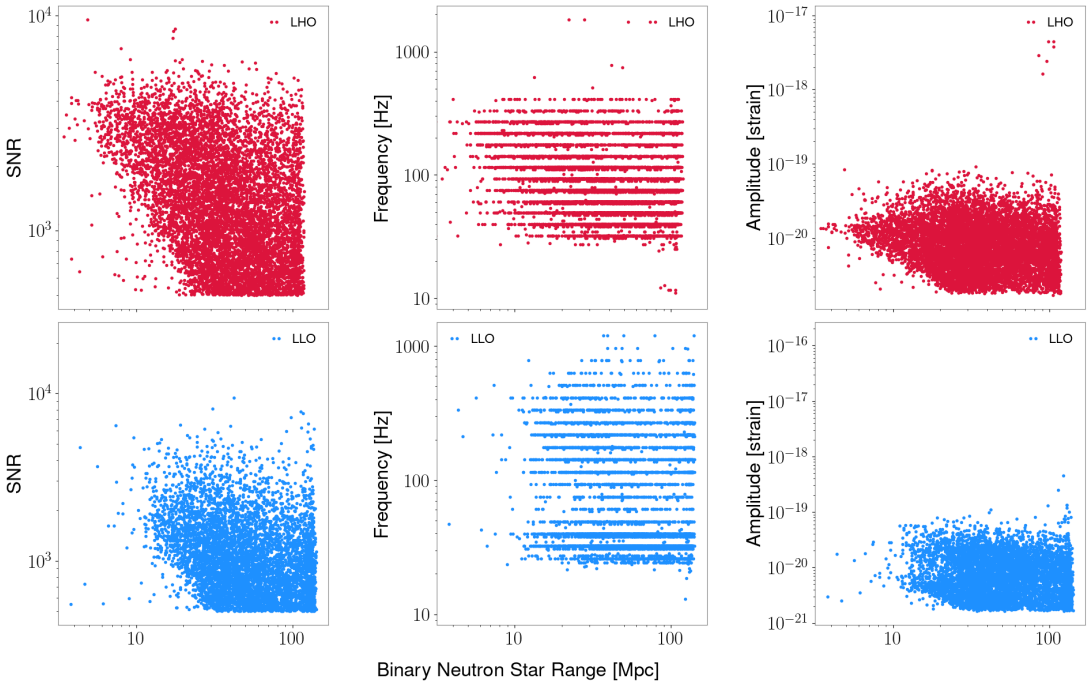

Figure A.3. Omicron parameters SNR, frequency, and amplitude as a function of BNS range in O3. *Top Row*: LHO is displayed in red. *Bottom Row*: LLO is displayed in blue.

Appendix B. Auxiliary Witness Channels

I analyzed all the channels that were found to be statistically significant by H-veto and created this list of channels that I consider unsafe, or witnesses, of loud transient noise.

These channels witness loud glitches in the GW strain data:

- L1:ASC-AS_A_RF45_I_PIT_OUT_DQ
- L1:ASC-AS_A_RF45_I_YAW_OUT_DQ
- L1:ASC-AS_A_RF45_Q_PIT_OUT_DQ
- L1:ASC-AS_A_RF45_Q_YAW_OUT_DQ
- L1:ASC-AS_B_RF45_I_PIT_OUT_DQ
- L1:ASC-AS_B_RF45_I_YAW_OUT_DQ
- L1:ASC-AS_B_RF45_Q_PIT_OUT_DQ
- L1:ASC-AS_B_RF45_Q_YAW_OUT_DQ
- L1:ASC-SRC1_P_OUT_DQ
- L1:ASC-SRC1_Y_OUT_DQ
- L1:ASC-X_TR_A_NSUM_OUT_DQ
- L1:ASC-X_TR_B_NSUM_OUT_DQ
- L1:ASC-Y_TR_A_NSUM_OUT_DQ
- L1:ASC-Y_TR_B_NSUM_OUT_DQ
- L1:LSC-POP_A_LF_DQ
- L1:LSC-REFL_A_LF_OUT_DQ
- L1:PEM-EX_VMON_ETMX_ESDPOWER18_DQ
- L1:PEM-EX_VMON_ETMX_ESDPOWER24_DQ

- L1:PEM-EY_VMON_ETMY_ESDPOWER18_DQ
- L1:PEM-EY_VMON_ETMY_ESDPOWER24_DQ

These channels are deemed unsafe as they are related to the channels that witness the loud glitches:

- L1:ASC-DHARD_P_A_OUT_DQ
- L1:ASC-DHARD_P_B_OUT_DQ
- L1:ASC-DHARD_P_OUT_DQ
- L1:ASC-DHARD_Y_A_OUT_DQ
- L1:ASC-DHARD_Y_B_OUT_DQ
- L1:ASC-DHARD_Y_OUT_DQ

These channels are deemed unsafe as their significance is reduced after vetoing the round winner:

- L1:ASC-REFL_A_DC_SUM_OUT_DQ
- L1:ASC-REFL_A_RF9_Q_PIT_OUT_DQ
- L1:ASC-REFL_A_RF9_Q_YAW_OUT_DQ
- L1:ASC-REFL_A_RF9_I_YAW_OUT_DQ
- L1:ASC-REFL_A_RF9_I_PIT_OUT_DQ
- L1:ASC-REFL_A_RF45_I_YAW_OUT_DQ
- L1:ASC-REFL_A_RF45_I_PIT_OUT_DQ
- L1:ASC-REFL_A_RF45_Q_YAW_OUT_DQ
- L1:ASC-REFL_A_RF45_Q_PIT_OUT_DQ
- L1:ASC-REFL_B_DC_SUM_OUT_DQ
- L1:ASC-REFL_B_RF9_Q_PIT_OUT_DQ

- L1:ASC-REFL_B_RF45_Q_PIT_OUT_DQ
- L1:ASC-REFL_B_RF9_I_PIT_OUT_DQ
- L1:ASC-REFL_B_RF45_I_PIT_OUT_DQ
- L1:ASC-REFL_B_RF9_Q_YAW_OUT_DQ
- L1:ASC-REFL_B_RF45_Q_YAW_OUT_DQ
- L1:ASC-REFL_B_RF9_I_YAW_OUT_DQ
- L1:ASC-REFL_B_RF45_I_YAW_OUT_DQ
- L1:OMC-PZT1_MON_AC_OUT_DQ
- L1:OMC-PZT2_MON_AC_OUT_DQ
- L1:LSC-MICH_IN1_DQ
- L1:LSC-MICH_OUT_DQ
- L1:LSC-PRCL_IN1_DQ
- L1:LSC-PRCL_OUT_DQ
- L1:LSC-REFL_A_RF45_I_ERR_DQ
- L1:LSC-REFL_A_RF45_Q_ERR_DQ
- L1:LSC-REFL_A_RF9_Q_ERR_DQ
- L1:LSC-POP_A_RF45_I_ERR_DQ
- L1:LSC-POP_A_RF45_Q_ERR_DQ
- L1:LSC-POP_A_RF9_I_ERR_DQ
- L1:LSC-SRCL_IN1_DQ
- L1:LSC-SRCL_OUT_DQ
- L1:ASC-X_TR_A_PIT_OUT_DQ
- L1:ASC-X_TR_A_YAW_OUT_DQ

- L1:ASC-X_TR_B_PIT_OUT_DQ
- L1:ASC-X_TR_B_YAW_OUT_DQ
- L1:ASC-AS_A_RF36_I_PIT_OUT_DQ
- L1:ASC-AS_A_RF36_I_YAW_OUT_DQ
- L1:ASC-AS_A_RF36_Q_PIT_OUT_DQ
- L1:ASC-AS_A_RF36_Q_YAW_OUT_DQ
- L1:ASC-AS_B_RF36_I_PIT_OUT_DQ
- L1:ASC-AS_B_RF36_I_YAW_OUT_DQ
- L1:ASC-AS_B_RF36_Q_PIT_OUT_DQ
- L1:ASC-AS_B_RF36_Q_YAW_OUT_DQ
- L1:ASC-MICH_Y_OUT_DQ

Triggers in these channels are do not have many coincidences with GW strain triggers:

- L1:ASC-MICH_P_OUT_DQ
- L1:IMC-IM4_TRANS_SUM_OUT_DQ

Appendix C. Hanford t-SNE on Gravity Spy Glitch Classes

The clustering of glitches identified as Blip, Koi Fish and Extremely Loud by Gravity Spy is also present in LHO. Here I provide preliminary results of t-SNE applied to O4a glitches between May 24, 2023 and October 1, 2023 at LHO. Similar to the LLO results

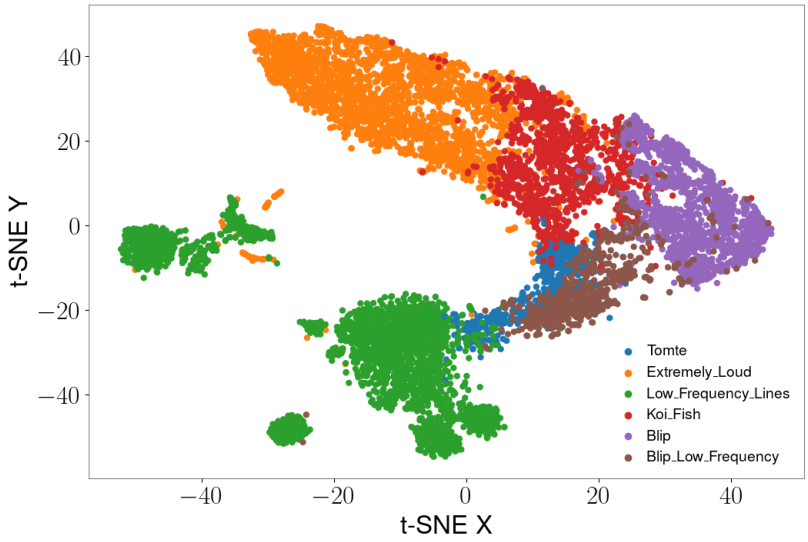

Figure C.1. t-SNE clustering results for different Gravity Spy glitch classifications in LHO from May 24, 2023 to October 1, 2023. Each Gravity Spy classification is represented by a different color.

discussed in 6.1, t-SNE again groups Blip, Koi Fish, and Extremely Loud glitches in the LHO data.

Figure C.2, shows the omicron parameters SNR and amplitude for the LHO Blip, Koi Fish, and Extremely Loud glitches, similar to the LLO results discussed in 6.1. The similarity in results between LHO and LLO provides more support that these glitch classification may have a common origin and there is an energy scale that defines the glitch type.

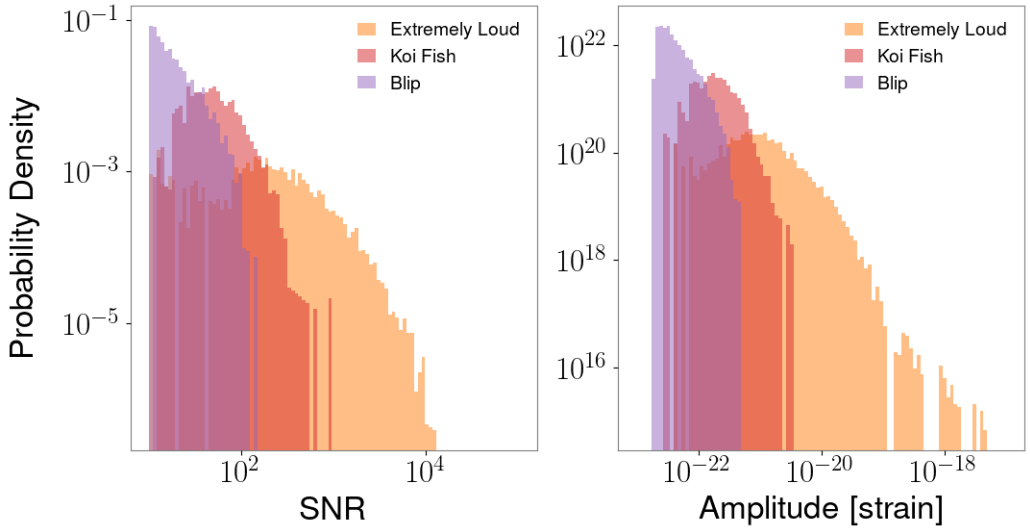

Figure C.2. *Left*: SNR probability density distribution of Extremely Loud, Koi Fish and Blip glitches in O4a at LHO. *Right*: Amplitude probability density distribution of Extremely Loud, Koi Fish and Blip glitches in O4a at LHO.

Bibliography

[1] Albert Einstein. The Formal Foundation of the General Theory of Relativity. *Sitzungsber. Preuss. Akad. Wiss. Berlin (Math. Phys.)*, 1914:1030–1085, 1914.

[2] Isaac Newton. *Philosophiæ Naturalis Principia Mathematica*. England, 1687.

[3] R. A. Hulse and J. H. Taylor. Discovery of a pulsar in a binary system. *Astrophys. J. Lett.*, 195:L51–L53, 1975.

[4] B. P. Abbott et al. Observation of Gravitational Waves from a Binary Black Hole Merger. *Phys. Rev. Lett.*, 116(6):061102, 2016.

[5] Robert Johnston. Gravitational wave-related images.

[6] Karl Wette. Searches for continuous gravitational waves from neutron stars: A twenty-year retrospective. *Astropart. Phys.*, 153:102880, 2023.

[7] Benjamin P. Abbott et al. First search for gravitational waves from known pulsars with Advanced LIGO. *Astrophys. J.*, 839(1):12, 2017. [Erratum: Astrophys.J. 851, 71 (2017)].

[8] R. Abbott et al. All-sky search for short gravitational-wave bursts in the third Advanced LIGO and Advanced Virgo run. *Phys. Rev. D*, 104(12):122004, 2021.

[9] Nelson Christensen. Stochastic Gravitational Wave Backgrounds. *Rept. Prog. Phys.*, 82(1):016903, 2019.

[10] B. P. Abbott et al. Binary Black Hole Mergers in the first Advanced LIGO Observing Run. *Phys. Rev. X*, 6(4):041015, 2016. [Erratum: Phys.Rev.X 8, 039903 (2018)].

[11] B. P. Abbott et al. GWTC-1: A Gravitational-Wave Transient Catalog of Compact Binary Mergers Observed by LIGO and Virgo during the First and Second Observing Runs. *Phys. Rev. X*, 9(3):031040, 2019.

[12] B. P. Abbott et al. GW170817: Observation of Gravitational Waves from a Binary Neutron Star Inspiral. *Phys. Rev. Lett.*, 119(16):161101, 2017.

[13] R. Abbott et al. GWTC-2: Compact Binary Coalescences Observed by LIGO and Virgo During the First Half of the Third Observing Run. *Phys. Rev. X*, 11:021053, 2021.

[14] R. Abbott et al. GWTC-3: Compact Binary Coalescences Observed by LIGO and Virgo during the Second Part of the Third Observing Run. *Phys. Rev. X*, 13(4):041039, 2023.

[15] A. G. Abac et al. Observation of Gravitational Waves from the Coalescence of a $2.5 - 4.5\ M_\odot$ Compact Object and a Neutron Star. 4 2024.

[16] Aaron Geller. Masses in the Stellar Graveyard.

[17] California Institute of Technology. Basic Michelson Interferometer.

[18] Craig Cahillane and Georgia Mansell. Review of the Advanced LIGO Gravitational Wave Observatories Leading to Observing Run Four. *Galaxies*, 10(1):36, 2022.

[19] Nina Bode et al. Advanced LIGO Laser Systems for O3 and Future Observation Runs. *Galaxies*, 8(4):84, 2020.

[20] X Y. et al. Sensitivity and performance of the Advanced LIGO detectors in the fourth observing run. *paper in preparation.*

[21] Fritschel, P., Yamamoto, H., Mueller, and Arain, M. Stable Recycling Cavities for Advanced LIGO. Technical Report T080208, LSC, 2008.

[22] M. Tse et al. Quantum-Enhanced Advanced LIGO Detectors in the Era of Gravitational-Wave Astronomy. *Phys. Rev. Lett.*, 123(23):231107, 2019.

[23] D. Ganapathy et al. Broadband Quantum Enhancement of the LIGO Detectors with Frequency-Dependent Squeezing. *Phys. Rev. X*, 13(4):041021, 2023.

[24] Sheila E. Dwyer, Georgia L. Mansell, and Lee McCuller. Squeezing in Gravitational Wave Detectors. *Galaxies*, 10(2):46, 2022.

[25] L. McCuller et al. Frequency-Dependent Squeezing for Advanced LIGO. *Phys. Rev. Lett.*, 124(17):171102, 2020.

[26] B.C. Seymour, M. Kasprzack, A. Pele, and A. Mullavey. Characterization on Non-linear Angular Noise Coupling into Differential Arm Length of the LIGO Livingston Detector. Technical Report T1700343, LSC, 2017.

[27] Craig Cahillane, Joe Betzwieser, Duncan A. Brown, Evan Goetz, Evan D. Hall, Kiwamu Izumi, Shivaraj Kandhasamy, Sudarshan Karki, Jeff S. Kissel, Greg Mendell, Richard L. Savage, Darkhan Tuyenbayev, Alex Urban, Aaron Viets, Madeline Wade, and Alan J. Weinstein. Calibration uncertainty for advanced ligo's first and second observing runs. *Physical Review D*, 96(10), November 2017.

[28] D. Tuyenbayev et al. Improving LIGO calibration accuracy by tracking and compensating for slow temporal variations. *Class. Quant. Grav.*, 34(1):015002, 2017.

[29] Peter R Saulson. *Fundamentals of Interferometric Gravitational Wave Detectors.*

WORLD SCIENTIFIC, 1994.

[30] Gabriela Gonzalez. Suspensions thermal noise in LIGO gravitational wave detector. *Class. Quant. Grav.*, 17:4409–4436, 2000.

[31] Gabriela I Gonzalez and Peter R Saulson. Brownian motion of a mass suspended by an anelastic wire. *The Journal of the Acoustical Society of America*, 96(1):207–212, 1994.

[32] J. Steinlechner. Development of mirror coatings for gravitational-wave detectors. *Phil. Trans. Roy. Soc. Lond. A*, 376(2120):20170282, 2018.

[33] California Institute of Technology. Advanced LIGO Suspension.

[34] S. M. Aston et al. Update on quadruple suspension design for Advanced LIGO. *Class. Quant. Grav.*, 29(23):235004, 2012.

[35] S. Wen et al. Hydraulic External Pre-Isolator System for LIGO. *Class. Quant. Grav.*, 31(23):235001, 2014.

[36] Aaron Buikema et al. Sensitivity and performance of the Advanced LIGO detectors in the third observing run. *Phys. Rev. D*, 102(6):062003, 2020.

[37] Katherine Dooley. *Design and Performance of High Laser Power Interferometers for Gravitational-wave Detection*. PhD thesis, University of Florida, 2011.

[38] Michael Zevin et al. Gravity Spy: Integrating Advanced LIGO Detector Characterization, Machine Learning, and Citizen Science. *Class. Quant. Grav.*, 34(6):064003, 2017.

[39] L. K. Nuttall. Characterizing transient noise in the LIGO detectors. *Phil. Trans. Roy. Soc. Lond. A*, 376(2120):20170286, 2018.

[40] Derek Davis et al. LIGO detector characterization in the second and third observing runs. *Class. Quant. Grav.*, 38(13):135014, 2021.

[41] Samantha A. Usman et al. The PyCBC search for gravitational waves from compact binary coalescence. *Class. Quant. Grav.*, 33(21):215004, 2016.

[42] D. Davis, T. B. Littenberg, I. M. Romero-Shaw, M. Millhouse, J. McIver, F. Di Renzo, and G. Ashton. Subtracting glitches from gravitational-wave detector data during the third LIGO-Virgo observing run. *Class. Quant. Grav.*, 39(24):245013, 2022.

[43] Duncan Macleod, Evan Goetz, Iara Ota, Maximiliano Isi, Thomas Massinger, Derek

Davis, Matt Pitkin, paulaltin, and Alex Nitz. gwpy/gwsumm: 2.2.6, April 2024.

[44] Hsin-Yu Chen, Daniel E. Holz, John Miller, Matthew Evans, Salvatore Vitale, and Jolien Creighton. Distance measures in gravitational-wave astrophysics and cosmology. *Class. Quant. Grav.*, 38(5):055010, 2021.

[45] Florent Robinet, Nicolas Arnaud, Nicolas Leroy, Andrew Lundgren, Duncan Macleod, and Jessica McIver. Omicron: a tool to characterize transient noise in gravitational-wave detectors. *SoftwareX*, 12:100620, 2020.

[46] Jessica L. McIver. *The impact of terrestrial noise on the detectability and reconstruction of gravitational wave signals from core-collapse supernovae*. PhD thesis, Massachusetts U., Amherst, Massachusetts U., Amherst, 2015.

[47] S. Chatterji, L. Blackburn, G. Martin, and E. Katsavounidis. Multiresolution techniques for the detection of gravitational-wave bursts. *Class. Quant. Grav.*, 21:S1809–S1818, 2004.

[48] Alex L. Urban, Duncan Macleod, Thomas Massinger, Jeffrey Bidler, Joshua Smith, Alexandra Macedo, Siddharth Soni, Scott Coughlin, Katerina Leman, Derek Davis, and Andy Lundgren. gwdetchar/gwdetchar: 1.0.2, December 2019.

[49] Joshua R. Smith, Thomas Abbott, Eiichi Hirose, Nicolas Leroy, Duncan Macleod, Jessica McIver, Peter Saulson, and Peter Shawhan. A Hierarchical method for vetoing noise transients in gravitational-wave detectors. *Classical Quantum Gravity*, 28:235005, 2011.

[50] S. Soni et al. Discovering features in gravitational-wave data through detector characterization, citizen science and machine learning. *Class. Quant. Grav.*, 38(19):195016, 2021.

[51] S. Soni et al. Reducing scattered light in LIGO's third observing run. *Class. Quant. Grav.*, 38(2):025016, 2020.

[52] Joseph S. Areeda, Joshua R Smith, Andrew P Lundgren, Edward Maros, Duncan M. Macleod, and John Zweizig. LigoDV-web: Providing easy, secure and universal access to a large distributed scientific data store for the LIGO Scientific Collaboration. *Astron. Comput.*, 18:27–34, 2017.

[53] S. Soni, J. Glanzer, Y. Kim, Y. Zheng, et al. aLIGO LLO Logbook. 56645, 2021.

[54] A. Effler. aLIGO LLO Logbook. 52427, 2020.

[55] S. Nichols and G. Gonzalez. aLIGO LLO Logbook. 53658, 2020.

[56] Jones, E., Nichols, S., Gonzalez, G. Solving the Mystery of Koi Fish Glitch Sources at LIGO. Technical Report T2300303, LSC, 2023.

[57] Tabata Aira Ferreira and Cesar Augusto Costa. Comparison between t-SNE and cosine similarity for LIGO glitches analysis. *Class. Quant. Grav.*, 39(16):165013, 2022.

[58] R. Dolesi, M. Hueller, D. Nicolodi, D. Tombolato, S. Vitale, P. J. Wass, W. J. Weber, M. Evans, P. Fritschel, R. Weiss, et al. *Phys. Rev. D*, 84:063007, 2011.

[59] M. E. Zucker and S. E. Whitcomb. Proceedings of the seventh marcel grossman meeting on recent developments in theoretical and experimental general relativity, gravitation, and relativistic field theories. In *Proceedings of the Seventh Marcel Grossman Meeting on recent developments in theoretical and experimental general relativity, gravitation, and relativistic field theories*, pages 1434–1436, 1996.

[60] M. E. Zucker and Stanley E. Whitcomb. Measurement of optical path fluctuations due to residual gas in the LIGO 40-meter interferometer. In *7th Marcel Grossmann Meeting on General Relativity (MG 7)*, pages 1434–1436, 7 1994.

[61] Weiss, R., Zucker, M., Whitcomb, S. Optical Pathlength Noise in Sensitive Interferometers Due to Residual Gas. Technical Report T952001, LSC, 1994.

[62] Weiss, R. Residual Gas in the LIGO beam Tubes. Technical Report G1100105, LSC, 2003.

[63] McCormick, S. and others. Pre-vent O4a RGA Scans. Technical Report E2400054, LSC, 2024.

[64] R. Schofield et al. aLIGO LHO Logbook. 35538, 2017.

[65] S. Nichols and G. Gonzalez. aLIGO LHO Logbook. 68897, 2023.

[66] S. Nichols and G. Gonzalez. aLIGO LLO Logbook. 64466, 2023.

[67] S. Nichols and A. Effler. aLIGO LLO Logbook. 70378, 2024.

[68] S. Nichols and A. Effler. aLIGO LLO Logbook. 70430, 2024.

Vita

Shania Nichols was born in Brooklyn, New York and graduated from Brentwood High School. She went on to the State University of New York College at Oswego (SUNY Oswego) where she received a B.S. in Meteorology with an Astronomy minor in 2018. During the summer of 2017, Shania participated in the Advancing Space Science through Undergraduate Research Experiences (ASSURE) Summer Research Program at University of California Berkeley's Space Sciences Lab (SSL). Following graduation from SUNY Oswego, Shania moved to Baton Rouge, Louisiana to pursue a Ph.D. in Physics from Louisiana State University.